

# The structure of ultrathin iron oxide films studied by x-ray diffraction

Dissertation (kumulativ)

zur Erlangung des Grades Doktor der Naturwissenschaft (Dr. rer. nat.)  
dem Fachbereich Physik der Universität Osnabrück  
vorgelegt von

**Florian Bertram, M.Sc.**

Osnabrück, Oktober 2012



# Contents

<b>1. Introduction</b>	<b>5</b>
<b>2. Theoretical background</b>	<b>7</b>
2.1. Crystals and epitaxy of crystalline thin films . . . . .	7
2.1.1. Single crystals . . . . .	7
2.1.2. Epitaxial films . . . . .	8
2.2. X-ray scattering . . . . .	11
2.3. X-ray diffraction . . . . .	11
2.3.1. The Bragg condition . . . . .	11
2.3.2. Scattering at a single atom . . . . .	14
2.3.3. Scattering at a unit cell . . . . .	15
2.3.4. Diffraction at single crystals . . . . .	15
2.3.5. Crystal truncation rods . . . . .	16
2.3.6. Modeling the diffracted intensity from a thin film layer system . . . . .	19
2.4. X-ray reflectivity . . . . .	21
2.5. Low-energy electron diffraction . . . . .	23
2.6. X-ray photoemission spectroscopy . . . . .	25
<b>3. Properties of iron oxides and iron oxide thin films</b>	<b>27</b>
3.1. Iron oxide . . . . .	27
3.2. Iron oxide thin films on MgO(001) . . . . .	31
3.3. The surface lattice coordinate system for the reciprocal space . . . . .	32
<b>4. Experimental setup and data analysis for synchrotron radiation experiments</b>	<b>37</b>
4.1. Generation of synchrotron radiation . . . . .	37
4.2. Setup of an x-ray scattering beamline for (grazing incidence) x-ray diffraction and x-ray reflectivity . . . . .	39
4.3. Scattering geometries . . . . .	46
4.4. Data correction . . . . .	48
4.5. Data analysis of x-ray diffraction data . . . . .	51
<b>5. Experimental results on the structure of iron oxide thin films</b>	<b>57</b>
<b>6. X-ray diffraction study on size effects in epitaxial magnetite thin films on MgO(001),</b> <i>PREPRINT</i>	<b>59</b>
F. Bertram, C. Deiter, O. Hoefert, M. Suendorf, T. Schemme, F. Timmer, B. Zimmermann, and J. Wollschläger <i>Journal of Physics D: Applied Physics</i> <b>45</b> , 395302 (2012).	

<b>7. Reordering between tetrahedral and octahedral sites in ultrathin magnetite films grown on MgO(001), PREPRINT</b>	<b>61</b>
F. Bertram, C. Deiter, T. Schemme, S. Jentsch, and J. Wollschläger <i>Journal of Applied Physics</i> <b>113</b> , 184103 (2013).	
<b>8. Post-deposition annealing induced reordering of tetrahedral sites</b>	<b>63</b>
8.1. Introduction . . . . .	63
8.2. Experimental setup . . . . .	63
8.3. Results . . . . .	63
8.4. Discussion . . . . .	66
8.5. Conclusion . . . . .	67
<b>9. In-situ x-ray diffraction studies on post deposition annealing of ultra-thin iron oxide films, PREPRINT</b>	<b>69</b>
F. Bertram, C. Deiter, K. Pflaum, M. Suendorf, C. Otte, and J. Wollschläger <i>Journal of Applied Physics</i> <b>110</b> , 102208 (2011).	
<b>10.A compact high vacuum heating chamber for in-situ x-ray scattering studies, PREPRINT</b>	<b>71</b>
F. Bertram, C. Deiter, K. Pflaum, and O. H. Seeck <i>Review of Scientific Instruments</i> <b>83</b> , 083904 (2012).	
<b>11. Summary and outlook</b>	<b>73</b>
<b>A. Derivation of the rms roughness model for x-ray diffraction</b>	<b>75</b>
<b>B. List of publications</b>	<b>77</b>
<b>Literature</b>	<b>81</b>
<b>List of Figures</b>	<b>91</b>
<b>List of Tables</b>	<b>95</b>

# 1. Introduction

Nowadays, most electronic devices are based on semiconductors, mainly silicon. Within the last decades the performance of these devices has increased enormously due to downscaling of the devices. However, the possibility of downscaling is limited. One approach to overcome this problem is using not only the charge of an electron but also its spin as information carrier. The combination of electronics and spin information is called *spintronics* [1,2].

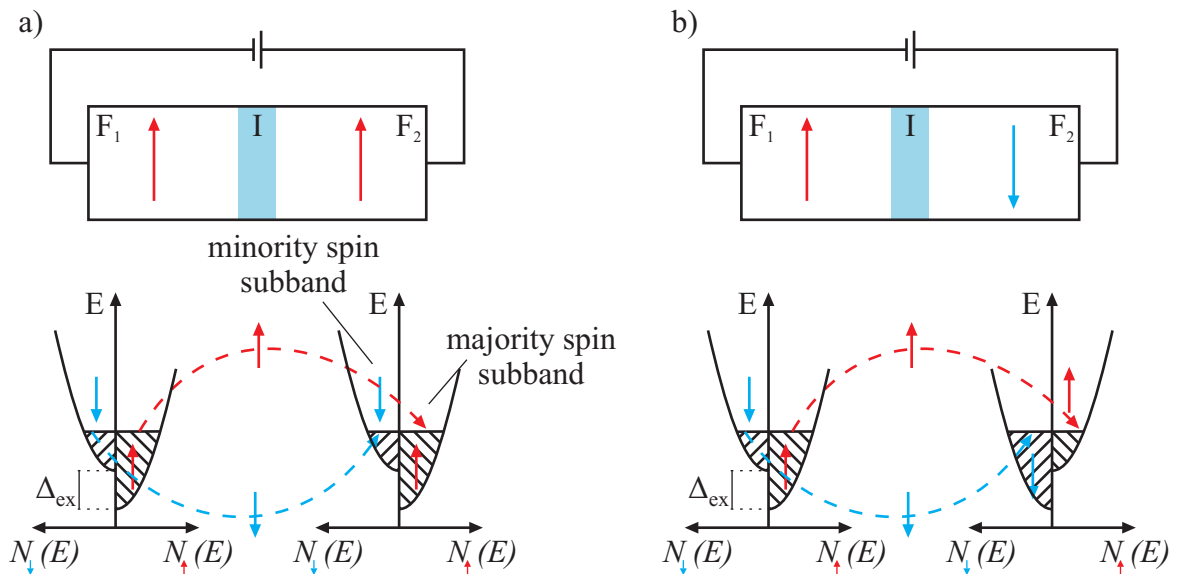


**Fig. 1.1:** Schematic drawing of a magnetic tunneling junction consisting of two ferromagnetic electrodes (F<sub>1</sub> and F<sub>2</sub>) separated by a thin insulator (I) and the respective density of states profile for magnetization in both electrodes aligned parallel (a) and antiparallel (b).

One example for a spintronic device is the magnetic tunneling junction (MTJ). A MTJ consists of two ferromagnetic electrodes separated by a thin insulator (typically a few nanometer) as illustrated in Fig. 1.1. If the electrodes are spin-polarized, i.e. the density of states at the Fermi level is different for spin-up and spin-down states, the tunneling magnetoresistance (TMR) effect can be observed. If the magnetization in both electrodes is parallel the tunneling probability through the insulator is higher than in the antiparallel case. This can be explained by the spin polarization of the electrodes and the fact that the electron spin is preserved in the tunneling process [3,4].

Due to their half metallic character with a predicted 100% spin polarization at the Fermi level and high Curie temperature magnetite (Fe<sub>3</sub>O<sub>4</sub>) thin films are excellent candidates for creating spintronic devices such as magnetic tunneling junctions [2,5]. Magnesium oxide and magnetite have a lattice mismatch of only 0.3%. Therefore, magnetite films can be easily grown on magnesium oxide surfaces at high crystal quality. Apart from that, magnesium

oxide can be used as a material for the insulating layer in a magnetic tunneling junction [6]. Iron oxides show various stoichiometries since the valence of Fe may alter between  $\text{Fe}^{2+}$  and  $\text{Fe}^{3+}$ . Therefore, iron oxides are, apart from their applications in the field of spintronics, also of large interest for catalytic applications. Possible catalytic applications are the Fischer–Tropsch synthesis [7], the oxidation of carbon monoxide [8–10], or the use as catalytic support for noble metal nanoparticles [11].

For both catalytic and spintronic applications it is important to understand the structure and growth properties of such oxide films. For ultrathin films characteristic material properties are often changed due to finite size or interface effects. In MTJs often reduced TMR effects, compared to theoretical predictions, have been observed. This could be attributed to spin-flips occurring at the ferromagnet/insulator interface [3,4]. By improving the quality of the interface it was possible to considerably increase the TMR effect [4]. Interface induced effects also often lead to changes in the electronic structure, which might cause a reduced spin polarization in the ferromagnetic layer of a MTJ. For magnetite thin films grown on magnesium oxide such reduced spin polarization has also been found [12].

Therefore, this thesis addresses the structure of ultrathin magnetite films grown on magnesium oxide by reactive molecular beam epitaxy. The main technique used to study the structure of these films is synchrotron radiation based (grazing incidence) x-ray diffraction (SR-(GI)XRD). In addition, x-ray reflectivity (XRR) is used to study film thickness and layer structure, lab source based x-ray photoemission spectroscopy (XPS) to obtain chemical information and low energy electron diffraction (LEED) to study the surface structure of the films.

Within the last decades SR-(GI)XRD has proven to be a very powerful technique to study the structure of surfaces and ultra thin films [13–16]. In contrast to standard surface science techniques for structure determination, like scanning probe microscopy (SPM) or electron diffraction, the large penetration depth of x-rays allows to study not only surface properties of the films but also the structure of buried layers, as well as properties of the film substrate interface. Using SR-(GI)XRD it is also possible to study order-disorder transitions within the film structure.

The first part of the thesis gives an overview on the theoretical background (Chap. 2). This includes considerations on the growth of single crystals and the theoretical basis of the experimental techniques used. In addition, a short review on the properties of iron oxides as well as iron oxide thin films will be given (Chap. 3). After that the experimental setup for synchrotron radiation based x-ray diffraction is discussed in detail (Chap. 4).

The second part of the thesis presents and discusses the experimental results on the structure of ultrathin iron oxide films. First, the influence of deposition conditions on the film structure is investigated. Afterwards, the influence of post-deposition annealing is studied.

## 2. Theoretical background

This chapter overviews of the theoretical background that is important for this work. First, crystals and crystalline thin films will be introduced briefly. Afterwards, x-ray diffraction (XRD), which is the main technique used in this work, is discussed in detail including a quantitative derivation with main focus on thin film layer systems. In addition, x-ray reflectivity (XRR), low energy electron diffraction (LEED), and x-ray photoemission spectroscopy (XPS) are discussed briefly.

### 2.1. Crystals and epitaxy of crystalline thin films

Since the topic of this work is about the structure of epitaxial thin films, the properties of single crystals [17,18] and crystalline thin films [19] will be discussed briefly in the following.

#### 2.1.1. Single crystals

A crystal is a structure with a periodicity in three dimensions. It consists of a basic arrangement of atoms, the unit cell, which is repeated infinitely in all three dimensions at constant distance for a perfect crystal. The repetition of the unit cell forms a three dimensional periodically ordered lattice, which is called *crystal lattice*.

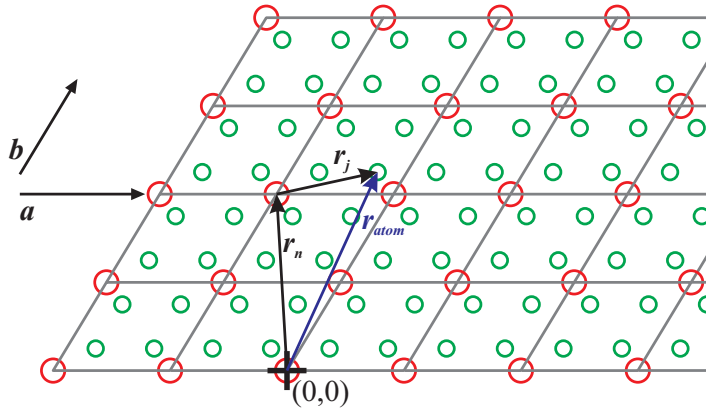


**Fig. 2.1:** Sketch of a two dimensional crystal. The position of each atom within the crystal  $\mathbf{r}_{atom}$  is given by the sum of the position vector of the unit cell  $\mathbf{r}_n$  and the position vector of the atom within the unit cell  $\mathbf{r}_j$ .

The crystal structure can be described by the positions of the atoms (or ions) in the unit cell and three linear independent translation vectors ( $\mathbf{a}$ ,  $\mathbf{b}$ , and  $\mathbf{c}$ ) giving the spatial repetition of the unit cell. These vectors define the shape and spacing of the crystal lattice and are therefore called *lattice vectors*. The position  $\mathbf{r}_{atom}$  of any atom (or ion) in a crystal is given by its position in the unit cell  $\mathbf{r}_j$  and a linear combination  $\mathbf{r}_n$  of the three lattice vectors  $\mathbf{a}$ ,  $\mathbf{b}$ , and  $\mathbf{c}$ :

$$\mathbf{r}_{atom} = \mathbf{r}_j + \mathbf{r}_n = \mathbf{r}_j + m \cdot \mathbf{a} + n \cdot \mathbf{b} + o \cdot \mathbf{c} , \quad (2.1)$$

where  $m$ ,  $n$ , and  $o$  are integer numbers. This is illustrated in Fig. 2.1 for a two dimensional crystal.

Different types of crystals are sorted by their symmetries. A common example is the face centered cubic (fcc) lattice. Here the crystal lattice has a cubic symmetry with an additional atom on each face of the cube. Details can be found in the literature [17, 18, 20].

Instead of describing the unit cell directly with lattice vectors it can be alternatively characterized by the absolute values of the lattice vectors  $a$ ,  $b$ , and  $c$  and the angles  $\alpha$ ,  $\beta$ , and  $\gamma$  between them. The lattice vectors can be calculated from these values.

### Lattice planes

For Bragg reflection the lattice planes of a crystal play a very important role. A lattice plane is indexed by three integer indices  $h$ ,  $k$ ,  $l$ , known as Miller indices. They describe the lattice plane which intercepts the three crystallographic axes defined by the lattice vectors at  $a/h$ ,  $b/k$ , and  $c/l$ .

If any of the Miller indices  $hkl$  is a non integer value they are replaced by a set  $hkl$  with the smallest common integer multiple but the same ratio as the original  $hkl$ , e.g.  $(1\frac{1}{2}\frac{1}{3})$  becomes  $(632)$ .

### 2.1.2. Epitaxial films

The growth of a crystallographically oriented single crystal film on a single crystalline substrate is called *epitaxy* [19]. The epitaxial growth is usually divided into three basic growth modes (cf. Fig. 2.2):

- **Layer-by-layer (or Frank-van der Merve) growth:**  
Each atomic layer is completed before a new layer is formed on top. This is the case if the adatoms are bound stronger to the substrate surface than to each other.
- **Island (or Vollmer-Weber) growth:**  
Three dimensional islands nucleate directly on the surface. In this case the adatoms are bound stronger to each other than to the substrate surface.
- **Layer-plus-island (or Stranski-Krastanov) growth:**  
After the formation of an initial atomically flat layer (see layer-by-layer growth) the growth mode changes to island growth. The thickness of the intermediate flat layer depends on the particular case.

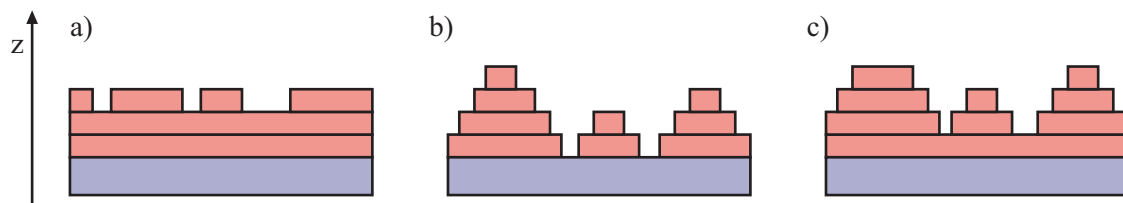


**Fig. 2.2:** Schematic drawings of the different growth modes: a) layer-by-layer, b) island, and c) layer-plus-island growth.

### Lattice mismatch and relaxation

Apart from the growth mode the lattice mismatch and resulting strain effects play an important role in thin film epitaxy. When depositing one material on a different one (heteroepitaxy) their lattice constants usually do not exactly match. However, only the mismatch within the surface plane is of concern. The lattice mismatch is defined as

$$\epsilon = \frac{a_{film} - a_{substrate}}{a_{substrate}} \quad (2.2)$$

where  $a_{substrate}$  and  $a_{film}$  are the lateral lattice constants of the substrate and the film material, respectively. It is important to note that the lattice mismatch is generally not the same in different crystallographic directions. To compensate the lattice mismatch two processes can be observed.

1. **pseudomorphic growth:** The lattice of the film is compressed (or stretched) in lateral directions to meet the lateral lattice constants of the substrate. As a result the film is distorted in vertical direction accordingly to keep the unit cell volume constant.
2. formation of **misfit dislocations:** The misfit is compensated by dislocations in the film lattice. With increasing film thickness the film is relaxing towards its bulk properties.

If the lattice mismatch is relatively small pseudomorphic growth can typically be observed, while misfit dislocations usually occur for larger lattice mismatch.

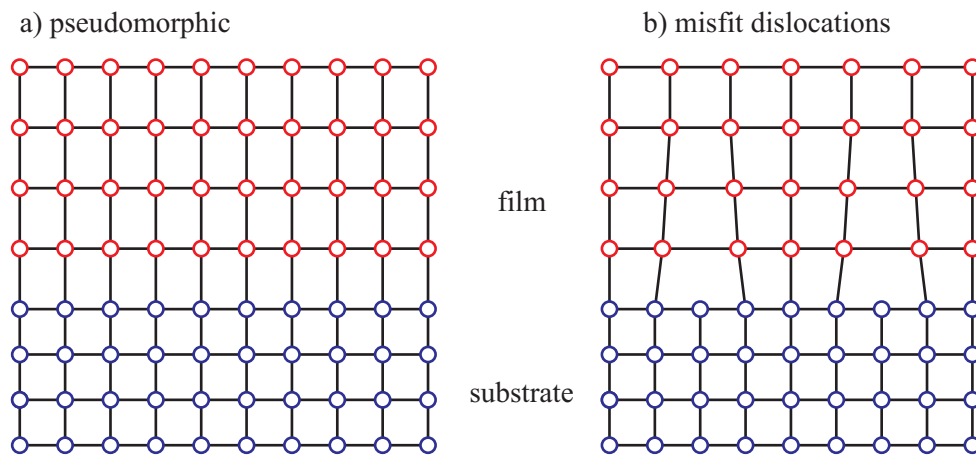


**Fig. 2.3:** Schematic drawings of the different relaxation processes: a) pseudomorphic growth, and b) misfit dislocations.

### Molecular beam epitaxy

One of the most common techniques to grow epitaxial thin films is molecular beam epitaxy (MBE). Here, the material grown on a sample surface is delivered by an atomic or molecular beam. Due to the very small free mean path of such molecular beams under ambient conditions, MBE is usually performed in ultra high vacuum (UHV) chambers. The molecular beam is generated by heating a source material until it starts to evaporate or sublimate (depending on the used material). One of the most common techniques to achieve the heating is electron

beam bombardment. High voltage of typically  $\approx 1000$  V is applied to a crucible containing the source material. Electrons emitted from a filament nearby are accelerated by the high voltage towards the crucible, which is heated by the electron impact. In case of metals it is also possible to omit the crucible and apply the high voltage directly to the material source. Here, it is necessary, that the metal sublimates at lower temperatures than the melting temperature (at the given pressure), which is the case for e.g. iron.

To grow metal oxide films by MBE the pure metal may be evaporated in a low oxygen atmosphere. Typically, it is much easier to evaporate the pure metal instead of the metal oxide, since the required evaporation (or sublimation) temperature is usually much lower. By changing the oxygen partial pressure during growth it is possible to change the oxide phase of the film. This technique is called *reactive* MBE. When using oxygen plasma instead of oxygen gas it is called *plasma* MBE.

Other common techniques to grow epitaxial films are pulsed laser deposition (PLD), where the source material is evaporated by an intense pulsed laser beam and sputter deposition, where the atoms from the source material are ejected by ion bombardment (sputtering).

## 2.2. X-ray scattering

The basic principle of x-ray scattering techniques is that an incoming x-ray beam is scattered at an object. Afterwards, the scattered intensity is detected [20]. Since the cross section from x-rays with the atomic nucleus is of orders of magnitude smaller than the cross section with electrons, the contribution from x-rays scattered at nuclei is usually neglected. The amplitude  $A(\mathbf{q})$  of an x-ray wave scattered at an electron at the position  $\mathbf{r}_e$  is given by the Thomson formula

$$A(\mathbf{q}) = A_0 \frac{e^2}{m_e c^2 R_0} e^{i\mathbf{q} \cdot \mathbf{r}_e} \quad (2.3)$$

where  $A_0$  is the amplitude of the incoming wave,  $e$  and  $m_e$  are the charge and the mass of an electron,  $c$  is the speed of light and  $R_0$  is the distance between the electron and the observer. The amplitude is given as a function of the scattering vector  $\mathbf{q} \equiv \mathbf{k}_f - \mathbf{k}_i$  determined by the difference of the wave vectors of the scattered ( $\mathbf{k}_f$ ) and incoming wave ( $\mathbf{k}_i$ ). For reasons of simplicity we combine all constants in one constant  $C \equiv \frac{e^2}{m_e c^2 R_0}$  and reduce formula 2.3 to

$$A(\mathbf{q}) = A_0 C e^{i\mathbf{q} \cdot \mathbf{r}_e} . \quad (2.4)$$

Here, the influence of the polarization of the incidence beam is neglected. Since it strongly depends on the specific scattering geometry, it will be introduced as a correction factor to the measured intensity later on (Chap. 4.4).

Real objects contain many electrons. Therefore, the scattering at such objects is the sum of the scattering processes at all contributing electrons. Due to the low interaction of x-rays with matter it is possible to describe x-ray scattering processes in terms of the kinematical scattering theory. Here, **multiple scattering**, **refraction**, and **absorption** are neglected. Within this approximation the scattered intensity of an object is given by the Fourier transformation of its electron density.

## 2.3. X-ray diffraction

The scattering of x-rays at long range ordered periodic systems is in general called x-ray diffraction. These systems are typically crystals. The scattering at these periodic structures cause constructive and destructive interference of the scattered waves resulting in spots of very high intensity. These spots are called Bragg peaks or Bragg reflections. The phenomena of x-ray diffraction in single crystals was first discovered and theoretically described by Laue [21] and Bragg [22] in 1912 and 1913, respectively.

### 2.3.1. The Bragg condition

Bragg described the diffraction of x-rays at a crystal lattice by reflection of the incidence x-rays at lattice planes. Due to their path difference, as illustrated in Fig. 2.4, the reflected beams from different parallel lattice planes cause an interference pattern. Here, Bragg peaks

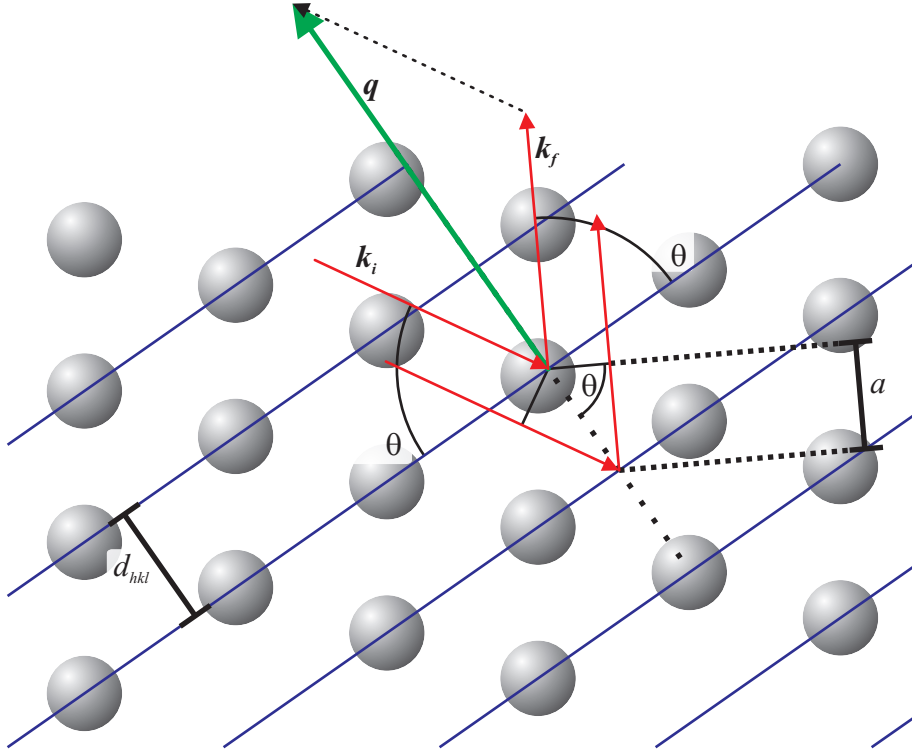


**Fig. 2.4:** An incidence wave  $k_i$  is reflected at a crystal lattice plane (solid lines). The outgoing waves  $k_f$  have different phase due to the path difference  $a$ . If  $2a = n\lambda$  is fulfilled the outgoing waves interfere constructively and a Bragg peak can be observed. The scattering vector  $q$  resulting from  $k_i$  and  $k_f$  is oriented perpendicular to the lattice planes.

occur where the Bragg condition given by

$$2d_{hkl} \sin \theta = n\lambda \quad (2.5)$$

is fulfilled. The distance between two lattice planes is given by  $d_{hkl}$ ,  $\theta$  is the angle between the lattice planes and the incidence angle and the exit angle, as well. The order of the Bragg reflection is given by  $n$  and  $\lambda$  is the vacuum wavelength of the incidence beam. This equation also gives a condition for wavelengths used for diffraction at typical crystal lattices. The Bragg angle of the first order Bragg reflection is given by

$$\theta = \arcsin \frac{\lambda}{2d_{hkl}} . \quad (2.6)$$

This equation is only valid if  $\lambda \leq 2d_{hkl}$  is fulfilled. This means if the maximum path difference which can be achieved ( $2d_{hkl}$  at normal incidence) is smaller than the wavelength no constructive interference is possible. Therefore, no diffraction phenomena can be observed.

Since the distance of lattice planes in typical crystals is in the order of a few Ångströms the wavelength should also be of that order or less. At the same time, the wavelength should not be too small since this would cause very small Bragg angles, which are technically difficult to observe and lead to a lower resolution in reciprocal space.

This requirement on the wavelength is fulfilled by x-ray photons.

### The reciprocal space

Instead of using the Bragg law to identify positions of Bragg peaks one can also use the equivalent Laue conditions

$$\mathbf{q} \cdot \mathbf{a} = 2\pi h \quad , \quad (2.7)$$

$$\mathbf{q} \cdot \mathbf{b} = 2\pi k \quad , \quad (2.8)$$

$$\mathbf{q} \cdot \mathbf{c} = 2\pi l \quad (2.9)$$

with the scattering vector  $\mathbf{q}$  and the unit vectors of the crystal  $\mathbf{a}$ ,  $\mathbf{b}$ , and  $\mathbf{c}$ . Bragg peaks occur wherever  $h$ ,  $k$ , and  $l$  are integer numbers.  $h$ ,  $k$ , and  $l$  are the Miller indices which are also used to index lattice planes as explained above.

An important concept related to the Laue conditions are the reciprocal lattice vectors. They are related to the real space lattice vectors  $\mathbf{a}$ ,  $\mathbf{b}$ , and  $\mathbf{c}$  and are defined as

$$\mathbf{a}^* = 2\pi \frac{\mathbf{b} \times \mathbf{c}}{\mathbf{a} \cdot (\mathbf{b} \times \mathbf{c})} \quad , \quad (2.10)$$

$$\mathbf{b}^* = 2\pi \frac{\mathbf{c} \times \mathbf{a}}{\mathbf{a} \cdot (\mathbf{b} \times \mathbf{c})} \quad , \quad (2.11)$$

$$\mathbf{c}^* = 2\pi \frac{\mathbf{a} \times \mathbf{b}}{\mathbf{a} \cdot (\mathbf{b} \times \mathbf{c})} \quad (2.12)$$

where  $\mathbf{a} \cdot (\mathbf{b} \times \mathbf{c})$  gives the unit cell volume. If all angles between the lattice vectors are  $\alpha = \beta = \gamma = 90^\circ$  the lengths of the reciprocal lattice vectors are given by

$$a^* = \frac{2\pi}{a} \quad , \quad (2.13)$$

$$b^* = \frac{2\pi}{b} \quad , \quad (2.14)$$

$$c^* = \frac{2\pi}{c} \quad . \quad (2.15)$$

If the scattering vector  $\mathbf{q}$  is equal to one of the reciprocal lattice vectors  $\mathbf{a}^*$ ,  $\mathbf{b}^*$ , and  $\mathbf{c}^*$ , the Laue condition is automatically fulfilled for  $h$ ,  $k$ , and  $l$ , respectively. Thus, when using these vectors as basis vectors for the reciprocal space the Laue condition is fulfilled at all positions in reciprocal space given by the coordinates  $(hkl)$  where  $h$ ,  $k$ , and  $l$  are integer numbers. Therefore, it is convenient to describe diffraction phenomena using the reciprocal space with the reciprocal lattice vectors as basis vectors.

The Laue condition as well as the Bragg condition define only the occurrence of Bragg peaks due to the symmetry of the crystal lattice. However, the contribution from the structure of the unit cell is neglected. The inner structure of unit cells often leads to interference at Bragg peaks which may alter the intensity. If the interference leads to zero intensity at Bragg peaks they are called *structure forbidden peaks*. Describing the diffraction by a crystal the amplitude is typically divided into its contribution from the unit cell, the structure factor  $F(\mathbf{q})$ , and the contribution from the lattice symmetry, the lattice factor  $G(\mathbf{q})$ . Thus, the amplitude  $A(\mathbf{q})$  is

given by

$$A(\mathbf{q}) = F(\mathbf{q}) G(\mathbf{q}) . \quad (2.16)$$

The Bragg condition and the Laue conditions are not giving quantitative information on the diffracted intensity. Therefore, a quantitative description for the diffracted intensity from single crystal thin film systems grown on single crystal substrates will be derived in the following using the simplifications from the kinematic approximation explained above. The derivation is mainly based on theoretical descriptions given by Feidenhans'l [23], Robinson and Tweed [24], and Deiter [25].

### 2.3.2. Scattering at a single atom

The amplitude of a wave scattered at a single atom is given by the summation over the scattering from all electrons of this atom, given by the Thompson scattering formula (cf. Eq. 2.4), taking the phase difference between the waves scattered at different electrons into account. One has to consider that the electrons are not localized at the center of an atom given by  $\mathbf{r}_a$  but are distributed around the center according to the electron distribution function  $\rho$ . A second point to consider is that the distance between electron and observer  $R_0$  is slightly different for all possible electron positions. But since the distance between the electrons and the center of the atom  $|\mathbf{r}|$  is typically many orders of magnitude smaller than  $R_0$  we can assume the same value of  $R_0$  for all electrons. Thus, the amplitude of a wave scattered at an atom is given by

$$A(\mathbf{q}) = A_0 C \int d^3r \rho(\mathbf{r}) e^{i\mathbf{q} \cdot (\mathbf{r}_a + \mathbf{r})} \quad (2.17)$$

$$= A_0 C f(\mathbf{q}) e^{i\mathbf{q} \cdot \mathbf{r}_a} . \quad (2.18)$$

Here, we define the atomic form factor

$$f(\mathbf{q}) = \int d^3r \rho(\mathbf{r}) e^{i\mathbf{q} \cdot \mathbf{r}} \quad (2.19)$$

which results from the Fourier transformation of the electron density of the atom. It can be determined by quantum mechanical methods such as Hartree-Fock or density functional theory. Calculated values for different atoms and ions can be found in literature [26]. In this work values calculated assuming a spherical electron distribution are used. Thus, the form factor depends only on the absolute value of  $\mathbf{q}$  and not on the direction.

To derive a function defining the form factor the calculated values are approximated by four Gaussian functions

$$f(q) = \sum_{j=1}^4 a_j e^{-b_j \left(\frac{q}{4\pi}\right)^2} + c . \quad (2.20)$$

Values for the constants  $a_i$ ,  $b_i$  and  $c$  are also available for many ions in literature [26].

### 2.3.3. Scattering at a unit cell

After deriving an expression to describe the amplitude of x-rays scattered at a single atom we move on to the most basic structure in a crystal, the unit cell. The unit cell describes a basic arrangement of atoms which is periodically repeated to build up the crystal (cf. Sec. 2.1.1). The amplitude for an x-ray wave scattered at a single unit cell is given by the summation over the amplitudes scattered at the atoms of the unit cell

$$A(\mathbf{q}) = A_0 C \sum_j f_j(q) e^{i\mathbf{q} \cdot (\mathbf{r}_n + \mathbf{r}_j)} \quad (2.21)$$

$$= A_0 C F(\mathbf{q}) e^{i\mathbf{q} \cdot \mathbf{r}_n} . \quad (2.22)$$

Here, the position of the unit cell is given by  $\mathbf{r}_n$  while the position of the atom within the unit cell is given by  $\mathbf{r}_j$ . We define the structure factor of the unit cell

$$F(\mathbf{q}) = \sum_j f_j(q) e^{i\mathbf{q} \cdot \mathbf{r}_j} . \quad (2.23)$$

It is important to mention that in contrast to the atomic form factor, which is isotropic in all directions, the structure factor depends on the direction of the scattering vector due to the phase difference between x-ray waves scattered at different atoms.

### The Debye-Waller factor

The equation obtained above assumes that all atoms are located at fixed positions. In fact these positions are just average values. Due to thermal vibrations, impurities, dislocations, or defects, the atoms within a unit cell might be shifted from their ideal position. This leads to a change in the scattered intensity which is typically described by a Debye-Waller factor  $D$  so that the modified structure factor is given by

$$\overline{F(\mathbf{q}, D)} = e^{-D|\mathbf{q}|^2} \sum_j f_j(q) e^{i\mathbf{q} \cdot \mathbf{r}_j} \quad (2.24)$$

assuming a Gaussian distribution of the atoms around their ideal position. Thus, the Debye-Waller factor leads to a dampening of the structure factor which increases with increasing scattering vector. The Debye-Waller factor itself increases with increasing atomic displacement. A detailed derivation of the Debye-Waller factor from thermal vibrations can be found in the book of Warren [20].

### 2.3.4. Diffraction at single crystals

So far we considered only single objects to describe the scattered x-ray wave amplitude. Now we look at periodic structures, crystals, which are formed from these objects. As already mentioned a crystal is an object consisting of a unit cell which is periodically repeated. The scattering from such periodic structures is called *diffraction*. The amplitude diffracted at a

crystal is given by the summation over the scattering amplitudes of all unit cells

$$A(\mathbf{q}) = A_0 C \sum_n F_n(\mathbf{q}) e^{i\mathbf{q} \cdot \mathbf{r}_n} . \quad (2.25)$$

In our case of a three dimensional perfect crystal where  $F_n$  is identical for all unit cells we can rewrite Eq. 2.25 and obtain

$$A(\mathbf{q}) = A_0 C F(\mathbf{q}) \sum_{n_a=0}^{N_a-1} \sum_{n_b=0}^{N_b-1} \sum_{n_c=0}^{N_c-1} e^{i\mathbf{q} \cdot (n_a \mathbf{a} + n_b \mathbf{b} + n_c \mathbf{c})} \quad (2.26)$$

$$= A_0 C F(\mathbf{q}) \sum_{n_a=0}^{N_a-1} e^{in_a \mathbf{q} \cdot \mathbf{a}} \sum_{n_b=0}^{N_b-1} e^{in_b \mathbf{q} \cdot \mathbf{b}} \sum_{n_c=0}^{N_c-1} e^{in_c \mathbf{q} \cdot \mathbf{c}} \quad (2.27)$$

with the lattice vectors of the crystal  $\mathbf{a}$ ,  $\mathbf{b}$  and  $\mathbf{c}$  and the number of unit cells in the three corresponding dimensions  $N_a$ ,  $N_b$  and  $N_c$ .

### 2.3.5. Crystal truncation rods

Considering a bulk crystal with infinite size in all three dimensions Eq. 2.27 becomes a series of  $\delta$  functions with intensity peaks at single points known as Bragg peaks. However, considering surfaces and thin films the crystal is not infinite in the vertical direction. As a consequence the diffracted intensity is not located at single spots but smeared out in vertical direction forming crystal truncation rods (CTRs) [23,24], as illustrated in Fig. 2.5.

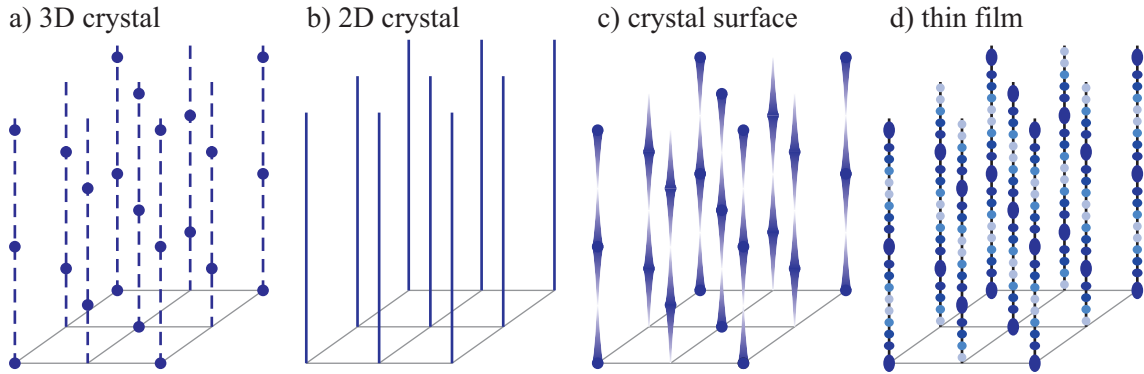


**Fig. 2.5:** Schematic drawing showing the intensity distribution in reciprocal space. a) Three dimensional crystals produce diffraction spots in reciprocal space. The dashed lines are direction markers only. b) Two dimensional layers produce diffraction rods. c) Surfaces of crystals produce diffraction spots connected by modulated diffraction rods in vertical direction. d) Thin films produce diffraction spots and oscillations (fringes) in vertical direction.

To describe a semi-infinite crystal substrate we have to substitute the sum over  $n_c$  for the vertical direction by the sum

$$\sum_{-\infty}^{N_c(n_a, n_b)} e^{in_c \mathbf{q} \cdot \mathbf{c}} . \quad (2.28)$$

This results in

$$A_{\text{substrate}}(\mathbf{q}) = A_0 C F(\mathbf{q}) \sum_{n_a=0}^{N_a-1} e^{i n_a \mathbf{q} \cdot \mathbf{a}} \sum_{n_b=0}^{N_b-1} e^{i n_b \mathbf{q} \cdot \mathbf{b}} \sum_{n_c=-\infty}^{N_c(n_a, n_b)} e^{i n_c \mathbf{q} \cdot \mathbf{c} + n_c \epsilon} \quad (2.29)$$

where  $e^{n_c \epsilon}$  is a dampening factor taking into account the absorption within deeper crystal layers. The function  $N_c(n_a, n_b)$  describes a variation of height in lateral direction (cf. Fig. 2.6) and is therefore describing a surface roughness.

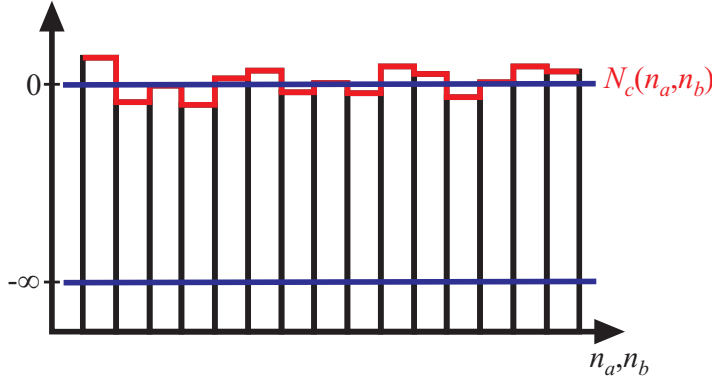


**Fig. 2.6:** Height profile of a semi-infinite crystal surface. The average step height is at the zero level, while the profile is defined by the function  $N_c(n_a, n_b)$ .

In case of a crystal truncation rod we can assume that the Laue conditions in lateral direction ( $\mathbf{q} \cdot \mathbf{a} = 2\pi h$  and  $\mathbf{q} \cdot \mathbf{b} = 2\pi k$ ) are fulfilled and thus, simplify Eq. 2.29 to

$$A_{\text{substrate}}(\mathbf{q}) = A_0 C F(\mathbf{q}) \sum_{n_a=0}^{N_a-1} 1 \sum_{n_b=0}^{N_b-1} 1 \sum_{n_c=-\infty}^{N_c(n_a, n_b)} e^{i n_c \mathbf{q} \cdot \mathbf{c} + n_c \epsilon} \quad (2.30)$$

$$= A_0 C F(\mathbf{q}) \sum_{n_a=0}^{N_a-1} \sum_{n_b=0}^{N_b-1} \frac{e^{(i \mathbf{q} \cdot \mathbf{c} + \epsilon) N_c(n_a, n_b)}}{1 - e^{-(i \mathbf{q} \cdot \mathbf{c} + \epsilon)}} \quad (2.31)$$

where the sum over  $n_a$  and  $n_b$  can be considered as an averaging over the height function  $N_c(n_a, n_b)$ . Thus, we write

$$A_{\text{substrate}}(\mathbf{q}) = A_0 C F(\mathbf{q}) N_a N_b \frac{\left\langle e^{(i \mathbf{q} \cdot \mathbf{c} + \epsilon) N_c(n_a, n_b)} \right\rangle}{1 - e^{-(i \mathbf{q} \cdot \mathbf{c} + \epsilon)}}. \quad (2.32)$$

Assuming a Gaussian height distribution of  $N_c(n_a, n_b)$  we obtain

$$A_{\text{substrate}}(\mathbf{q}) = A_0 C F(\mathbf{q}) N_a N_b \frac{e^{-\sigma^2 (1 - \cos \mathbf{q} \cdot \mathbf{c})}}{1 - e^{-(i \mathbf{q} \cdot \mathbf{c} + \epsilon)}} \quad (2.33)$$

where  $\sigma$  is the rms<sup>1</sup> roughness of the semi-infinite substrate. A detailed derivation is given in Appendix A.

<sup>1</sup>root mean square

Using a similar approach we can describe the diffraction from a thin film of only a few layers. Here, in addition to the roughness at the top of the film one has also to consider a roughness at the bottom resulting in two height functions  $N_c^+(n_a, n_b)$  for the top and  $N_c^-(n_a, n_b)$  for the bottom (cf. Fig. 2.7). The intermediate number of unit cells is given by  $\bar{N}_c$ . In addition we can neglect the influence of absorption for thin films. We now obtain

$$A_{film}(\mathbf{q}) = A_0 C F(\mathbf{q}) \sum_{n_a=0}^{N_a-1} 1 \sum_{n_b=0}^{N_b-1} 1 \sum_{n_c=N_c^-(n_a, n_b)}^{N_c^+(n_a, n_b)} e^{i n_c \mathbf{q} \cdot \mathbf{c}} \quad (2.34)$$

$$= A_0 C F(\mathbf{q}) \sum_{n_a=0}^{N_a-1} \sum_{n_b=0}^{N_b-1} \frac{e^{i \mathbf{q} \cdot \mathbf{c} N_c^-(n_a, n_b)} - e^{i \mathbf{q} \cdot \mathbf{c} N_c^+(n_a, n_b)} + 1}{1 - e^{i \mathbf{q} \cdot \mathbf{c}}} \quad (2.35)$$

where the sum can also be expressed by an averaging

$$A_{film}(\mathbf{q}) = A_0 C F(\mathbf{q}) N_a N_b \frac{\left\langle e^{i \mathbf{q} \cdot \mathbf{c} u_c^-} \right\rangle - e^{i \mathbf{q} \cdot \mathbf{c} \bar{N}_c} \left\langle e^{i \mathbf{q} \cdot \mathbf{c} u_c^+} \right\rangle}{1 - e^{i \mathbf{q} \cdot \mathbf{c}}} \quad (2.36)$$

where  $u_c^+$  and  $u_c^-$  are the deviations from the average film thickness  $\bar{N}_c$  to the top and the bottom, respectively.

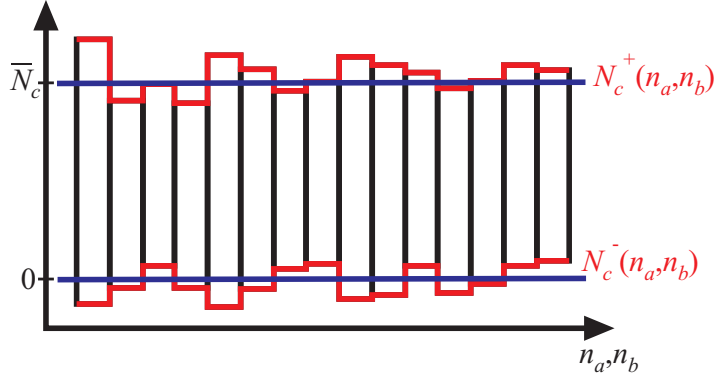


**Fig. 2.7:** Height profile of a thin film with an average thickness of  $\bar{N}_c$ . The roughness of the film top is given by  $N_c^+(n_a, n_b)$ , the roughness of the film bottom is given by  $N_c^-(n_a, n_b)$ .

Assuming again a Gaussian distribution for  $u_c^+$  and  $u_c^-$  we obtain

$$A_{film}(\mathbf{q}) = A_0 C F(\mathbf{q}) N_a N_b \frac{e^{-\sigma_-^2 (1 - \cos \mathbf{q} \cdot \mathbf{c})} - e^{i \mathbf{q} \cdot \mathbf{c} \bar{N}_c} e^{-\sigma_+^2 (1 - \cos \mathbf{q} \cdot \mathbf{c})}}{1 - e^{i \mathbf{q} \cdot \mathbf{c}}} \quad (2.37)$$

with  $\sigma_+$  and  $\sigma_-$  representing the top and bottom rms roughness of the film.

Assuming zero roughness the diffraction from a thin film reduces to the form

$$S_N(x) = \sum_{n=0}^{N-1} e^{inx} = \frac{1 - e^{ixN}}{1 - e^{ix}} \quad (2.38)$$

This formula is known as the N-slit function with  $x = \mathbf{q} \cdot \mathbf{c}$  and  $N = \bar{N}_c$ . It shows main maxima at  $x = 2\pi m$  for  $m \in \mathbb{Z}$  with a maximum value of  $N$ . In addition to the main maxima

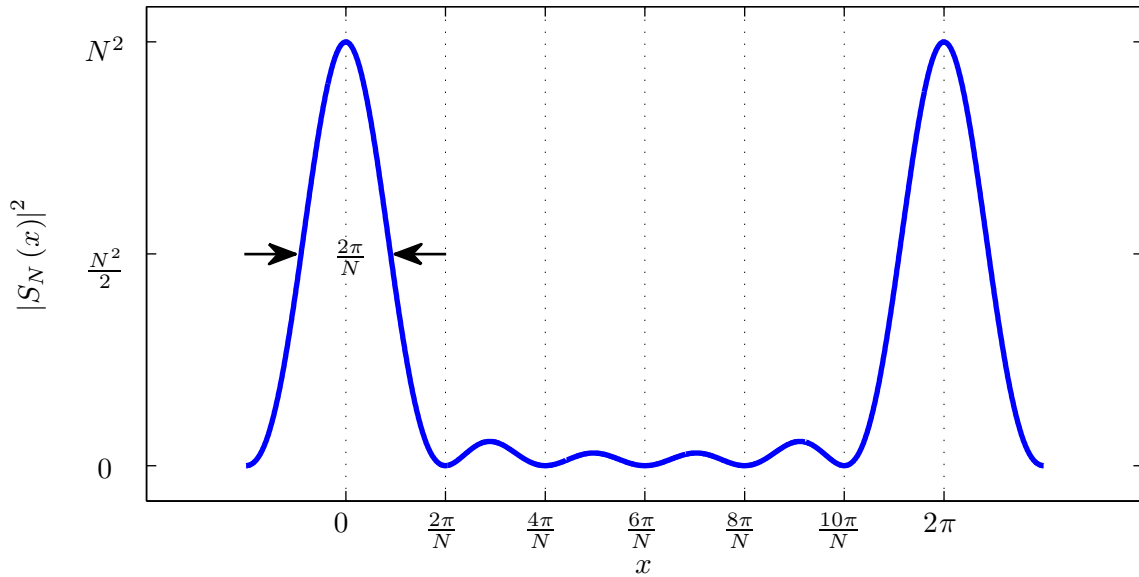


**Fig. 2.8:** The N-slit function for  $N = 6$ . Main maxima occur at multiples of  $2\pi$  with  $N - 2$  smaller side maxima or fringes in between two main maxima. The spacing between two fringes is  $\frac{2\pi}{N}$ . The FWHM of the main peaks is also given by  $\frac{2\pi}{N}$ .

the N-slit function has also  $N - 2$  smaller side maxima between two main maxima. These smaller side maxima are called fringes. With increasing number of slits  $N$  the number of the fringes increases and the peak width of the side maxima and the main maxima is decreasing. For infinite  $N$  the N-slit function passes over into periodic iterated  $\delta$  functions located at the positions of the main maxima. Fig. 2.8 shows the characteristic profile of an N-slit function for  $N = 6$ .

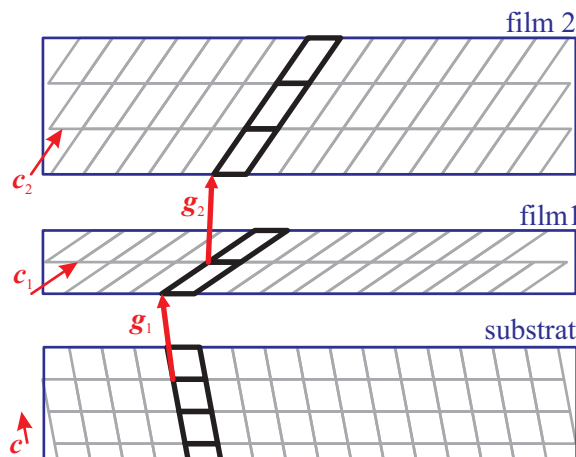


**Fig. 2.9:** Schematical drawing of a layer system consisting of two films and a substrate.

### 2.3.6. Modeling the diffracted intensity from a thin film layer system

A layer system (cf. Fig. 2.9) is usually consisting of a substrate and one or more layers on top of it. To calculate the diffracted intensity we have to calculate the sum over the substrate

and all top layers taking the phase difference into account. The amplitude for such a layer system is given by

$$A_{system}(\mathbf{q}) = A_{substrate}(\mathbf{q}) + \sum_i \Theta_i e^{i\mathbf{q} \cdot \mathbf{p}_i} A_{film,i}(\mathbf{q}) \quad (2.39)$$

where  $\Theta_i$  is an occupation factor describing impurities and dislocations in the layer. The phase factor  $e^{i\mathbf{q} \cdot \mathbf{p}_i}$  takes into account the phase difference between the substrate and the layers. The phase vector  $\mathbf{p}_i$  is defined as

$$\mathbf{p}_i = \sum_{j=0}^{i-1} \mathbf{g}_j + \overline{N_{c_j}} \mathbf{c}_j \quad (2.40)$$

where  $\mathbf{g}_j$  is an interface vector defining distance and lateral shift between layer  $j$  and  $j + 1$ .  $\overline{N_{c_j}} \mathbf{c}_j$  gives the phase shift due to the film thickness of layer  $j$ .

## 2.4. X-ray reflectivity

With x-ray reflectivity (XRR) it is possible to investigate the layer structure of surfaces, interfaces and thin films. To study the x-ray reflectivity of a thin film or a layer system the intensity of the reflected beam is measured as a function of the incidence angle  $\alpha_i$ . For such measurements the incidence angle is typically kept below  $5^\circ$ . In contrast to conventional optics the incidence angle of x-rays is typically given as angle between the incidence beam and the surface. More detailed descriptions on the theory of x-ray reflectivity are available in the literature in large quantity, e.g. [15,27]. In case of reflectivity the scattering vector has only a vertical component which is given by  $q = \frac{4\pi}{\lambda} \sin \alpha_i$ .

The most important value to describe the reflectivity of a material is the refractive index  $n$ . For x-rays it is defined as

$$n = 1 - \delta + i\beta \quad (2.41)$$

where  $\delta$  and  $\beta$  are material specific constants related to the x-ray scattering probability of the material. The value of  $\delta$  is proportional to the electron density and is typically on the order of  $10^{-6}$  while  $\beta$  is proportional to the absorption and about a factor 100 smaller than  $\delta$ . Thus, the refractive index in case of x-rays is slightly smaller than unity. Therefore, it is possible to observe total external reflection when studying the reflectivity of surfaces and thin films with x-rays below a critical angle  $\alpha_c$ . Using Snell's law the value of this critical angle can be approximated to

$$\alpha_c \approx \sqrt{2\delta} \quad (2.42)$$

The reflectivity of an interface of two layers ( $j$  and  $j+1$ ) of different composition with different refractive indexes is given by the Fresnel coefficient

$$r_{j,j+1} = \frac{q_j - q_{j+1}}{q_j + q_{j+1}} \quad (2.43)$$

where  $q_j = k\sqrt{n_j^2 - \cos^2 \alpha_i}$  is the vertical component of the wave vector transfer in layer  $j$ .  $k = \frac{2\pi}{\lambda}$  is the absolute value of the wave vector and  $\lambda$  is the vacuum wavelength.

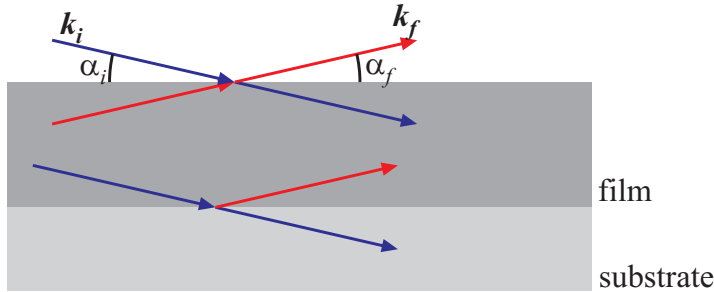


**Fig. 2.10:** Reflectivity of a thin film on a substrate. At each interface the incidence beam ( $k_i$ ) is reflected and transmitted. Also, the reflection and transmission of the beam reflected at buried interfaces is contributing to the total reflected intensity.

The reflected intensity of a layer system on flat substrates as sketched in Fig. 2.10 can be calculated by a recursive algorithm known as Parratt algorithm [28] taking into account the reflectivity and transmission of each interface. To consider the interface roughness when using the Parratt algorithm different roughness models have been proposed. The most common

model for solid thin films is a formalism described by Nevot-Crochet [29]. This model assumes an error-function type electron density profile at the interface. It results in an exponential factor reducing the reflectivity of the interface. This model is only valid if the roughness is small compared to the film thickness. If this is not the case other models have to be used, e.g. the electron density profile might be represented by a stack of very thin flat layers. This is known as arbitrary density model [27].

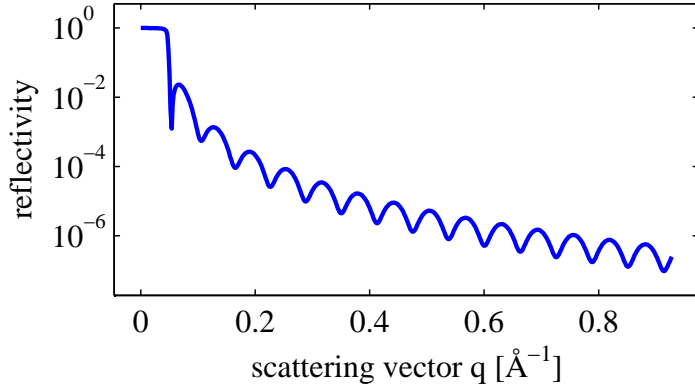


**Fig. 2.11:** Reflectivity curve for a magnetite layer on MgO. Up to the critical angle total external reflection is observed. After that the intensity is decreasing. The observed oscillations originate from an interference between the beams reflected at the film/vacuum and the substrate/film interface.

Fig. 2.11 shows a calculated reflectivity curve for a magnetite layer on MgO(001). Up to the critical angle for total reflection the reflectivity is 1, i.e. total reflection occurs. Afterwards, the intensity is dropping with  $1/q^4$ . In addition intensity oscillations occur, which originate from interference between the x-rays reflected at the film/vacuum and at the substrate/film interface. The periodicity of these oscillations is characteristic for the film thickness. For such a simple one-layer-plus-substrate model the thickness can be estimated to  $d = \frac{2\pi}{\Delta q} \approx \frac{\lambda}{2\Delta\alpha_i}$  where the distance between two maxima is given by  $\Delta q$  and  $\Delta\alpha_i$ .

## 2.5. Low-energy electron diffraction

For electron and x-ray diffraction in principle the same Bragg formula is valid. Also the wavelength used in both low-energy electron and x-ray diffraction is in the same range. The major difference between electrons and x-rays is the scattering cross section, which is orders of magnitudes larger for electrons compared to the photons used in x-ray diffraction. Thus, the penetration depth of electrons is much smaller and as a result the surface sensitivity is considerably higher. With low-energy electron diffraction (LEED) usually only the near surface region is accessible (typically  $\approx 3$  atomic layers). As a consequence in reciprocal space the Bragg peaks which are observed are smeared out in vertical direction and become Bragg rods similar to the surface scattering in the x-ray case. In contrast to the x-ray case almost no bulk information contributes when using electron diffraction due to small penetration depth of the electrons. Thus, only the rods in vertical direction originating from the surface can be observed. However, a small bulk contribution as well as atomic steps on the surface typically lead to a modulation of the intensity along the vertical rods.

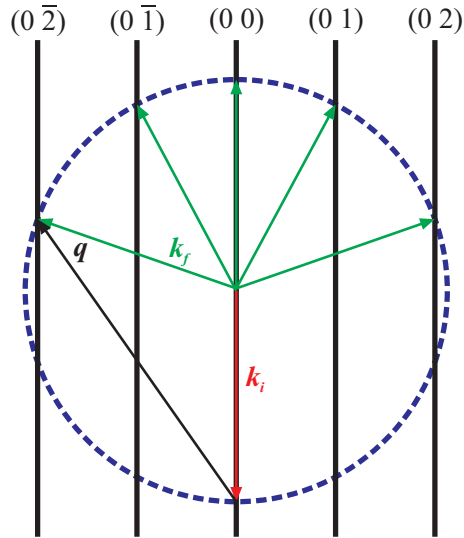


**Fig. 2.12:** Ewald construction for a LEED setup using normal incidence. The Ewald sphere (dashed line) is defined by all possible positions for the wave vector of the diffracted beam. The rods (solid line) are the positions in reciprocal space where the 2D Laue conditions are fulfilled. At the interception points of the rods and Ewald sphere diffraction spots can be observed with LEED.

In a typical LEED experiment a fixed normal incidence beam is used and the diffracted intensity is recorded using a two dimensional detector (usually a fluorescent screen). According to the Ewald construction (cf. Fig. 2.12), diffraction can be observed whenever the Ewald sphere is intercepting a Bragg rod. The surface of the Ewald sphere is defined by the set of all possible exiting wave vectors  $\mathbf{k}_f$ . Its radius is equal to the length of the wave vector  $|\mathbf{k}_f|$ . The 2D detector covers the hemisphere above the sample (or at least a large amount of it) and all peaks originating from wave vectors pointing towards the direction of the detector can be observed on the screen. The 2D spot pattern shows the symmetry of the reciprocal space in lateral direction. The electron beam is typically focused on the detector to achieve narrow peaks. However, it is also possible to focus on the sample if only a very small sample area shall be studied.

Since the incidence angle is usually fixed in LEED experiments the only possibility to change the scattering condition is to change the electron energy, i.e. its wavelength. By changing the wavelength the radius of the Ewald sphere changes and therefore the position where the sphere and the Bragg rod intercept also varies.

Due to the large scattering probability of electrons a quantitative analysis would require the use of a complex multiple scattering theory. However, already from a qualitative analysis of the diffraction pattern a lot of information can be obtained. Most obvious is the lateral symmetry of the crystal surface, which can be derived from the symmetry of the diffraction spots. In addition to that superstructure peaks are frequently observed. These additional peaks originate from changes in the surface structure compared to the bulk structure, and leads to a larger surface unit cell. The changes in the surface structure are typically related to uncompensated bounds or polar surfaces. A famous example for such a superstructure is the  $(7 \times 7)$  superstructure of the Si(111) surface [30].

A typical LEED setup consists of two major parts: the electron gun and the fluorescence screen. Fig. 2.13 shows a schematic drawing of a three-grid LEED setup [31]. The electron gun typically has an energy range from 20 to 500 eV and consists of a filament and a Wehnelt cylinder (W). The electrons emitted by the filament are collimated by the Wehnelt cylinder and afterwards pass an electrostatic lens (apertures A, B, C, D). The lens is used to accelerate and focus the electron beam. The focused electron beam is hitting the sample at normal incidence and the scattered electrons are detected by a spherical fluorescent screen (collector). Since only high energy electrons are visible on the fluorescent screen the screen has to be put to positively charged high voltage ( $\approx 5$  keV) to accelerate the low energy electrons. By biasing the middle grid negatively the background scattering from inelastic scattered electrons can be suppressed. The inner grid as well as apertures A and D are usually put to the same potential (ground) to create a field-free area between sample and the fluorescent screen system.

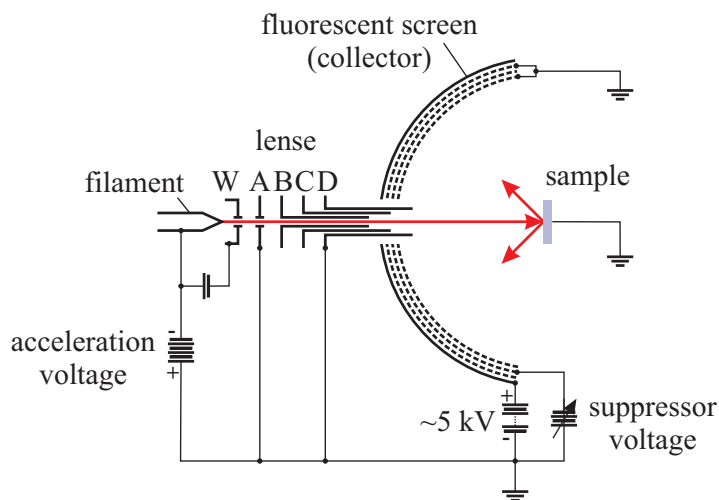


**Fig. 2.13:** A three-grid LEED setup [31] with a filament emitting the electrons, Wehnelt cylinder (W), electrostatic lens (A, B, C, D), and the fluorescent screen with the three-grid system for background suppression and electron acceleration.

## 2.6. X-ray photoemission spectroscopy

X-ray photoemission spectroscopy (XPS) or also known as electron spectroscopy for chemical analysis (ESCA) is a spectroscopic technique to study the electronic structure of the occupied states in a material [19]. The basis of this technique is the photoelectric effect. A photon with the energy  $\hbar\omega$  is absorbed by an electron which originally is in a state with the binding energy  $E_i$  relative to the Fermi level  $E_{Fermi}$ . The electron leaves the solid with a kinetic energy of

$$E_{kin} = \hbar\omega - E_i - \phi \quad (2.44)$$

where  $\phi = E_{vacuum} - E_{Fermi}$  is the work function of the material, i.e. the energy necessary to remove an electron from a solid. To excite electrons from the core levels photon energies in the x-ray region are necessary. For studying the valence band photon energies in the ultra violet region are typically used due to the larger cross section.

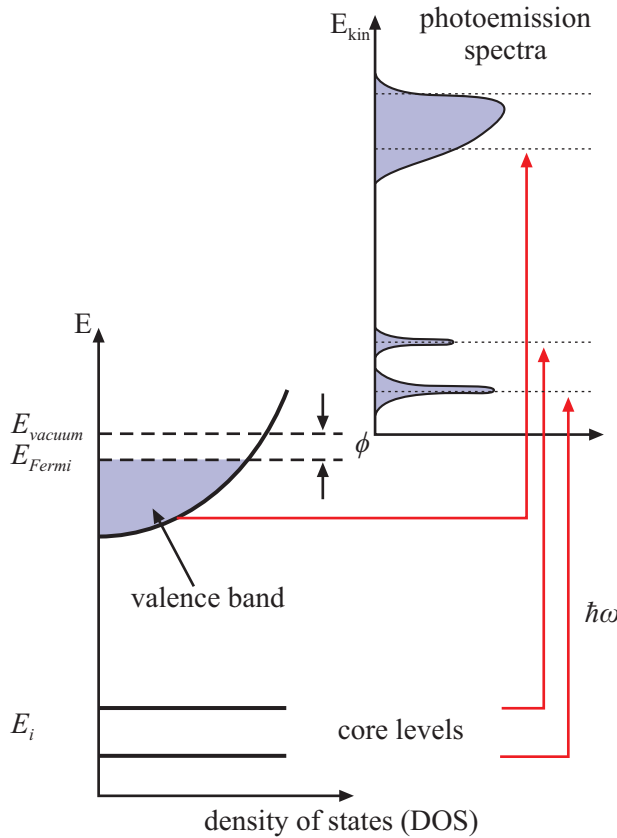


**Fig. 2.14:** Schematical drawing of the photoemission excitation process. Electrons are excited by incoming photons with an energy  $\hbar\omega$  and are emitted with a kinetic energy  $E_{kin} = \hbar\omega - E_i - \phi$ .

To observe a photoelectron the photon energy has to be larger than  $E_i + \phi$ , the electron emission has to be directed towards the sample surface and the electron should not be scattered on its path leaving the solid. Therefore, the mean free path of the electron within a solid is an important issue in XPS. The mean free path depends on both the investigated material as well as the kinetic energy of the electron. For the kinetic energies used by XPS the electron mean free path is in the order of some Ångstroms up to a few nanometer. Thus, XPS is a technique which is very surface sensitive. However, it is possible to even increase the surface sensitivity by illuminating the sample at grazing incidence below the critical angle of total external

reflection and/or collect photoelectrons at grazing exit. The bulk sensitivity can be increased by increasing the photon energy and therefore the kinetic energy of the photoelectrons. This method is known as HAXPES (hard x-ray photoemission spectroscopy).

Eq. 2.44 gives a direct relation between the kinetic energy of the photoelectrons and the binding energy of the state from which the photoelectrons were emitted. Thus, using XPS one probes the binding energy of the occupied states. These binding energies are characteristic for specific elements. Since, the chemical environment of an atom within a material influences the electronic structure of the atom, the binding energy is also influenced by the chemical environment. As a result the characteristic peak positions are shifting typically by 1 to 10 eV. Hence, XPS can be used to determine the chemical composition of material compounds.

In addition to the main line peaks also satellite peaks may occur. Shake-up and shake-down satellites occur when the photoelectron excites an electron from the valence band. In case of shake-up satellites the valence band electron is excited to a higher energy level and a satellite peak occurs. Since the photoelectron loses energy when exciting the valence band electron the satellite are shifted by a few eV to lower kinetic energies (higher binding energies) compared to the main line. Shake-off satellites occur when the excited valence band electron leaves the ion.

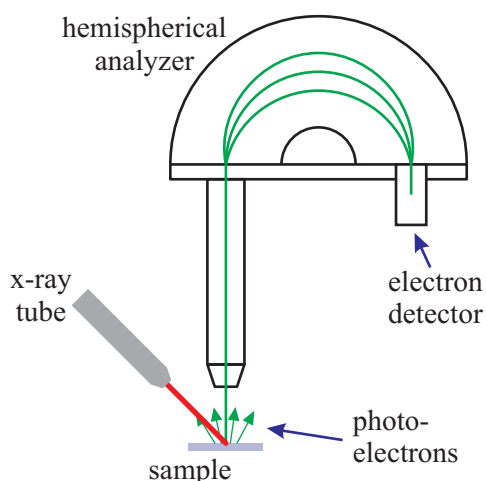


**Fig. 2.15:** Typical XPS setup consisting of an x-ray tube and a hemispherical analyzer. Due to the incoming x-ray beam the sample emits photoelectrons. By applying electric fields in the analyzer only electrons of a certain energy can pass the analyzer and can be detected at the detector.

Due to the small mean free path of electrons at ambient conditions, XPS experiments are usually performed under ultra high vacuum conditions. A typical XPS setup consists of an x-ray source, either x-ray tubes or synchrotron radiation are used, and an energy dispersive electron detector. In case of XPS mainly hemispherical analyzers are used. By applying electric fields the electrons entering the analyzer are forced on a circular trajectory where only electrons with a desired kinetic energy can pass the analyzer and reach the electron detector. To increase the efficiency, the electrons which enter the analyzer at different angles are focused on the detector.

## 3. Properties of iron oxides and iron oxide thin films

This chapter will take a closer look onto the material investigated in this work: iron oxide. Here, the properties of both bulk iron oxide as well as iron oxide thin films will be discussed.

### 3.1. Iron oxide

Iron oxides can be found in three stoichiometric forms: FeO, Fe<sub>3</sub>O<sub>4</sub>, and Fe<sub>2</sub>O<sub>3</sub>. These stoichiometries are also often characterized by the charge of the iron ions. FeO contains exclusively Fe<sup>2+</sup> ions, Fe<sub>3</sub>O<sub>4</sub> contains both Fe<sup>2+</sup> and Fe<sup>3+</sup> ions, and Fe<sub>2</sub>O<sub>3</sub> contains only Fe<sup>3+</sup> ions. Fig. 3.1 shows the bulk phase diagram for the different iron oxides as a function of temperature and oxygen partial pressure obtained by Kettler et al. from theoretical calculations [32]. At ambient conditions Fe<sub>2</sub>O<sub>3</sub> is the most stable phase. However, the calculated free energies suggest that, especially at low pressures, different oxides might coexist as metastable phases.

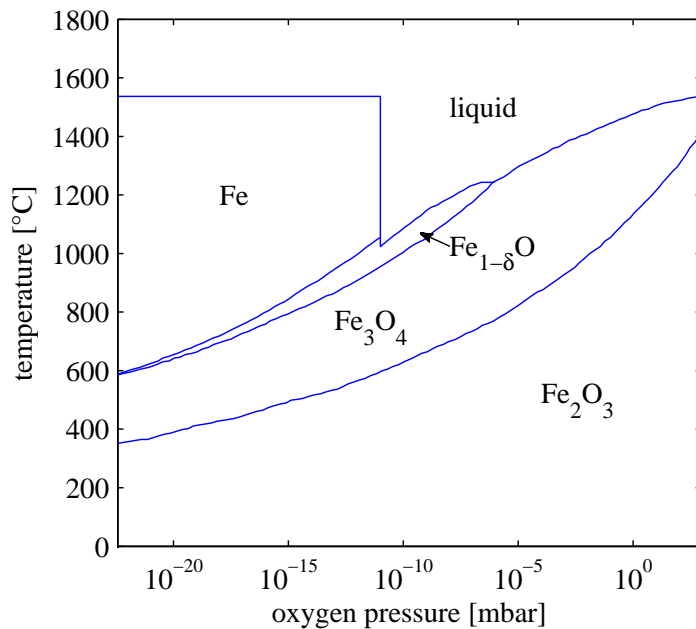


**Fig. 3.1:** Phase diagram as a function of temperature and oxygen partial pressure obtained by Kettler et al. from theoretical calculations [32].

#### Wüstite (FeO)

Wüstite is the iron oxide with the lowest oxidation state of all iron oxides containing only divalent iron. Since it is not stable under ambient conditions it usually forms a non-stoichiometric

iron deficient phase [33]. Therefore, it is often referred to as  $\text{Fe}_{1-\delta}\text{O}$  where  $\delta$  ranges from 0.04 to 0.12. Wüstite crystallizes in the rock salt ( $\text{NaCl}$ ) structure which consists of two fcc<sup>1</sup> lattices shifted by half a unit cell with respect to each other along one lattice vector.  $\text{FeO}$  has a bulk lattice constant of  $a = 4.332 \text{ \AA}$ . It is antiferromagnetic and electrically insulating.

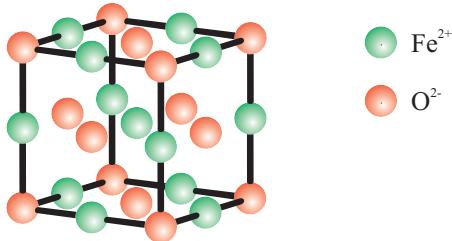


**Fig. 3.2:** Sketch of the wüstite unit cell.

### Magnetite ( $\text{Fe}_3\text{O}_4$ )

Magnetite is an iron oxide containing divalent and trivalent iron. Magnetite crystallizes in the inverse spinel structure and has a bulk lattice constant of  $a = 8.3963 \text{ \AA}$ .

The generalized formula for the inverse spinel structure is given by  $\text{B}(\text{AB})\text{C}_4$  and it has a cubic symmetry. Tetrahedrally coordinated sites (A sites) are occupied by cations of type B, while octahedrally coordinated sites (B sites) are occupied by randomly distributed A and B type cations. The anions (type C) form an fcc sublattice.

In case of magnetite type A ions are  $\text{Fe}^{2+}$ , type B ions  $\text{Fe}^{3+}$  and type C ions  $\text{O}^{2-}$ . Thus, the oxygen anions are forming a fcc sublattice,  $\text{Fe}^{3+}$  ions occupy tetrahedral sites, while the octahedral sites are occupied by randomly distributed  $\text{Fe}^{2+}$  and  $\text{Fe}^{3+}$  ions. An important point to consider about spinel type unit cells is the anion parameter  $u$  describing a distortion of the anion fcc sublattice. For magnetite the anion parameter  $u = 0.2548$  is almost matching the ideal value of  $u = 0.25$  for an undistorted fcc anion sublattice [34].

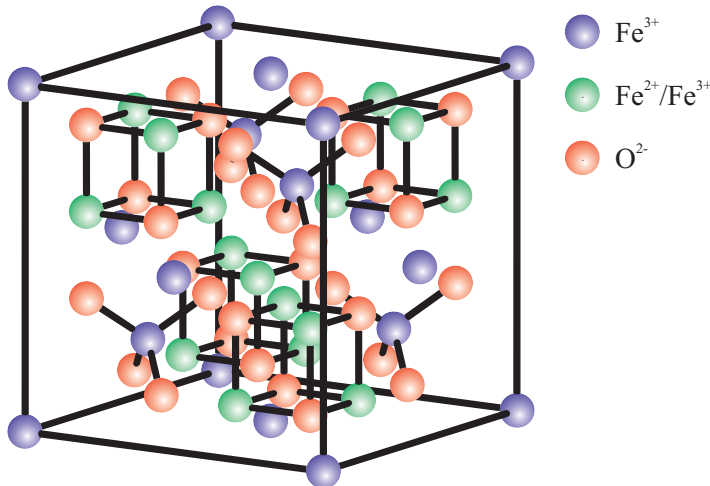


**Fig. 3.3:** Sketch of the magnetite unit cell.

Due to the antiparallel coupling of the spin moments from A and B sites magnetite is ferrimagnetic with a net magnetic moment of  $4\mu_B$ . It is a half-metal with full spin polarization

<sup>1</sup>face centered cubic

at the Fermi level. Another important property of magnetite is that it has a metal/insulator transition at about  $T_V = 125$  K, known as Verwey transition [35]. Below the Verwey temperature the conductivity as well as the magnetization are dropping by several orders of magnitude. This behavior is attributed to a charge ordering in the tetrahedral sites. The actual temperature of the Verwey transition depends on the purity of the magnetite phase and already small deviations from the magnetite stoichiometry lead to a broadening of the transition. Hence, a sharp Verwey transition is believed to be a good indication for the purity of the magnetite stoichiometry and a high crystallinity.

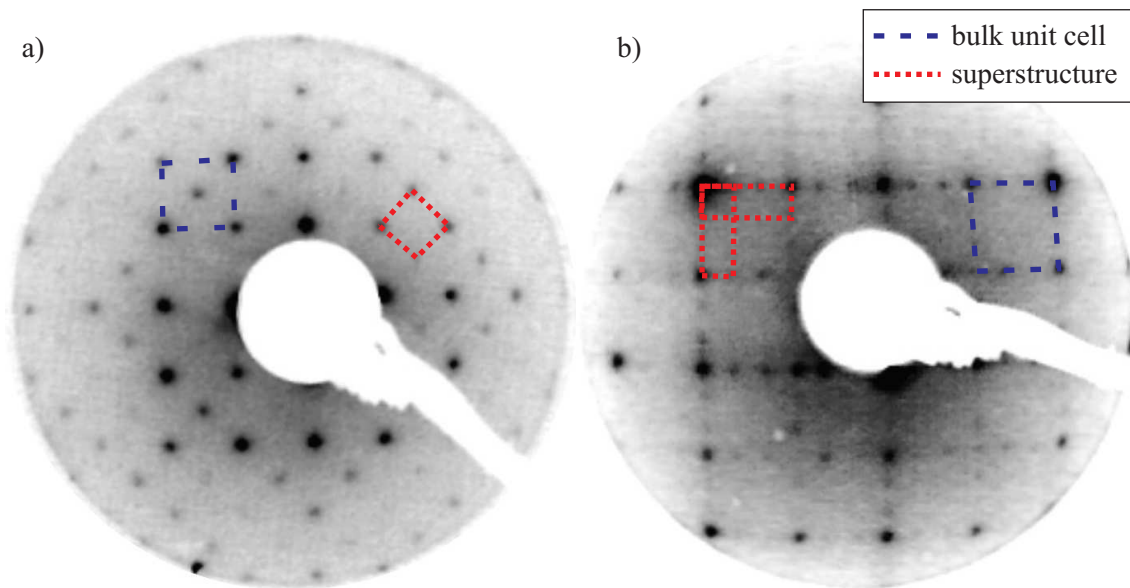


**Fig. 3.4:** a) typical LEED image from a magnetite thin film showing the  $(\sqrt{2} \times \sqrt{2})R45$  superstructure of the reconstructed surface. b) LEED image (taken from [36]) of a magnetite film grown on MgO which was annealed at  $600^\circ\text{C}$  after deposition showing the typical  $(3 \times 1)$  superstructure for magnetite films contaminated by magnesium segregation.

The (001) surface of magnetite typically shows a  $(\sqrt{2} \times \sqrt{2})R45$  superstructure (cf. Fig 3.4a) which is reported in large quantity in the literature [37–39]. In order to explain the superstructure two different models have been purposed. One assuming a so called *A-layer* termination, and the other model assuming a *B-layer* termination [40]. As suggested by the names the A-layer termination model assumes that the top surface layer is consisting of A sites, i.e. ions tetrahedrally coordinated in the bulk. To compensate for the polarity each second row is missing and thus leading to a superstructure. The B-layer termination model assumes that the terminating top surface layer is consisting of B sites, i.e. iron ions which are octahedrally coordinated in the bulk, as well as oxygen anions, but with the ions are shifted compared to their bulk positions [39].

### Maghemite ( $\gamma\text{-Fe}_2\text{O}_3$ ) and hematite ( $\alpha\text{-Fe}_2\text{O}_3$ )

Maghemite and hematite contain only trivalent iron. Hematite crystallizes in the trigonal corundum ( $\text{Al}_2\text{O}_3$ ) structure with lattice constants  $a = b = 5.112 \text{ \AA}$  and  $c = 13.82 \text{ \AA}$  and lattice angles  $\alpha = \beta = 90^\circ$  and  $\gamma = 120^\circ$ . Maghemite crystallizes in a defect spinel structure

similar to magnetite with a lattice constant of  $a = 8.3515 \text{ \AA}$ . In contrast to magnetite only  $13\frac{1}{3}$  of the 16 octahedral B sites are occupied randomly distributed. Like magnetite, maghemite is also ferrimagnetic while hematite is antiferromagnetic.

Concerning bulk structures hematite is the more stable phase of  $\text{Fe}_2\text{O}_3$ . However, the structure of  $\text{Fe}_2\text{O}_3$  thin films strongly depends on the substrate. While e.g.  $\text{Fe}_2\text{O}_3$  films on  $\text{Al}_2\text{O}_3$  typically form  $\alpha\text{-Fe}_2\text{O}_3$ ,  $\text{Fe}_2\text{O}_3$  films typically form  $\gamma\text{-Fe}_2\text{O}_3$  on  $\text{MgO}(001)$ .

### X-ray photoelectron spectroscopy

Iron oxides of different compositions have been studied by XPS in the past. The Fe2p region is generally used to give a rough estimate of the oxide phase since the Fe2p peak has a characteristic satellite structure for each oxide phase [41,42]. Fig. 3.5 shows the experimental spectra corresponding to the three iron oxide phases from Yamashita et al. [41]. For  $\text{Fe}_{1-\delta}\text{O}$  and  $\text{Fe}_2\text{O}_3$  satellite peaks with characteristic peak positions occur between the  $\text{Fe}2p_{1/2}$  and the  $\text{Fe}2p_{3/2}$  signals. For  $\text{Fe}_3\text{O}_4$  containing divalent and trivalent iron ions in principle both satellite peaks should occur. However, due to the superposition of both peaks an intensity plateau is formed so that no peak can be distinguished. Thus, by observing the peak structure of the Fe2p peak region it is possible to roughly estimate the oxide phase. To obtain more precise values for the ratio of iron and oxygen, however, a more detailed analysis is necessary.

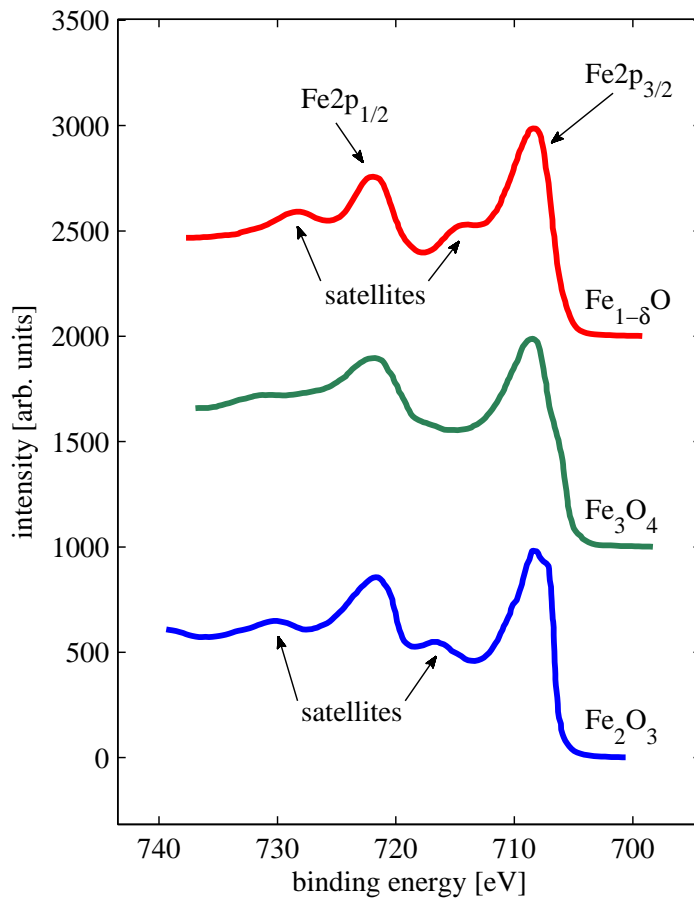


**Fig. 3.5:** XPS spectra for different iron oxide phases as determined by Yamashita et al. [41]

### 3.2. Iron oxide thin films on MgO(001)

For the growth of epitaxial iron oxide thin films magnesium oxide (MgO) is one of the most common used substrates. Typically, the iron oxide is grown on the (001) plane of a MgO single crystal since the lattice mismatch between MgO and the cubic iron oxides is very low. Concerning the doubled MgO lattice constant which is slightly bigger than that of magnetite and maghemite the misfit is  $\epsilon = -0.3\%$  and  $\epsilon = -0.8\%$ , respectively. The FeO lattice constant is slightly larger than the MgO lattice constant and the misfit is  $\epsilon = 2.6\%$ . Thus, iron oxide films, especially magnetite, can be grown on MgO almost without any strain effects.

#### Magnesium oxide

Magnesium oxide crystallizes in the rock salt structure, like wüstite, with a lattice constant of  $a = 4.2117 \text{ \AA}$ . It is electrically insulating and diamagnetic.

#### Epitaxy

The growth of iron oxide thin films on magnesium oxide as well as other substrates (e.g.  $\text{Al}_2\text{O}_3$ ) has been extensively studied in the past by a large quantity of research groups, e.g. [38, 43–45]. In the following the most important results from these studies will be discussed.

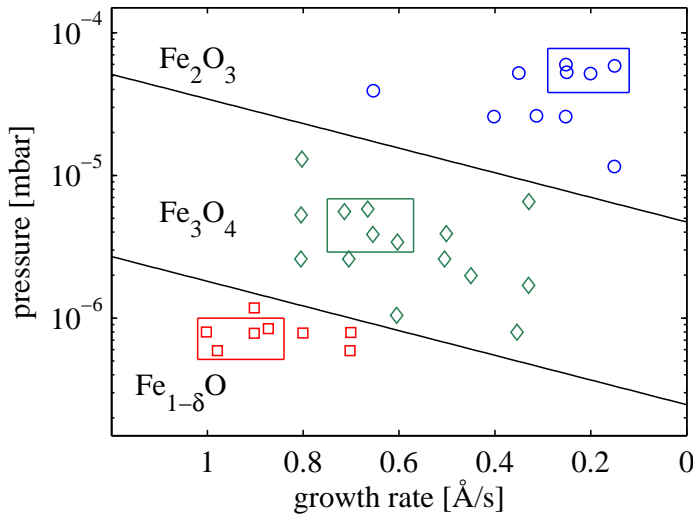


**Fig. 3.6:** Phase diagram for the deposition of iron oxide thin films using plasma assisted MBE obtained from Gao et al. [46]. The border between the different phases is indicated by solid lines while the boxes mark the optimal deposition conditions for each phase. The  $\text{Fe}_2\text{O}_3$  data includes both  $\alpha\text{-Fe}_2\text{O}_3$  as well as  $\gamma\text{-Fe}_2\text{O}_3$  depending on the used substrate.

Iron oxide thin films are mainly prepared using reactive approaches [38, 46, 47]. Thus, pure iron (or in rare cases also iron oxide) is evaporated in the presence of oxygen. Using such a deposition approach the quality and stoichiometry of the film strongly depends on the oxygen concentration given by its partial pressure as well as the deposition rate. Fig. 3.6 shows a phase diagram as a function of growth rate and oxygen partial pressure for the deposition of epitaxial iron oxide films by plasma assisted MBE obtained by Gao et al. [46] using different types of substrate.

The phase diagram clearly shows that in general higher growth rates result in a lower oxidation state while higher oxygen pressures lead to a higher oxidation state. Both can easily be

explained by the fact that a higher concentration of oxygen as well as a lower deposition rate increase the reaction probability of iron and oxygen. The phase diagram was obtained using oxygen plasma instead of molecular oxygen as done in this work. Plasma assisted MBE is similar to reactive MBE. But instead of molecular oxygen an oxygen plasma is used. Therefore, the reaction probability between oxygen and iron changes and the exact values in the phase diagram might differ from the reactive MBE case but the general relation between growth rate, oxygen concentration, and the oxidation state can be transferred to this deposition technique as well.

Another important parameter for the deposition of epitaxial thin films is the substrate temperature. In several different studies the influence of the substrate temperature on the film structure is discussed. Although, Voogt et al. [48] observed layer-by-layer growth of magnetite over a wide range of studied substrate temperatures (from room temperature up to 450°C), generally 250°C is assumed to be the lower limit for the deposition of high quality magnetite films. However, several studies showed that higher substrate temperatures lead to a segregation of substrate magnesium into the iron oxide film so that magnesioferrite ( $\text{MgFe}_2\text{O}_4$ ) is formed [46, 49, 50]. Like magnetite magnesioferrite has also a spinel type structure with a lattice constant of  $a = 8.3866 \text{ \AA}$  which is very similar to the magnetite lattice constant. Therefore, it is quite difficult to distinguish between magnetite and magnesioferrite films using x-ray diffraction. However, magnesioferrite shows a different superstructure. Both a  $(3 \times 1)$  superstructure (cf. Fig 3.4b) [36, 51] and a  $(4 \times 1)$  superstructure [37] have been observed by LEED. Studies on the magnetic properties of magnetite films on MgO show that the segregation of magnesium leads to a weakening of the magnetic properties of the film as well as a suppression of the Verwey transition.

### Antiphase boundaries

Since the magnetite and maghemite lattice constants are doubled in size compared to the MgO lattice constant such epitaxial films grown on MgO show antiphase boundaries (APB) [45, 52–54]. When two or more iron oxide islands start to grow from different nucleation centers on a MgO surface the lateral size of these islands increases until the borders of the islands meet. Since the MgO unit cell is half the size of the magnetite unit cell the spacing between two nucleation centers might be  $n$  or  $n + \frac{1}{2}$  times the magnetite unit cell size ( $n$  is an integer number). In the latter case an antiphase boundary occurs where both islands meet. Detailed studies on APBs could show that the density of APBs is related to the deposition temperature [45]. At higher deposition rates a lower density of APBs can be observed due to the higher mobility of the ions adsorbed at the surface. The APB density can also be reduced by post-deposition annealing. Like the segregation of magnesium the formation of APBs also leads to a reduction of the magnetic properties of magnetite films and suppresses the Verwey transition [45, 54].

## 3.3. The surface lattice coordinate system for the reciprocal space

As described in Sec. 2.3 for x-ray diffraction usually the reciprocal space is defined by the reciprocal lattice vectors. When performing surface x-ray diffraction it is often desirable to use a surface specific coordinate system and therefore obtain also surface specific reciprocal lattice vectors.

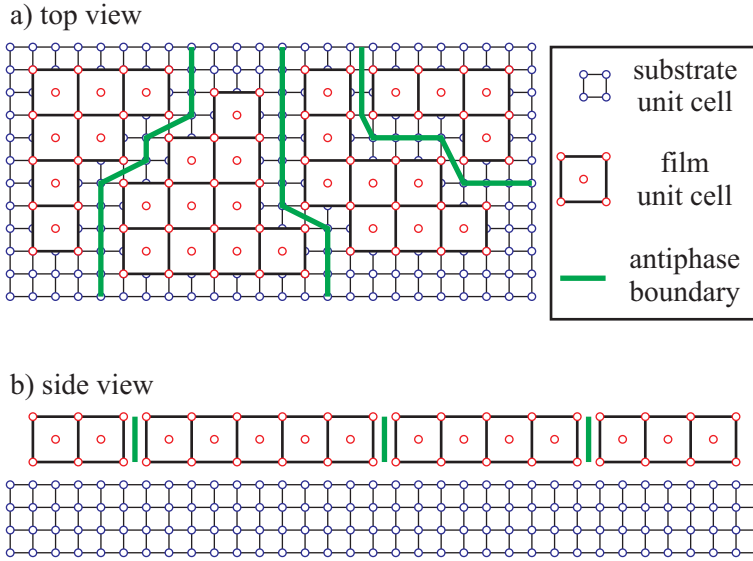


**Fig. 3.7:** Illustration of a thin film grown on a substrate showing antiphase boundaries in a) side view and b) top view.

For a layer system of one or more thin films on a substrate it is also reasonable to define a common coordinate system for the reciprocal space. Here, a typical choice is a coordinate system, which is related to the surface unit cell of the substrate as a common coordinate system.

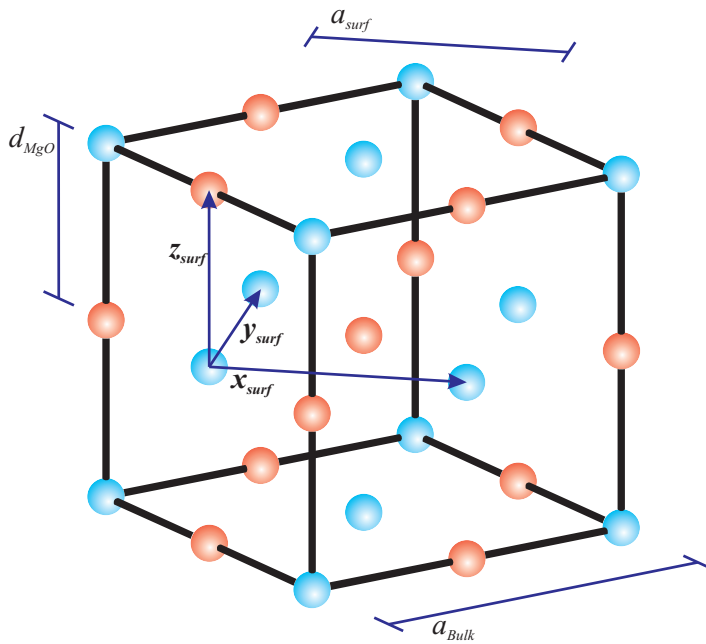


**Fig. 3.8:** Sketch of the MgO unit cell with the surface coordinate system used for indexing the reciprocal space in this work.

In this work the MgO(001) surface coordinate system is used for the description of iron oxide thin films grown on MgO. This surface coordinate system is half the size of the bulk unit cell in vertical direction and rotated by  $45^\circ$  in lateral direction as illustrated in Fig. 3.8. Thus, the basis vector pointing in vertical direction  $z_{surf}$  gives the MgO(001) layer distance  $d_{MgO} = 2.106 \text{ \AA}$ .

The transformation matrices to convert from the bulk coordinate system of MgO and FeO

(rock salt type unit cell) into the surface coordinate system are given by

$$T = \begin{pmatrix} 1 & 1 & 0 \\ 1 & -1 & 0 \\ 0 & 0 & 2 \end{pmatrix} \quad \text{for the real space and by} \quad T^* = \begin{pmatrix} \frac{1}{2} & \frac{1}{2} & 0 \\ \frac{1}{2} & -\frac{1}{2} & 0 \\ 0 & 0 & \frac{1}{2} \end{pmatrix} \quad (3.1)$$

for the reciprocal space. The respective transformation matrices for  $\text{Fe}_3\text{O}_4$  and  $\gamma\text{-Fe}_2\text{O}_3$  (spinel type unit cell) are given by

$$T = \begin{pmatrix} 2 & 2 & 0 \\ 2 & -2 & 0 \\ 0 & 0 & 4 \end{pmatrix} \quad \text{and} \quad T^* = \begin{pmatrix} \frac{1}{4} & \frac{1}{4} & 0 \\ \frac{1}{4} & -\frac{1}{4} & 0 \\ 0 & 0 & \frac{1}{4} \end{pmatrix}. \quad (3.2)$$

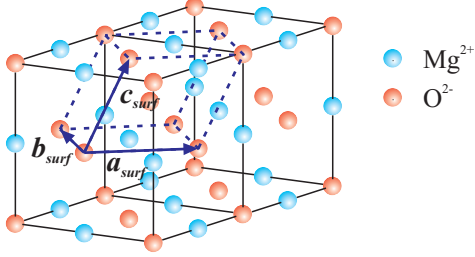


**Fig. 3.9:** Sketch of the MgO surface unit cell.

Using this coordinate system the lattice vectors of the MgO surface unit cell are given by

$$\mathbf{a}_{surf} = \begin{pmatrix} 1 \\ 0 \\ 0 \end{pmatrix}, \quad \mathbf{b}_{surf} = \begin{pmatrix} 0 \\ 1 \\ 0 \end{pmatrix}, \quad \mathbf{c}_{surf} = \begin{pmatrix} \frac{1}{2} \\ \frac{1}{2} \\ 1 \end{pmatrix}. \quad (3.3)$$

Hence, the unit cell contains only one  $\text{Mg}^{2+}$  one  $\text{O}^{2-}$  while the bulk unit cell definition contains four ions of both types. Although, this unit cell shows a lower symmetry than the bulk unit cell it offers several advantages, especially concerning the simulation of the diffracted intensity. On the one hand the number of unit cells in vertical direction has to be doubled compared to the bulk case when describing a crystal of the same height. On the other hand the number of atoms per unit cell is reduced. Since, the calculation time using the formulas derived in Sec. 2.3 increases with the number of atoms per unit cell but is independent of the number of unit cells per film, smaller unit cells with less atoms automatically lead to a better performance of the simulation. Another advantage of the reduced unit cell size, especially in vertical direction is, that it leads to a more realistic model describing the film structure. As explained in more detail in Sec. 4.5 only integer numbers of atomic layers, or more precise of unit cells, can be used within the model. When depositing crystalline thin films it happens very likely that the top layer might not form a complete but a truncated unit cell. This behavior can be described much better using unit cells as small as possible in vertical direction.

Fig. 3.10 shows the  $H = 0$  plane of the reciprocal space for the iron oxide/MgO(001) system

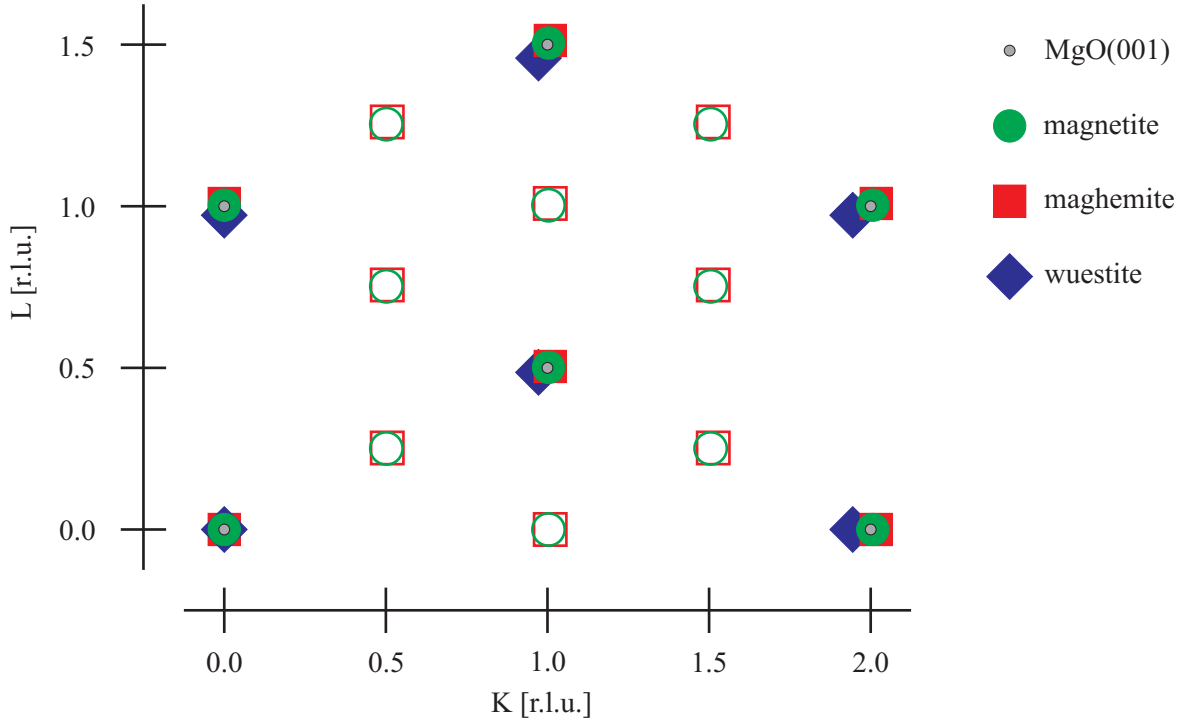


**Fig. 3.10:** Sketch of the  $H = 0$  plane of the reciprocal space for the MgO(001)/iron oxide system assuming the bulk lattice parameters. Open symbols indicate Bragg peaks originating exclusively from tetrahedral sites.

using the MgO(001) surface coordinate system for indexing. Bulk lattice parameters are used to calculate the position of the Bragg peaks shown in Fig. 3.10. Since MgO as well as FeO have essentially the same crystal structure they exhibit Bragg peaks at approximately the same positions except for a small deviation due to the different lattice constants.  $\text{Fe}_3\text{O}_4$  as well as  $\gamma\text{-Fe}_2\text{O}_3$  have additional peaks due to their larger unit cells. These additional peaks originate exclusively from the tetrahedral sites of the spinel structure.

The contribution of the different types of sites to the structure factor  $F_{total} = F_{tetrahedral} + F_{octahedral} + F_{oxygen}$  is shown in Fig. 3.11 a) and d). Fig. 3.11 b) and e) show the total structure factor while Fig. 3.11 c) and f) show the diffracted intensity from a magnetite film. Here, it is clearly visible that some Bragg peaks, e.g.  $(01\frac{1}{2})$ , originate exclusively from iron ions on octahedral sites and oxygen ions while other Bragg peaks, e.g.  $(011)$ , originate exclusively from iron ions on tetrahedral sites. Therefore, it is possible by studying certain Bragg peaks to distinguish between the tetrahedral and octahedral sites. However, as shown in Fig. 3.10 the Bragg peaks originating from octahedral sites are always overlapping with the Bragg peaks of the MgO substrate.

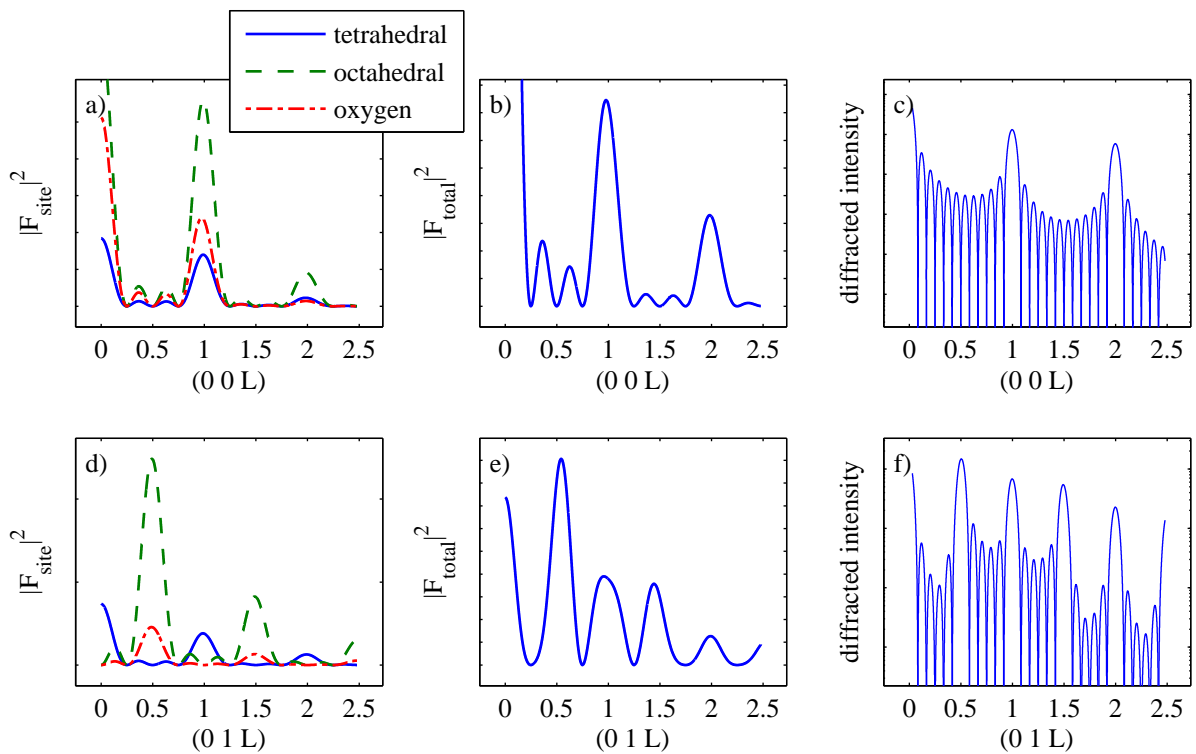


**Fig. 3.11:** a), d) contribution of the different magnetite sites to the structure factor. The solid line shows the contribution from iron ions at the tetrahedral sites, the dashed line iron ions at the octahedral sites and the dash-dotted line the contribution from oxygen ions. b), e) The total structure factor of magnetite. c), f) the diffracted intensity from a magnetite film. The top row shows calculations for the  $(00L)$  direction, the bottom row for the  $(01L)$  direction.

## 4. Experimental setup and data analysis for synchrotron radiation experiments

X-ray diffraction and reflectivity experiments are generally performed using diffractometers. A diffractometer is a device to position sample, detector and in some cases also the x-ray source in a way that the desired scattering condition is fulfilled. XRD and XRR experiments in this work are performed using synchrotron radiation sources. Compared to conventional lab sources the synchrotron light has several important advantages

1. higher intensity
2. tunable energy/wavelength
3. smaller beam size
4. smaller divergence.

The performance of x-ray sources, especially in case of synchrotron radiation sources, is usually measured by the brilliance of the x-ray beam. The brilliance  $B$  of the x-ray beam

$$[B] = \frac{\text{photons/second}}{(\text{mrad})^2 (\text{mm}^2 \text{ source area}) (0.1\% \text{ bandwidth})} \quad (4.1)$$

is defined by the number of photons per second, the horizontal and vertical divergence (given in mrad), the beam size (in  $\text{mm}^2$ ) within an energy bandwidth of 0.1% [15]. In general the brilliance is a function of the energy. Thus, the brilliance as a function of photon energy is an important x-ray source characteristic. Within the past decades there have been a lot of improvements on the brilliance of x-ray sources. Starting with the first x-ray tubes to modern third generation synchrotron radiation sources and free electron lasers (FEL) the brilliance has increased by several orders of magnitude.

In the following the generation of synchrotron radiation at modern sources will be explained as well as a typical setup of an x-ray scattering beamline using the beamlines W1 [23, 55] (DORIS, DESY) and P08 [56] (PETRA III, DESY), where the experiments presented in this thesis were performed, as an example. More details on the generation of synchrotron radiation can be found in the literature [15, 16]. In addition, the used scattering geometries, correction factors to the measured intensity, and the analysis of diffraction data will be discussed.

### 4.1. Generation of synchrotron radiation

Synchrotron radiation was first observed at a special type of particle accelerator called synchrotron from which it got its name. However, synchrotron radiation has become a general name for radiation originating from charged particles (typically electrons or positrons) travelling near the speed of light. Nowadays, dedicated synchrotron radiation sources are typically storage rings where electrons (or in some cases also positrons) are traveling at a constant

speed close to the speed of light. In contrast to particle accelerators they provide a very stable particle beam, which results in a very stable radiated beam, and the spectrum of the emitted radiation is not shifting due to the change in particle speed. Modern storage rings are not exactly circular, but have a polygon like shape. They consist of straight sections which are connected by so-called bending magnets deflecting the particles from one straight section into the adjacent one. The straight sections usually host insertion devices as explained below. The basic consideration for the generation of synchrotron radiation is that charged particles which are accelerated emit electromagnetic radiation. Traveling at non-relativistic velocities the radiation of the particle has a dipole radiation pattern. This pattern has a toroidal shape with the main axis pointing into the direction of the accelerating force. For particles traveling close the speed of light one has to consider relativistic effects and the Doppler shift. This results into a change of the radiation pattern. The electromagnetic radiation becomes a cone with its center pointing into the direction of propagation.

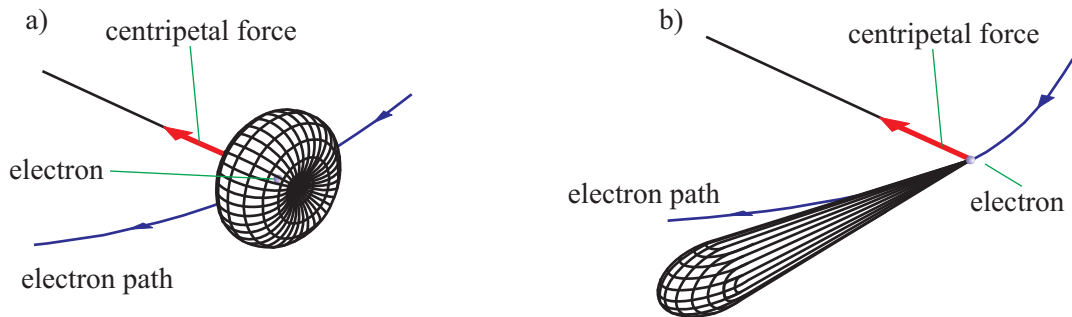


**Fig. 4.1:** Radiation pattern of an electron traveling along a circular path a) with non-relativistic velocity and b) with a velocity close to the speed of light. Taken from [57] and revised.

Since the intensity of the emitted radiation is related to the mass  $m$  of the particle by  $\frac{1}{m^4}$  only light particles such as electrons and positrons can practically be used to generate synchrotron radiation [16]. In most synchrotron radiation sources electrons are used since they can be generated more easily than positrons which are antiparticles. However, due to collisions of the electrons or positrons with residual gas positively charged particles are generated in storage rings. Electron beams attract these particles and thus keep them in the path of the electrons. This often leads to a reduction of the electron beam lifetime. This problem can be avoided by using positrons instead of electrons. In the storage rings DORIS and PETRA III, therefore, positrons are used.

The most basic device to generate synchrotron radiation is the bending magnet. By forcing the charged particles onto a circular path they are accelerated and emit radiation. The emission spectrum of a bending magnet depends on the bending radius and the energy of the particles. Since the bending radius is usually defined by the storage ring geometry the emitted spectrum of the bending magnets is also determined by it.

To achieve higher intensities of the emitted radiation and smaller beam sizes special insertion devices have been developed, which are placed into straight sections of the storage rings. These devices consist of periodically alternating magnetic structures forcing the electrons on an oscillating path. Thus, an insertion device is an accumulation of many bending magnets. There are two different kinds of insertion devices, the wiggler and the undulator. The main difference between both types is the strength of the magnetic field and the displacement of

#### 4.2. Setup of an x-ray scattering beamline for (grazing incidence) x-ray diffraction and x-ray reflectivity

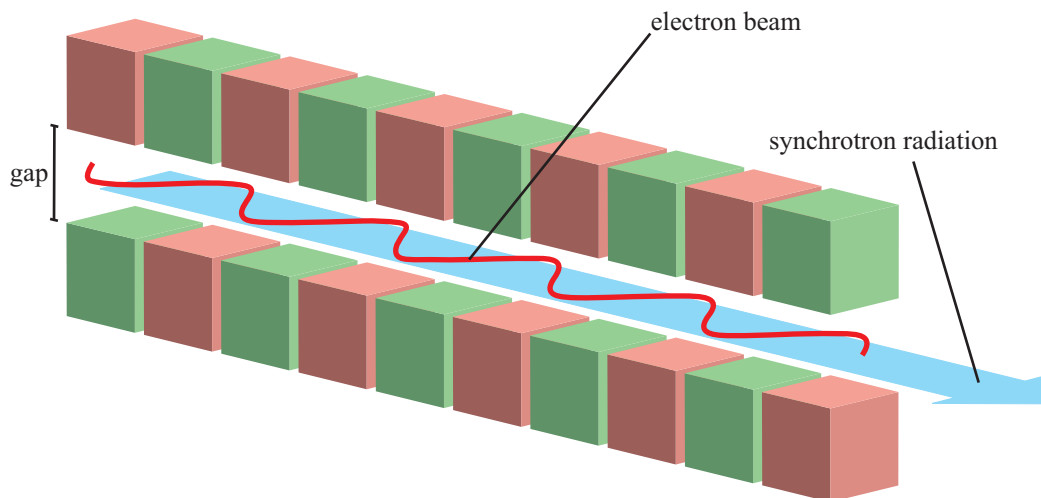


**Fig. 4.2:** Schematical drawing of a wiggler/undulator. The wiggler/undulator consists of an alternating magnet structure which forces the electron beam on an oscillating path while traveling through the wiggler. This causes the emission of synchrotron radiation.

the electron from its straight path. If the displacement is larger the insertion device is called a wiggler, and if it is small it is called an undulator. This leads to different characteristic emission spectra.

The spectrum emitted by wigglers is similar to the spectrum emitted by bending magnets. However, in contrast to bending magnets the bending radius within the magnet structure of the wiggler is not determined by the storage ring geometry and can be chosen to deliver an energy spectrum optimized for certain experimental techniques. The second advantage of wigglers compared to bending magnets is the higher intensity of the emitted radiation due to the iteration of several magnet structures in a row.

In case of undulators the small deviation of the charged particles from the straight path through the undulator leads to a coherent sum of the radiation emitted at each dipole of the undulator. This generates an emission spectrum consisting of a sharp intensity peak at a certain energy and its repetition at corresponding higher harmonics. The characteristic energy can be changed by changing the magnetic field. This is usually done by changing the opening gap of the undulator.

#### 4.2. Setup of an x-ray scattering beamline for (grazing incidence) x-ray diffraction and x-ray reflectivity

A typical beamline consists of three main parts. The first part is the front end with the radiation source (a bending magnet, wiggler or undulator). The second part is the beamline optics containing different devices for modification of the beam supplied by the frontend like monochromatization or focusing. The third part is the beamline endstation containing the experimental setup, most important is the diffractometer.

## The frontend

The frontend of a beamline contains the radiation source and high power slits capable to withstand the high intensity from the raw beam provided by the insertion device (or bending magnet). This is necessary to protect sensitive components in the beamline. At beamline W1 a wiggler with 16 periods (length 2 m) is used as insertion device. The P08 beamline is equipped with a undulator with 67 periods (length 2 m).

## The optics

The most important part of the optics for almost any synchrotron radiation beamline is the monochromator. The monochromator filters the photons of the desired photon energy (or wavelength) out of raw beam energy spectrum and dumps the rest. The most common monochromator design in the field of hard x-rays is an arrangement of two crystals called double-crystal monochromator (DCM). The first monochromator crystal is aligned to fulfill the (first order) Bragg condition for the desired energy. The second crystal is positioned so that the diffracted beam from the first crystal is hitting the second one fulfilling the same Bragg condition (see Fig. 4.3). Thus, only photons which fulfill the given Bragg condition can pass the monochromator. Typically, the monochromator crystals are made of silicon or germanium which can be grown at large size with very high purity and very small defect density. This is important since impurities in the crystal would cause diffuse scattering and therefore lower the intensity of the monochromatized beam.

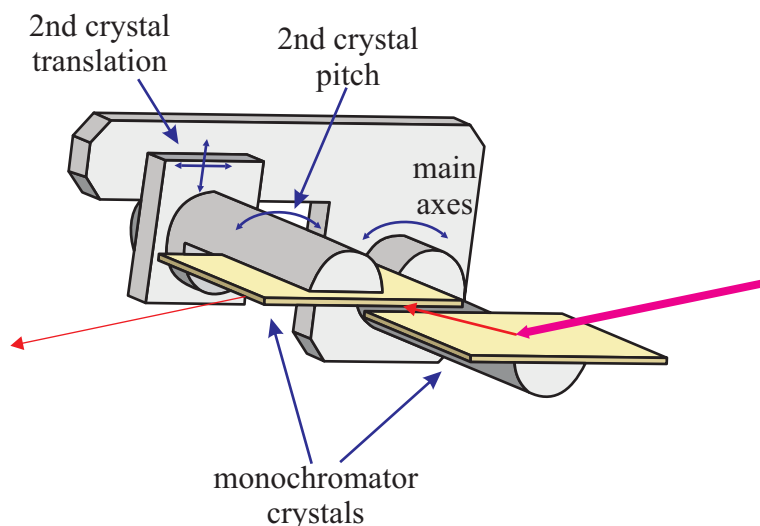


**Fig. 4.3:** Schematical drawing of a typical double-crystal monochromator. The white beam from the x-ray source is hitting the first DCM crystal. Here, the beam is diffracted at both the first and the second DCM crystal. To achieve a fixed vertical offset the second crystal can typically be shifted perpendicular and parallel to the first crystal. To compensate for small misalignments of both DCM crystals the second crystal typically has two additional rotations. One rotation in the same plane as the main axis (*pitch*) and the other one perpendicular to it (*roll*).

At beamline W1 a water cooled Si(111) DCM is used. At the P08 beamline an arrangement of

a DCM and a large-offset monochromator (LOM) is installed. The DCM is a liquid nitrogen cooled Si(111) monochromator with a fixed vertical offset of 22.5 mm. The LOM is also a DCM with fixed offset, but the vertical offset of 1250 mm is rather large compared to conventional DCMs. This is required to separate the beams of the P08 beamline and the adjacent beamline P09 located in the same straight section. Since the heat load of the monochromatic beam from the Si(111) DCM is much smaller compared to the raw beam no cooling is required for the LOM. The LOM is equipped with two crystal pairs. The first one is a Si(311) pair and the second one a Si(511) pair covering the energy range from 5.4 to 18.4 keV and from 8.4 to 29.4 keV, respectively. Since, the energy bandwidth of the Si(311) and Si(511) reflection is much smaller than the peak width of the Si(111) reflection the LOM also serves as a high resolution element in the beamline.

Another important component of a beamline optics is a device for higher harmonic suppression. So called higher harmonics are photons of an integer multiple of the fundamental energy. These photons can not be filtered by the monochromator since according to the Bragg law the diffraction angle for a first order Bragg reflection at an energy  $E$  is the same as for the  $n$ th order Bragg reflection at an energy  $E_{hh} = n \cdot E$ . In case of silicon or germanium (111) monochromators the second harmonic can usually be neglected since the (222) reflection is forbidden in the diamond structure<sup>1</sup>. Therefore, the third harmonic is usually the strongest harmonic which is observed.

A typical way to suppress these higher harmonics is the use of x-ray mirrors. Here, one takes advantage of the fact that the critical angle for total reflection depends on the energy of the incidence x-rays. As mentioned above, the critical angle can be approximated by  $\alpha_c = \sqrt{2\delta}$  where the material constant  $\delta$  generally decreases with increasing energy, leading to a lower critical angle  $\alpha_{c,hh}$  for the higher harmonics. By choosing a mirror angle between the critical angles  $\alpha_c$  and  $\alpha_{c,hh}$ , where the fundamental energy is totally reflected while the reflectivity for the higher harmonics is already decreasing the intensity of the higher harmonics is significantly reduced. Fig. 4.4 shows the reflectivity of an x-ray mirror of aluminum with a 100 nm gold coating for 10 and 30 keV. The reflectivity curves show clearly that for a fundamental photon energy of 10 keV and therefore a third harmonic of 30 keV a higher harmonic suppression of about  $10^{-2}$  can be achieved by choosing a mirror angle between the critical angles of total reflection for both photon energies.

At the W1 beamline a gold coated mirror is used for higher harmonic suppression. At the P08 beamline no mirrors are used. Instead the LOM serves as a higher harmonic suppressor. Here, one uses the fact that according to dynamical diffraction theory the Bragg angle of a symmetric reflection geometry slightly differs depending on photon energy and reflection index. Together with the very small divergence of the Petra III beam this leads to a virtually complete suppression of higher harmonics at P08 [56].

The third important component of the beamline optics are devices focusing or collimating the x-ray beam. Typical focusing devices are curved x-ray mirrors [58–60], compound refractive lenses (CRLs) [61] or in case of focusing to very small beam sizes also waveguides [62].

At W1 the same mirror which is used for the higher harmonic suppression is also used for focusing. Here, a spot size of  $1.6 \times 4 \text{ mm}^2$  at the sample can be achieved. At P08 two CRL

---

<sup>1</sup>Due to an asymmetry in the electron density distribution within the silicon and germanium unit cell the (222) reflection vanishes not completely but the integrated intensity of the reflection is significantly reduced compared to the other non-forbidden reflections.

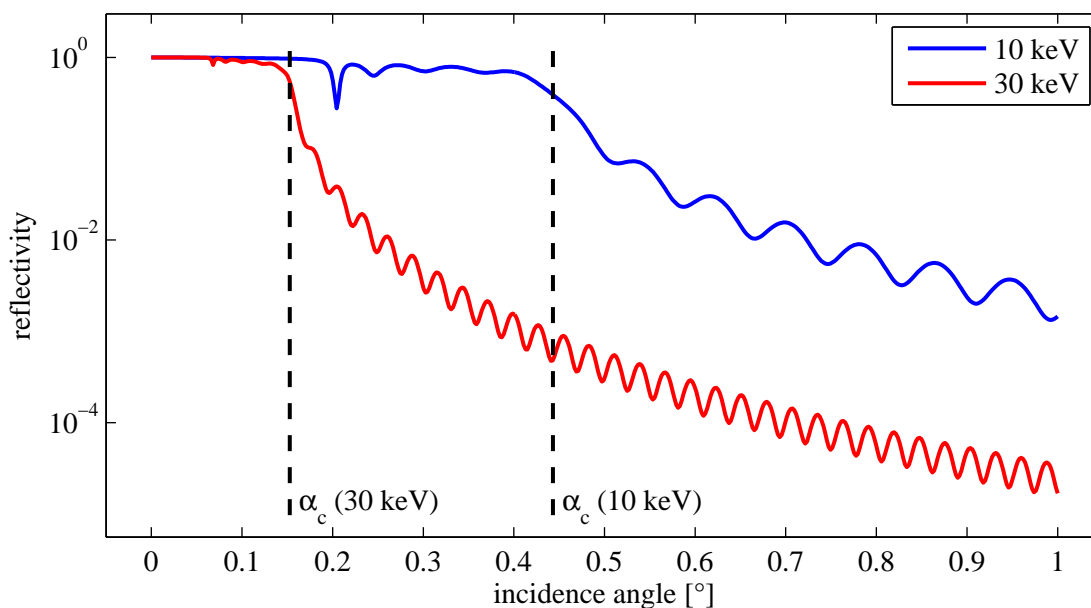


**Fig. 4.4:** Calculated reflectivity of a x-ray mirror coated with 100 nm gold for 10 and 30 keV. The critical angles for total reflection are indicated by dashed lines.

changers are installed equipped with different sets of beryllium CRLs which can be moved into the beam to achieve the desired focusing or collimation of the beam. The first CRL changer is positioned approximately in the center between the source, i.e. the undulator, and the sample position for collimation or moderate focusing. The second CRL changer is installed at a distance of 1.5 m to the sample position allowing microfocusing. The typical spot size at the sample position in collimation mode is  $700 \times 400 \mu\text{m}^2$  and  $30 \times 2 \mu\text{m}^2$  using the microfocusing mode.

### The endstation

At the beamline endstation the actual experimental setup is located. The main part of an endstation for x-ray scattering experiments are: a diffractometer for sample and detector positioning, one or more slit systems to define the beam shape and to cut off unwanted scattering within the beamline, a primary beam intensity monitor and a beam attenuator.

When performing x-ray scattering experiments the incidence beam on the sample, and the detector have to be positioned according to the desired scattering condition. Since tilting the incidence x-ray beam is very complicated in most cases the sample is moved instead. Only in cases where sample movement is not possible or hard to achieve, e.g. liquid samples, the x-ray beam is tilted using special x-ray mirror or monochromator setups [63]. For x-ray reflectivity and specular x-ray diffraction the calculation of scattering angles for sample and detector is rather simple. If the sample is tilted in one plane, typically perpendicular to the beam polarization, by an angle  $\theta$ , the detector has to be rotated by  $2\theta$  in the same plane to fulfill the scattering condition. Therefore, this geometry is also known as  $\theta - 2\theta$  setup. For other sample geometries like CTR scans in a grazing incidence setup calculations to convert angular positions into a position in reciprocal space are available in the literature for

a broad range of different diffractometer types. For beamlines dedicated to such techniques these calculations are usually implemented into the beamline control software. Depending on the requirements of the experimental techniques, different diffractometer types are used, e.g. z-axis diffractometers are mainly used at surface diffraction beamlines.

The W1 beamline endstation is equipped with a six-circle z-axis heavy load diffractometer (cf. Fig 4.5) designed and build by the Risø National Laboratory (Denmark). Detailed information on possible scattering geometries can be found in the literature e.g. [64]. This diffractometer type is optimized for surface diffraction in a grazing incidence mode but can also be used in so called four-circle mode e.g. for specular x-ray diffraction or reflectivity.

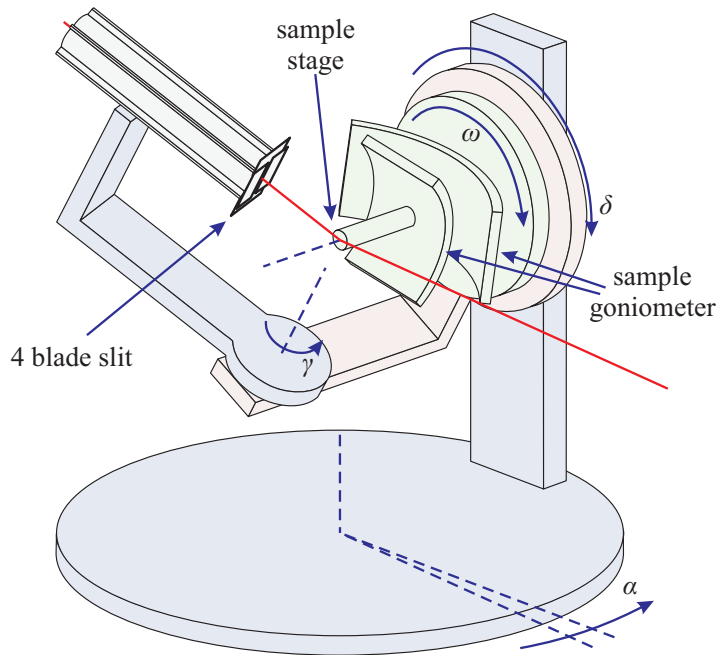


**Fig. 4.5:** Sketch of the z-axis diffractometer at W1. The rotation  $\alpha$  is rotating the whole diffractometer with respect to the incoming beam. The rotations  $\delta$  and  $\gamma$  are used for the positioning of the detector, while  $\omega$  is used for sample positioning. Using the z-axis mode, where the sample is vertically mounted,  $\alpha$  is the fixed angle of incidence,  $\omega$  the sample azimuth,  $\delta$  the inplane detector angle and  $\gamma$  the out of plane detector angle. In the four-circle mode, where the sample is horizontally mounted,  $\alpha$  and  $\gamma$  are fixed to zero,  $\omega$  is the variable angle of incidence and  $\delta$  the out of plane detector angle.

At the P08 beamline endstation a Kohzu Multi-Circle Diffractometer NZD-3 is installed. This is a 4S+2D type diffractometer, i.e. it has four degrees of freedom for sample positioning and two for detector positioning. It was specially designed to meet the P08 requirements of a small beam height (1 m) and high precision. Compared to the six-circle z-axis diffractometer at W1 this diffractometer offers several additional scattering modes [65]. However, in the experiments shown in this work only the grazing incidence geometry and the four-circle mode which are also available at the W1 instrument were used.

X-ray detectors are necessary to detect the x-rays scattered at the sample. Different types of x-ray detectors are available like scintillation detectors, photo diodes, pixel detectors or ccd cameras. Detectors are also available in different dimensions. The most simple ones are zero dimensional point detectors which are usually cheaper, faster and have, together with certain slit systems, a better spacial resolution compared to higher dimensional detectors. Also one dimensional array detectors and two dimensional area detectors are available. The advantage of these detectors is that the data from a quite large range of possible detector positions can be recorded at the same time e.g. for reciprocal space mappings or background subtraction. However, if a small part of a one or two dimensional detector is illuminated by very intense x-rays, e.g. from a Bragg reflection, the primary beam has to be attenuated by

a certain level to avoid a damaging of the detector. In this case the intensity detected on other detector regions is also attenuated and gets very noisy or is not detectable any more within a reasonable time period. To measure these regions anyway beam stops have to be used blocking the high intensity beam which would hit the detector without blocking the low intensity parts. While this problem is negligible in most cases for array detectors it becomes a serious problem for two dimensional detectors.

At both beamlines W1 and P08 Cyberstar NaI scintillation point detectors and Mythen array detectors [66] are available. Due to its higher dynamic range and the capability of creating reciprocal space maps within a much smaller time compared to the point detector the Mythen detector was used in most experiments shown in this work.

As mentioned above detectors can be damaged by high intensity x-ray beams. It is also important that the intensity measured by the detector is only proportional to the real intensity up to a certain intensity level. For the Cyberstar and Mythen detectors this level is  $10^5$  photon cts (counts per second) and  $10^6$  photon cts per pixel, respectively. Thus, the primary beam with a flux of  $\approx 10^{11}$  cts at W1 is far above this value. However, the high flux is necessary when measuring regions in reciprocal space with low scattering probability. To overcome this problem beam attenuators, often called absorbers, are used. The principle of beam attenuators is an absorbing object which is moved into the primary beam. Typical absorber setups have the possibility to attenuate the beam by several different absorption factors. This guaranties that the beam is not attenuated by an inadequate high factor.

Absorber setups where several foils can independently be moved into the beam are installed at both W1 and P08. By combining different foils attenuation over the whole range from completely blocking the primary beam to no attenuation can be achieved. The beamline control software can be used to automatically choose a reasonable attenuation value within the measurements. The data is corrected afterwards by the attenuation factor used at each data point.

Since the intensity of the primary beam might change during one measurement it is important to monitor this intensity to normalize the measured data. Detuning of optical components (e.g. the monochromator), decay of the storage ring current, or partial beam loss in the storage ring are possible reasons for changes in the primary beam intensity. A typical technique to obtain this intensity is to measure the scattered intensity from a target with very low absorption like gas targets or foils of low electron density materials, e.g. carbon. In case of gas targets it is also possible to measure the charge induced by ionizing gas molecules using an ionization chamber. At beamline W1 the scattering from residual gas in the beampipe and at beamline P08 the intensity scattered from thin carbon foil is detected by NaI scintillation point detectors. At P08 the primary beam can also be monitored by a fluorescence crystal tilted by  $45^\circ$  with respect to the beam which is recorded by an optical ccd-camera.

To shape the beam profile and cut off unwanted background scattering slits can be put into the beam. A typical design is a four-blade slit system. These systems consist two horizontal and two vertical blades, which can be used to define a horizontal and a vertical slit.

At beamline W1 a four-blade slit system is installed before the sample position to shape the beam and a second one is installed at the entrance of the detector flight tube. In front of the Mythen detector an additional slit of fixed size is installed. Together with the slit at the flight tube entrance this slit defines the acceptance angle of the detector. At beamline P08 a similar slit setup is installed but with two four-blade slits before the sample position. The

second slit is installed to cut of scattering from the first one.

### **The beamline control software**

Due to the high radiation level of the x-rays the experiments have to be set up in specially shielded areas usually called hutches. These hutches can only be entered when the x-ray beam is "switched off", i.e. the beam is blocked by a beam shutter. Basically, a beam shutter is an object which can be moved into the beam and is able to completely block the x-ray beam without getting damaged. Interlock systems are installed to ensure that nobody can enter a hutch when the beam shutter is not blocking the beam.

Therefore, almost all experimental equipment can be operated remotely. All equipment is controlled from a computer via the beamline control software. This is usually a special software designed to communicate with the beamline equipment like detectors, motors, etc. and which is able to perform the measurements and display the results as graphs. A typical measurement is detecting the scattered intensity for different positions of one or more motors. These measurements are called scans. Beamline control software, especially at diffraction beamlines, often also includes algorithms for converting between reciprocal and angular space.

At both beamlines W1 and P08 the beamline control software *online* <sup>[67]</sup> is used which was developed at *Deutsches Elektronen-Synchrotron*.

### 4.3. Scattering geometries

An incident x-ray beam has two degrees of freedom for positioning with respect to the sample surface, assuming that the incident beam is always hitting the sample surface at the center of the sample. The first degree of freedom is the angle between incident beam and the sample surface ( $\alpha_i$ ). The second one is the rotation of the sample ( $\phi$ ) around the surface normal with respect to the incident beam. The detector has the same two degrees of freedom for positioning; the rotation around the surface normal ( $\gamma$ ) and the exit angle between sample surface and detector ( $\delta$ ). Thus in total there are four degrees of freedom to position the incident beam and the detector with respect to the sample according to a certain diffraction condition as illustrated in Fig. 4.6. However, the diffraction condition is defined by a three dimensional scattering vector. Thus, there is no unique solution for the positioning of incident beam and detector to achieve a certain diffraction condition. Therefore, different scattering geometries have been developed for different purposes. For each of this scattering geometries certain angular restrictions are defined, e.g. the angle between incidence beam and sample surface should be fixed. Using these restrictions a unique conversion from angular space to reciprocal space and vice versa is possible. In this work two different scattering geometries, a setup for specular and a grazing incidence scattering, are used.

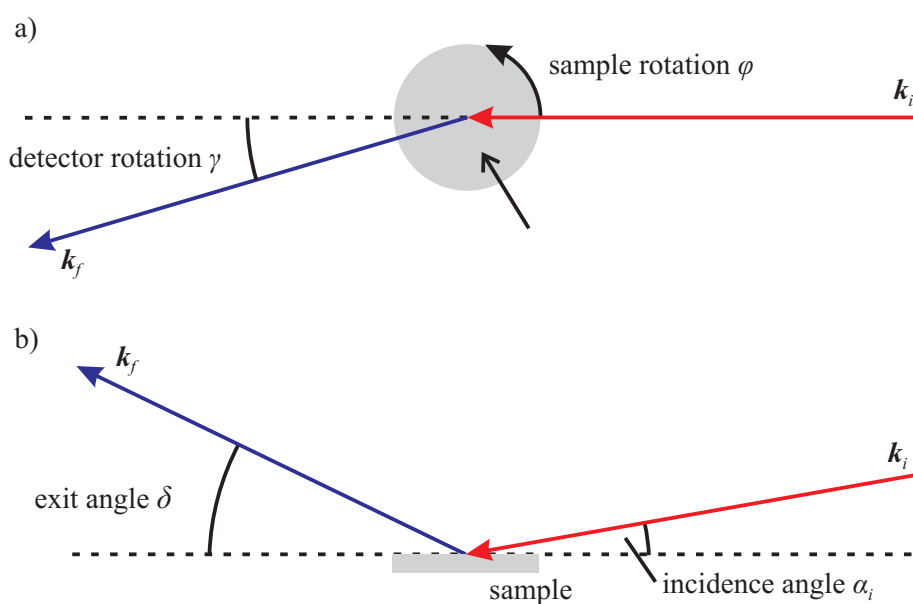


**Fig. 4.6:** Sketch illustrating the four degrees of freedom for the position of the incidence angle and the exiting angle.

Different types of diffractometers have been developed according to the requirements of different scattering geometries. However, it is important to note that in real diffractometers the four angles ( $\alpha_i$ ,  $\phi$ ,  $\gamma$ , and  $\delta$ ) are usually not fully independent. Thus, these dependencies have to be considered when converting between reciprocal and angular space.

In the specular setup the lateral components of the scattering vector are zero. This can only be achieved if the angle between the incidence beam and the sample surface is the same as the angle between the detector and the sample surface. Furthermore, the wave vectors resulting from the incident and the exiting beam have to be in the same plane perpendicular to the

surface, i.e.  $\gamma = 0$ . When using the incident beam as a reference frame for this geometry the detector has to be tilted by  $2\theta$  if the sample is tilted by  $\alpha_i = \theta$ . Therefore, this scattering geometry is often referred to as  $\theta - 2\theta$  setup.

This sample geometry has two important advantages. First, the angular calculations for certain scattering conditions are rather simple ( $\alpha_i = \delta$ ). Since only two angles are involved moving in the same plane, this geometry is already supported by the most basic types of diffractometers. The second advantage is that since the lateral components of the scattering vector are zero ( $H = K = 0$ ) all lateral effects can be neglected, e.g. lateral misfit or the absorption site of a film. Therefore, the analysis of the diffraction pattern simplifies.

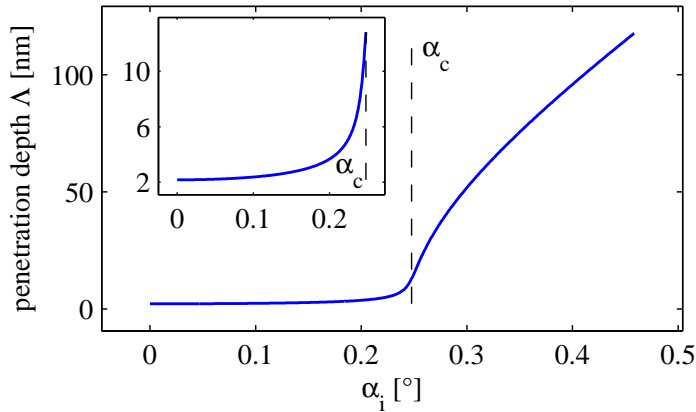


**Fig. 4.7:** Penetration depth of an x-ray beam of 10.5 keV upon a magnetite surface as a function of the angle of incidence  $\alpha_i$ .

To use a grazing incidence setup a fixed incidence angle  $\alpha_i$  is necessary. Typically, it is close to the critical angle for total reflection  $\alpha_c$  to increase the surface sensitivity of the measurement. The penetration depth of the x-rays strongly depends on the incidence angle (cf. Fig. 4.7). Choosing certain angles of incidence it is possible to change the surface sensitivity of a measurement. For  $\alpha_i < \alpha_c$  an evanescent wave is formed, which is traveling along the sample surface. In this case the scattering originates exclusively from the near surface region. For  $\alpha_i > \alpha_c$  the penetration depth rapidly increases with increasing angle of incidence. Therefore, grazing incidence x-ray diffraction (GIXRD) has become a standard tool to study the structure of surfaces and ultrathin films [23,24].

Since the angle of incidence is fixed in the grazing incidence setup only three degrees of freedom remain to fulfill a scattering condition.

## 4.4. Data correction

To analyze the experimental diffraction data obtained by CTR scans one has to take into account several correction factors for the measured intensity ( $I_{\text{mea}}$ ). These corrections will be explained briefly in the following. A more detailed derivation by E. Vlieg can be found in the literature [68]. The correction factors are calculated for specular diffraction with horizontal sample surface and grazing incidence diffraction in the z-axis mode with a vertical sample surface alignment. For the data correction we will neglect all effects which give a constant correction for the whole scan, e.g. intensity of the primary beam. In the data analysis these factors are collected in a single constant resulting in an arbitrary scaling of the intensity.

### Illumination correction

For small incidence angles usually a part of the beam is not hitting the sample and, therefore, not contributing to the diffracted intensity. The illumination correction takes into account the intensity loss due to this.

Illumination correction is not taken into account since it only applies for small angles. Thus, in case of specular diffraction it is not relevant. In case of grazing incidence diffraction the angle of incidence is small but fixed. Thus, the illumination correction is constant.

### Polarization factor

The polarization of the x-ray beam reduces the scattered intensity by a factor of  $\cos^2 \alpha_{\text{pol}}$  where  $\alpha_{\text{pol}}$  is the angle between the direction of observation and the vector indicating the direction of polarization.

Taking the setup of the z-axis diffractometer (as shown in Fig 4.5) into account we obtain for the polarization factor

$$P = p_h P_{\text{hor}} + (1 - p_h) P_{\text{ver}} \quad (4.2)$$

$$= p_h (1 - (\sin \alpha \cos \delta \cos \gamma + \cos \alpha \sin \gamma)^2) + (1 - p_h) (1 - \sin^2 \delta \cos^2 \gamma) \quad (4.3)$$

where the  $p_h$  is the horizontal fraction of the polarization.  $P_{\text{hor}}$  and  $P_{\text{ver}}$  are the polarization factors for the horizontal and vertical fraction, respectively.

The experiments shown in this work were performed at wiggler/undulator beamlines at synchrotron radiation sources. Here, the polarization is typically 99% (or better) vertically aligned. Thus, we assume  $p_h \approx 1$ .

For the grazing incidence case we obtain the factor

$$P_g \approx 1 - (\sin \alpha \cos \delta \cos \gamma + \cos \alpha \sin \gamma)^2 \quad (4.4)$$

while for specular diffraction no polarization effects ( $P_s = 1$ ) have to be taken into account due to the horizontal setup.

### Lorentz factor

When measuring the intensity of the scattered beam one integrates over the intensity in the area of the detector acceptance. To compensate changes in the integration volume when performing the conversion from angular to reciprocal space the Lorentz factor is introduced.

For the grazing incidence setup the Lorentz factor is given by

$$L_g = \frac{1}{\sin \gamma} \quad (4.5)$$

while we obtain

$$L_s = \frac{1}{\sin \omega} \quad (4.6)$$

for specular diffraction.

### Active area

The active area describes the sample area which is illuminated by the x-ray beam and is visible to the detector (see fig. 4.8). This is determined by the setting of the slits and the detector position. Since the slits are not moved during the measurement the slit contribution is constant and therefore neglected.

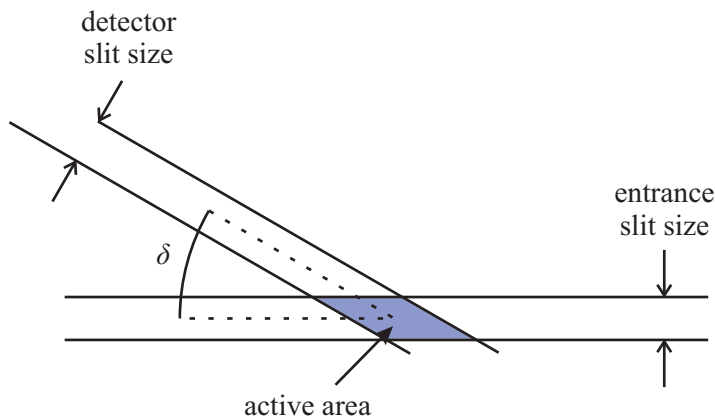


**Fig. 4.8:** Sketch illustrating the active sample area for the grazing incidence geometry. The active area is defined by the entrance slit size, i.e. the primary beam size, the detector slit size and the angle between sample and detector.

In the grazing incidence case the active area is given by

$$A_g = \frac{1}{\sin \delta} \quad (4.7)$$

and by

$$A_s = \frac{1}{\sin \omega} \quad (4.8)$$

in the specular diffraction case.

### Total correction

The correction factor  $\eta$  is now given by taking all corrections mentioned above into account

$$\eta = \frac{1}{P L A} . \quad (4.9)$$

The corrected intensity ( $I_{\text{cor}}$ ) is now given by

$$I_{\text{cor}} = \eta I_{\text{mea}} \quad (4.10)$$

$$= \frac{1}{P L A} I_{\text{mea}} \quad (4.11)$$

Thus the corrected intensity for grazing incidence setup is given by

$$I_{\text{cor,g}} = \frac{1}{P_g L_g A_g} I_{\text{mea}} \quad (4.12)$$

$$= \frac{\sin \gamma \sin \delta}{1 - (\sin \alpha \cos \delta \cos \gamma + \cos \alpha \sin \gamma)^2} I_{\text{mea}} \quad (4.13)$$

and the corrected intensity for the specular setup is given by

$$I_{\text{cor,s}} = \frac{1}{P_s L_s A_s} I_{\text{mea}} \quad (4.14)$$

$$= \sin^2 \omega I_{\text{mea}} . \quad (4.15)$$

## 4.5. Data analysis of x-ray diffraction data

To analyze CTR scans the data fitting program RodsNPlots was used. This program was developed by A. Greuling [69] and extended in several other works [70, 71]. For calculating the diffracted intensity along CTRs it uses the formula derived in Sec. 2.3 (Eq. 2.39).

The model assumed in RodsNPlots consists of a variable number of lateral coexisting **columns**. The scattering from all columns is summed incoherently, i.e. the scattered intensity is summed. Each column consists of a variable number of **layers**. The bottom layer is always assumed to be the substrate. Each layer has the following parameters:

- **material:** RodsNPlots contains many predefined unit cell definitions which are selected by the material parameter. By selecting a material one defines the structure factor used for the specific layer and the vertical lattice vector  $\mathbf{c}$ . The material can not be changed by the fitting algorithms.
- **layer:** Layer gives the number of atomic layers within the film. The number of layers has to be an integer number. Therefore, it is not practical to fit this parameter.
- **theta:** The occupation factor  $\Theta$  describes the coverage as well as holes or other impurities within the film which do not contribute to the diffracted intensity. It is also used for weighting the contribution from different columns.
- **intern:** Intern is a scaling factor for the vertical component of the vertical lattice vector  $\mathbf{c}$  as well as the vertical component of the unit cell atom positions. Thus, from its value the vertical layer distance can be calculated.
- **grenz:** Grenz is a scaling factor for the vertical component of the interface vector  $\mathbf{g}$ .
- **place:** Place defines the adsorption site of the film. Each integer number corresponds to a predefined interface vector  $\mathbf{g}$ . Place can not be changed by the fitting algorithm.
- **rms top/bot:** The top ( $\sigma_+$ ) and bottom ( $\sigma_-$ ) rms roughness is given by rms top/bot.
- **DW:** The Debye-Waller factor takes into account thermal vibrations as well as impurities within the crystal.

Other important model parameters not connected to individual films are:

- **A0:** The parameter A0 serves as a scaling factor of the scattered amplitude. It includes all parameters which are constant during a single measurement, e.g. the primary beam amplitude.
- **dampening:** The dampening factor  $\epsilon$  takes into account absorption within deeper layers of the substrate. This parameter cannot be fitted.
- **ground:** The ground parameter adds a constant background to the calculated intensity.

To find a set of variables which results in a calculated intensity reproducing the measured data optimization algorithms are used.

Such algorithms are widely used in different fields of science. The goal of an optimization algorithm is to find the dataset  $\mathbf{x}$  for which a function  $f(\mathbf{x})$  has a minimum value, especially, if no analytical solution to the problem is possible. In case of data fitting a function has to be defined describing the difference between the calculated and the experimental intensity.

In case of RodsNPlots this function is given by

$$E(\mathbf{x}) = \frac{1}{N} \sum_{j=1}^N \left| \log I_{exp}^j - \log I_{cal}^j(\mathbf{x}) \right| \quad (4.16)$$

where  $\mathbf{x}$  is a vector representing the different model parameters,  $N$  is the number of data points and  $I_{exp}^j$  and  $I_{cal}^j(\mathbf{x})$  are the measured and calculated intensities at data point  $j$ , respectively.

For data fitting four different optimization algorithms are used:

- a *hillclimb* algorithm based on nested intervals
- a Nelder-Mead simplex algorithm
- a Metropolis algorithm
- a differential evolution algorithm

The *hillclimb* and the simplex algorithm are deterministic approaches to the optimization problem while the Metropolis and the differential evolution algorithms use also random modifications. Therefore, the Metropolis and the differential evolution algorithms are much better suited for finding a global minimum while the other two can easily get stuck in local minima. Detailed descriptions of the four algorithms and their performance can be found in the work of A. Greuling <sup>[69]</sup> and only a brief discription will be given in the following.

### The hillclimb algorithm

The *hillclimb* algorithm uses nested intervals to find the minimum of a given function  $f(\mathbf{x})$ . Starting with the first element of the vector  $\mathbf{x}$  each element is varied using nested intervals until a minimum for  $f(\mathbf{x})$  is reached. Then, the next element of  $\mathbf{x}$  is varied accordingly. After the last element of  $\mathbf{x}$  has been varied the whole process is repeated for several iterations.

### The Nelder-Mead simplex algorithm

For a vector  $\mathbf{x}$  with  $N$  elements a simplex containing  $N + 1$  points in the  $N$  dimensional parameter space is created. In RodsNPlots the first point of the simplex is given by the user defined start parameters while all other points are initially randomly generated.

To minimize the function  $f(\mathbf{x})$  the Nelder-Mead algorithm replaces the point of the simplex for which  $f(\mathbf{x})$  is maximized using certain rules for creating the new point in parameter space, e.g. reflection, contraction, and expansion of the simplex. This procedure is continued over several iterations.

### The Metropolis algorithm

The Metropolis algorithm is a Monte Carlo based technique. Within each integration step one parameter of the vector  $\mathbf{x}$  is modified randomly. If this modification leads to a lower value for  $f(\mathbf{x})$  the change is accepted. However if, the modification leads to a larger value for

$f(\mathbf{x})$  the change is only accepted at a certain probability given by

$$p = e^{- (f(\mathbf{x}_{old}) - f(\mathbf{x}_{new})) / T} \quad (4.17)$$

where the parameter  $T$  can be used to adjust the probability of accepting changes leading to higher values of  $f(\mathbf{x})$ . This procedure is repeated for several iterations.

RodsNPlots offers the possibility to gradually decrease the parameter  $T$  with each iteration. Thus, the probability of accepting changes leading to higher  $f(\mathbf{x})$  is decreasing. It is also possible to change the maximum step width for each iteration so that in the beginning, when the distance to the minimum is relative large, huge changes are applied while in the end when the distance to the minimum is relative low, only smaller changes are applied. Within the Metropolis algorithm also changes leading to a higher  $f(\mathbf{x})$  are accepted. Therefore, this algorithm can escape local minima in contrast to the previously presented algorithms.

### The differential evolution algorithm

The differential evolution is a genetic algorithm which tries to model the natural evolution to minimize a function  $f(\mathbf{x})$ . First, a set of different vectors  $\mathbf{x}$  is generated. This set of vectors is called *population*. With each iteration step called *generation* the population is modified according to specific genetic operations. The genetic operations used in RodsNPlots are recombination, mutation and selection. Recombination generates a new vector by combining two existing vectors, while the mutation modifies existing vectors by random changes. The selection ensures that only the best vectors, i.e. those where  $f(\mathbf{x})$  has low values, are continued towards the next generation. Since the mutation as well as the recombination include random operations this algorithm is also able to escape local minima. In RodsNPlots the algorithm is implemented as described by Wormington et al. [72].

Concerning the analysis of x-ray diffraction data the differential evolution algorithm has proven to be the most effective of the algorithms presented here during daily work.

### Limitations of the theoretical model

Although, the theoretical model and the resulting formula developed in sec. 2.3 (Eq. 2.39) can describe the diffracted intensity from epitaxial thin films with a very high accuracy one has to consider some restrictions.

First, the model does not include any lateral misfit. In case of the films studied in this work this fact is not a problem since the lateral misfit is very small compared to the lateral width of Bragg peaks.

Second, only integer values for the number of atomic layers can be used within the theoretical model. The reason is that the N-slit function becomes a non-continuous function if  $N$  is not an integer number and becomes infinite when  $\exp(ix)$  becomes zero, i.e. when  $x$  is an integer number, as shown in Fig. 4.9 a).

In this context a non-integer number of atomic layers means that the *average* number of atomic layers is not an integer number. This means one or more layers are not fully occupied, e.g. in case of a rough surface. This can be modeled by assuming an integer number of layers with an occupation factor  $\Theta = 1$  and on top a single layer with  $\Theta < 1$ . The interface vector

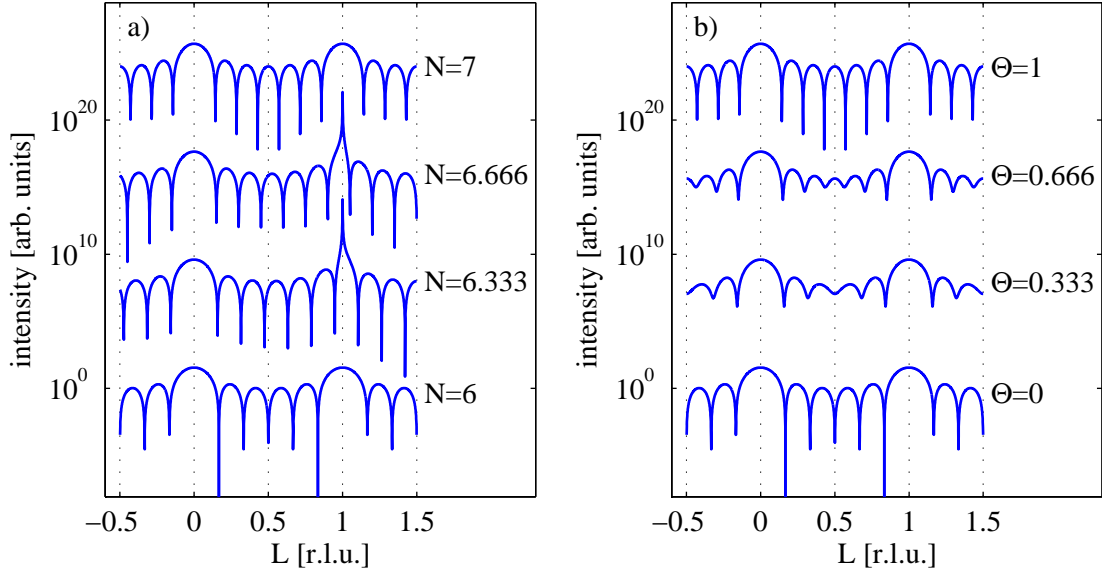


**Fig. 4.9:** a) The intensity of an N-slit function for different  $N$  ranging from 6 to 7. For non-integer  $N$  the intensity becomes infinity at  $L = 1$ . b) The intensity of a stack of two films. The lower layer consists of 6 atomic layers with  $\Theta = 1$  while the top layer consists of a single atomic layer with  $\Theta$  ranging from 0 to 1.

$\mathbf{g}$  has to be the same as the lattice vector  $\mathbf{c}$  of the layer below. Fig. 4.9b) shows the intensity distribution along  $L$  for different values of  $\Theta$ . The same considerations shown here for the N-slit function are also true for the modified N-slit function taking roughness into account.

Third, the roughness model causes a damping of the diffracted intensity between two Bragg peaks. However, it does not take the structure factor into account. Thus, if a Bragg peak is forbidden according to its structure factor the roughness results in a damping of the intensity around this forbidden Bragg peak but not at the position of this forbidden peak. This effect is illustrated in Fig 4.10 where forbidden Bragg peaks are present at the half order positions. At the position of the forbidden peak a small peak is visible which results from the missing dampening at that point. With increasing roughness this becomes even more pronounced. Thus, analyzing regions around forbidden Bragg peaks using this roughness model will lead to unreasonable results. Similar to the case of non-integer numbers of atomic layers a model introducing several single layers with different  $\Theta < 1$  could be used to describe a roughness which is also valid around forbidden Bragg reflections.

This problem is another reason why the unit cell implemented in the program should be as small as possible. When choosing a larger unit cell the number of forbidden Bragg peaks increases at which the intensity can not be accurately described by the theoretical model.

Keeping these restrictions in mind, however, the theoretical model is a powerful tool for analyzing the diffracted intensity from epitaxial thin film layer systems.

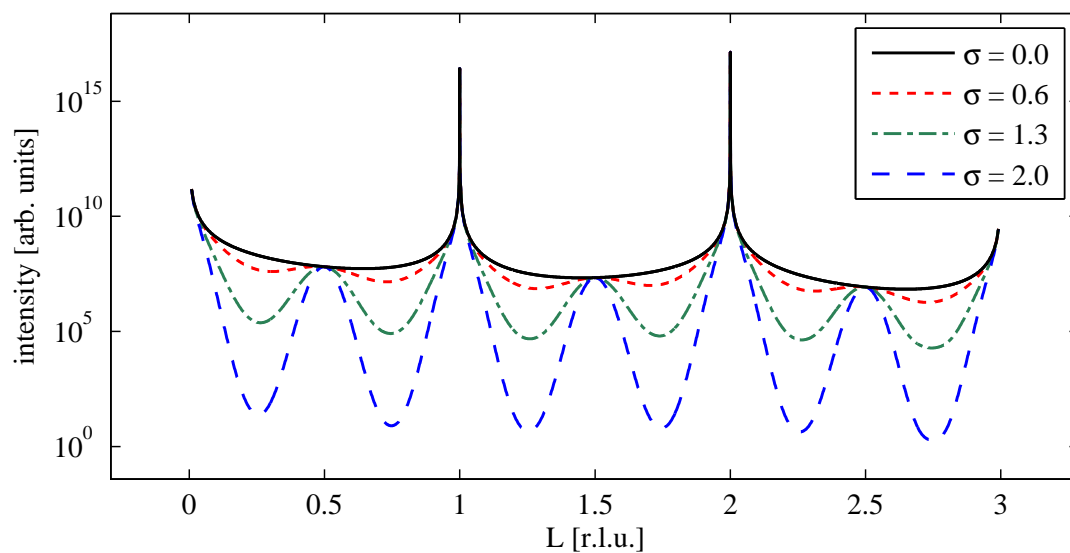


**Fig. 4.10:** Calculated intensity using different roughness values. For reasons of simplicity the calculation is done for a  $\text{Fe}_3\text{O}_4$  substrate but the same behavior occurs for thin films. With increasing roughness the intensity between the Bragg peaks is dampened. However, the intensity at the Bragg peaks forbidden by the structure factor (half order positions) remains constant independent of the roughness.



## 5. Experimental results on the structure of iron oxide thin films

In the following chapters the experimental results on the structure of iron oxide thin films are presented. In the first two chapters (Chap. 6 and 7) the influence of the deposition conditions on the film structure are discussed, while the subsequent chapters (Chap. 8 and 9) deal with the influence of post-deposition annealing (PDA) on the structure. In Chap. 10 the design of a high vacuum heating chamber for *in-situ* x-ray scattering experiments is presented, which was used for the *in-situ* experiments presented in Chap. 9.

The iron oxide thin films studied in the following chapters were all prepared by reactive molecular beam epitaxy (MBE) at low oxygen atmosphere. Here, commercially available MgO(001) single crystals of  $10 \times 10 \times 0.5 \text{ mm}^3$  from MaTeck GmbH were used as substrates. The sample preparation was performed in a multichamber ultrahigh vacuum (UHV) system consisting of a deposition chamber with a base pressure of  $10^{-8}$  mbar and an analysis chamber with a base pressure of  $10^{-10}$  mbar. The preparation chamber is equipped with an electron beam heating system, a high precision leak valve to supply low gas doses, and two evaporators for iron and silicon deposition. Both evaporators use an electron beam heating. Electrons emitted from a tungsten filament are accelerated by high voltage towards the material source. In case of the iron evaporator high voltage is applied directly to the iron rod. This is possible since at UHV conditions iron starts to sublime before it starts to melt. For the silicon evaporator a crucible is necessary to store the silicon.

The analysis chamber is equipped with a back-view LEED system and an XPS system consisting of a SPECS XR-50 x-ray tube with an Al anode and a Phoibos HSA 150 hemispherical analyzer. The dominant photon energy in the emission spectrum of such aluminum tubes is the Al  $K_{\alpha}$  line with an energy of 1486.6 eV. The energy resolution of the analyzer is 1 eV.

All samples have been prepared according to the procedure described in the following. Prior to the thin film deposition the samples have been cleaned by heating in UHV and low oxygen partial pressure. This leads to films without any carbon contaminations as checked by XPS and a high crystal quality with flat surfaces. Prior to the deposition the samples are first annealed to the desired substrate temperatures and the required amount of oxygen is introduced using the leak valve. Afterwards the evaporators are adjusted to deliver a certain deposition rate as measured by an oscillation quartz balance. As soon as all parameters are adjusted the evaporator shutter is opened to start the deposition. To prevent the reduction of the oxide films due to high substrate temperatures the oxygen level is kept constant after deposition until the sample has cooled down. Afterwards *in-situ* LEED and XPS measurements are performed.



---

Original publication: Journal of Physics D: Applied Physics **45**, 395302 (2012).  
available at <http://dx.doi.org/10.1088/0022-3727/45/39/395302>

## **X-ray diffraction study on size effects in epitaxial magnetite thin films on MgO(001)**

F. Bertram, C. Deiter, O. Hoefert, M. Suendorf, T. Schemme, F. Timmer, B. Zimmermann, and J. Wollschläger

### **Abstract**

Epitaxial ultrathin iron oxide films of different thicknesses were grown by reactive molecular beam epitaxy in  $10^{-6}$  mbar oxygen atmosphere on MgO(0 0 1) single crystal substrates at room temperature. Afterwards, the films were studied by x-ray diffraction, x-ray reflectivity and x-ray photoelectron spectroscopy to provide information regarding film structure as well as chemical composition of the films. Except for a very thin interface layer of subnanometer thickness, the iron oxide films have magnetite stoichiometry and structure and Mg does not diffuse from the substrate into the iron oxide film. The interface layer has wuestite structure as determined by kinematic diffraction analysis. The magnetite films exhibit very homogeneous thickness while the vertical lattice constant decreases gradually towards its bulk value.



---

Original publication: Journal of Applied Physics **113**, 184103 (2013).  
available at <http://dx.doi.org/10.1063/1.4803894>

# Reordering between tetrahedral and octahedral sites in ultrathin magnetite films grown on MgO(001)

F. Bertram, C. Deiter, T. Schemme, S. Jentsch, and J. Wollschläger

## Abstract

Magnetite ultrathin films were grown using different deposition rates and substrate temperatures. The structure of these films was studied using (grazing incidence) x-ray diffraction, while their surface structure was characterized by low energy electron diffraction. In addition to that we performed x-ray photoelectron spectroscopy and magneto optic Kerr effect measurements to probe the stoichiometry of the films as well as their magnetic properties. The diffraction peaks of the inverse spinel structure, which originate exclusively from Fe ions on tetrahedral sites are strongly affected by the preparation conditions, while the octahedral sites remain almost unchanged. With both decreasing deposition rate as well as decreasing substrate temperature the integrated intensity of the diffraction peaks originating exclusively from Fe on tetrahedral sites is decreasing. We propose that the ions usually occupying tetrahedral sites in magnetite are relocated to octahedral vacancies. Ferrimagnetic behaviour is only observed for well ordered magnetite films.



# 8. Post-deposition annealing induced reordering of tetrahedral sites

## 8.1. Introduction

In the previous chapter [98] the influence of deposition conditions on the structure of thin magnetite ( $\text{Fe}_3\text{O}_4$ ) films grown on  $\text{MgO}(001)$  was studied. The ordering of the tetrahedral sites of ultra thin magnetite films was found to be strongly depending on the deposition parameters. For low deposition rates as well as low temperatures a weak ordering on tetrahedral sites was observed while the ordering on octahedral sites remains almost unaffected. In this chapter the effect of post-deposition annealing (PDA) at low oxygen atmospheres on the structure of films with such weak ordering on the tetrahedral sites will be discussed. In the literature several reports can be found that PDA at oxygen atmospheres can improve the structure of iron oxide thin films, e.g. reduce the density of antiphase boundaries (ABP) [53].

## 8.2. Experimental setup

A magnetite thin film was grown by reactive MBE under molecular oxygen atmosphere of  $5 \times 10^{-6}$  mbar at room temperature in a multi chamber UHV system as previously described (cf. Chap. 5). After deposition the sample was removed from the UHV system and split in four equally sized parts. Each part was successively introduced into the UHV system again for PDA. The PDA was performed at an oxygen pressure of  $10^{-5}$  mbar at three different temperatures (200°C, 400°C, and 600°C) keeping one part as a reference sample.

After the film preparation and after PDA *in-situ* XPS measurements were performed to determine the magnesium content diffused into the film. Due to contaminations of the sample surface it was not possible to record LEED images after removal from UHV and the following PDA.

Afterwards, the samples were removed from the UHV system for *ex-situ* XRD measurements at the high resolution x-ray scattering beamline P08 at Petra III, Desy [56], using a photon energy of 12.38 keV ( $\lambda = 1 \text{ \AA}$ ). The diffraction measurements were performed using a specular geometry (XRD) as well as using a grazing incidence (GIXRD) setup.

## 8.3. Results

### X-ray photoemission spectroscopy

Fig. 8.1 a) and b) show measurements of the Fe2p and Fe3p peak region, respectively. The Fe2p region of the as-deposited sample shows no satellite peaks indicating a  $\text{Fe}_3\text{O}_4$

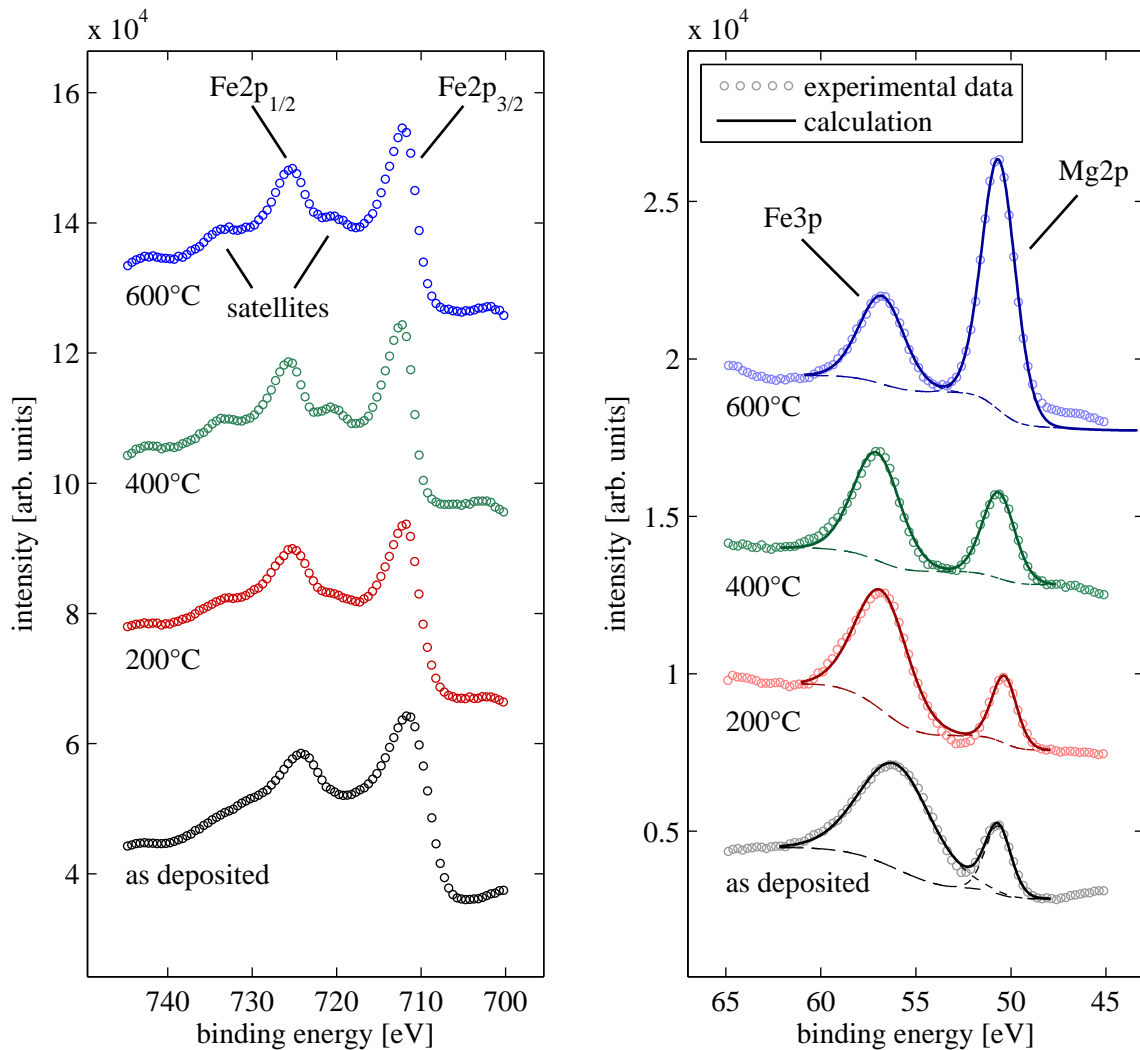


**Fig. 8.1:** XPS measurements of the Fe2p (a) and the Fe3p (b) peak regions for the as-deposited sample and the PDA samples.

stoichiometry [41], while for all annealed samples satellites are visible. The satellites indicate a shift of the film oxide phase from  $\text{Fe}_3\text{O}_4$  towards  $\text{Fe}_2\text{O}_3$ . They are most prominent for the sample annealed at  $400^\circ\text{C}$ . Thus, the  $400^\circ\text{C}$  sample has the highest oxidation state.

To estimate the magnesium diffusion into the film we studied the Fe3p peak region where the Mg2p peak is also present (cf. Fig 8.1). Curve fitting of this region was performed assuming two pseudo Voigt functions and a Shirley background. Fig 8.2 shows the relative iron and magnesium content obtained by the peak fitting taking the different cross sections into account.

We observe a magnesium concentration which is already very high (almost 50%) for the as-deposited film. With increasing PDA temperature the magnesium content increases. While the increase is relatively small for PDA at  $200^\circ\text{C}$  it becomes more pronounced at  $400^\circ\text{C}$  and  $600^\circ\text{C}$ .

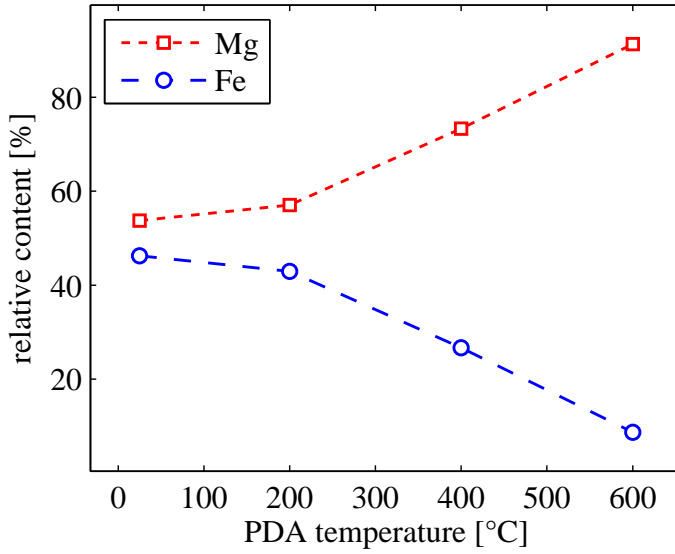


**Fig. 8.2:** Relative iron and magnesium content obtained by peak fitting of the Fe3p peak region.

### X-ray diffraction

X-ray diffraction CTR scans of the  $(00L)$  rod and the  $(01L)$  rod, obtained from the as-deposited film and the annealed films, were performed using specular (i.e.  $\theta - 2\theta$ ) and GIXRD geometry, respectively. For indexing of the Bragg peaks the surface coordinate system as described in Sec. 3.3 is used.

Measurements of the  $(00L)$  rod (cf. Fig 8.3) show clear fringes for the as-deposited film indicating a well ordered homogeneous crystalline iron oxide film and curve fitting using kinematic diffraction theory gives a film thickness of 3.3 nm. The films annealed at 200°C and 400°C also show clear fringes like the as-deposited film. For the film annealed at 200°C the fringes are slightly dampened compared to the as-deposited and the 400°C case. The sample annealed at 600°C shows no fringes and the iron oxide Bragg peak is not visible due to the overlapping with the more intense MgO substrate Bragg peak.

Fig. 8.4 shows CTR measurements of the  $(01L)$  rod performed in a GIXRD geometry. The as-deposited film shows fringes around  $L = 0.5$  indicating a homogeneous well ordered film. At  $L = 1$ , however, only a weak broad Bragg peak originating from the iron oxide film is observed. As explained in Sec. 3.3 the  $(01\frac{1}{2})$  Bragg peak originates exclusively from iron at octahedral sites while the  $(011)$  peak originates exclusively from iron at tetrahedral sites. With increasing PDA temperature the intensity of the  $(011)$  peak increases while the peak width is decreasing (cf. Fig. 8.5). For samples annealed at 200°C and 400°C fringes are still present at  $L = 0.5$ , but the sample annealed at 600°C shows no fringes and the iron oxide Bragg peak can not be observed due to the overlapping with the more intense substrate Bragg peak. Thus, at  $L = 0.5$  we observe essentially the same behavior as on the  $(00L)$  rod. However, the dampening of fringes for the 200°C sample mentioned above is even more prominent here.

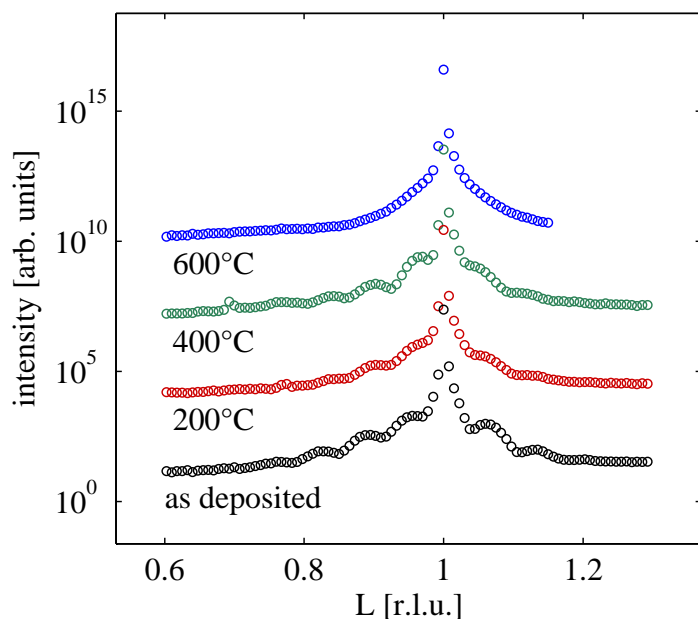


**Fig. 8.3:** XRD in specular geometry for the as-deposited film as well as the PDA samples.

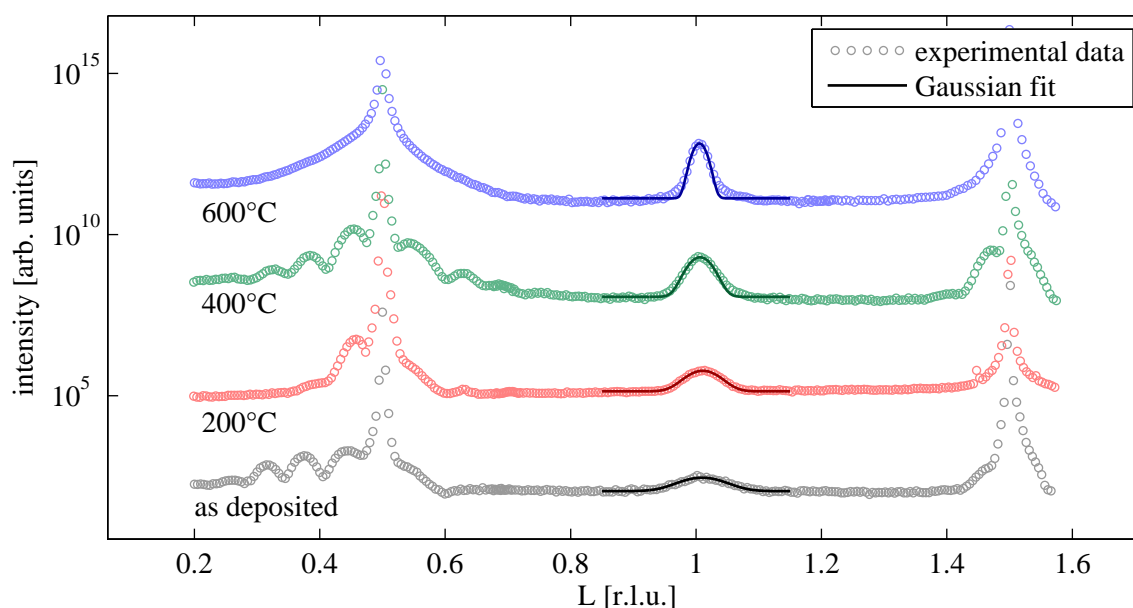


**Fig. 8.4:** CTR scans of the  $(01L)$  rod for the as-deposited sample and the PDA samples.

## 8.4. Discussion

The weak signal of the  $(011)$  Bragg peak for the as-deposited film indicates a weak ordered tetrahedral sublattice as expected from the studies presented in Chap. 7. With increasing PDA temperature the intensity of the peak increases while its width decreases. Thus, the order on the tetrahedral sites as well as the vertical domain size increases.

While the ordering on the tetrahedral sites increases a contrary effect is observed at the  $(001)$  and the  $(01\frac{1}{2})$  Bragg peak. The fringes originating from the iron oxide film at these Bragg

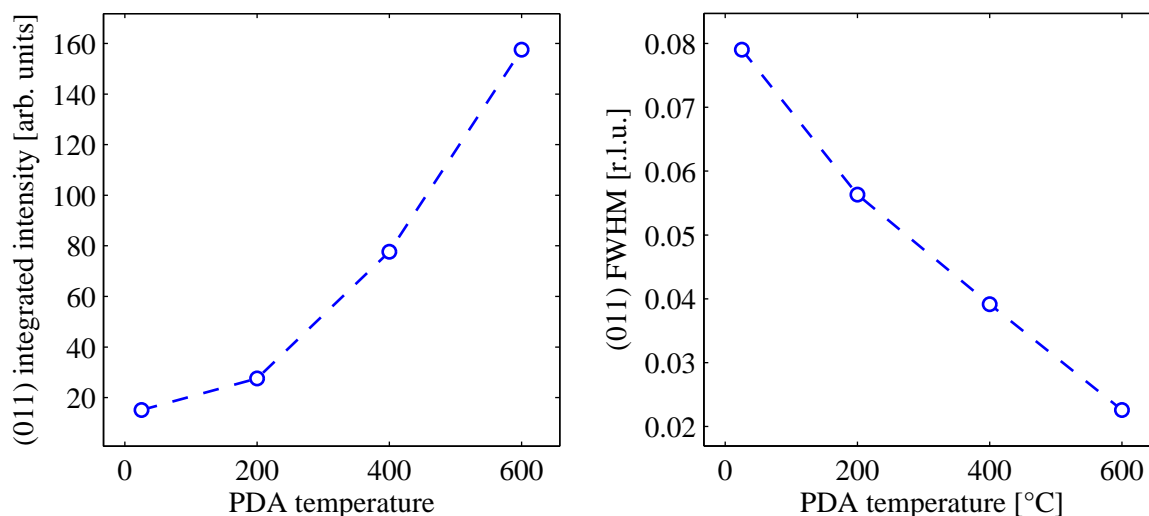


**Fig. 8.5:** Integrated intensity (a) and FWHM (b) of the (011) peak obtained by fitting a Gaussian function.

positions vanish for the 600°C sample and are slightly dampened for the 200°C sample. The vanishing of the fringes for the 600°C sample can be clearly attributed to an increased inhomogeneity within the film which is caused by the excessive diffusion of magnesium into the film as observed by XPS. For the 200°C sample the dampening remains unclear. As suggested by the XPS measurements the iron oxide film is oxidized due to the PDA. For the 400°C sample the highest oxidation state (close to  $\text{Fe}_2\text{O}_3$ ) is reached. Thus, the 200°C annealed film has an intermediate oxidation state. For the reduction of iron oxide films a dampening of the fringes for intermediate oxidation states was found by *in-situ* XRD measurements as described in the following chapter [99]. A similar effect could occur here for the oxidation. Another possible explanation is that the initial as-deposited film was not homogeneously covering the whole substrate area leading to small deviations in the film structure and composition for each of the four pieces leading to small deviations in the diffraction pattern.

The very high magnesium content initially observed is related to the very small film thickness of 3.3 nm. For deposition of magnetite at room temperature no diffusion of magnesium into the film is expected but the mean free path of the electrons was previously estimated to be  $\approx 5.3$  nm [93] for Fe3p and Mg2p photoelectrons. Since this value is larger than the film thickness obtained by XRD a large contribution to the XPS spectra is originating from the substrate. The strong increase of magnesium content with increasing PDA temperature is expected from reports in the literature, e.g. [77].

## 8.5. Conclusion

As shown by XRD measurements it is in fact possible to improve the ordering at the tetrahedral sites by PDA, where the ordering increases with increasing PDA temperature. However, the reordering is accompanied by significant diffusion of substrate magnesium into the film and increasing inhomogeneity within in the film.



---

Original publication: Journal of Applied Physics **110**, 102208 (2011).  
available at <http://dx.doi.org/10.1063/1.3661655>

## In-situ x-ray diffraction studies on post deposition annealing of ultra-thin iron oxide films

F. Bertram, C. Deiter, K. Pflaum, M. Suendorf, C. Otte, and J. Wollschläger

### Abstract

A maghemite ( $\gamma$ -Fe<sub>2</sub>O<sub>3</sub>) film of 8.3 nm thickness is epitaxially grown on MgO(001) single crystal substrate by reactive molecular beam epitaxy. Chemical composition and crystal structure of the surface was studied by x-ray photoelectron spectroscopy and low energy electron diffraction, respectively. Afterwards the sample was moved to a heating cell for *in-situ* x-ray diffraction experiments on the post-deposition annealing process in high-vacuum to study structural phase transitions of the iron oxide film. The iron oxide film is reduced with increasing temperature. This reduction occurs in two steps which are accompanied by structural transitions. The first step is a reduction from  $\gamma$ -Fe<sub>2</sub>O<sub>3</sub> to Fe<sub>3</sub>O<sub>4</sub> at 360°C and the second step is the reduction from Fe<sub>3</sub>O<sub>4</sub> to FeO at 410°C.



---

Original publication: Review of Scientific Instruments **83**, 083904 (2012).  
available at <http://dx.doi.org/10.1063/1.4746290>

## **A compact high vacuum heating chamber for in-situ x-ray scattering studies**

F. Bertram, C. Deiter, K. Pflaum, and O. H. Seeck

### **Abstract**

A very compact multi purpose high vacuum heating chamber for x-ray scattering techniques was developed. The compact design allows the chamber to be installed on high precision diffractometers which usually cannot support heavy and/or large equipment. The chamber is covered by a Be dome allowing full access to the hemisphere above the sample which is required for in-plane grazing incident x-ray diffraction and out-of plane wide angle x-ray diffraction.



# 11. Summary and outlook

The following chapter gives a short summary of the most important results obtained in this thesis together with an outlook on possible following research steps.

In this thesis the influence of deposition conditions and post-deposition annealing (PDA) on the structure of ultra thin iron oxide films grown on magnesium oxide (MgO) substrates has been studied.

Studying the dependency of film structure and thickness (Chap. 6), we showed that the iron oxide phase of MBE grown films is changing for fixed deposition conditions. For large film thickness (>20 nm) bulk like magnetite ( $\text{Fe}_3\text{O}_4$ ) structure and stoichiometry were observed. With decreasing film thickness the oxide phase is shifting towards a wüstite (FeO) phase. However, at a thickness of 6.1 nm the oxide phase is still closer to  $\text{Fe}_3\text{O}_4$  than FeO. In addition a FeO interface film of three atomic layers between the MgO substrate and the  $\text{Fe}_3\text{O}_4$  film was found. Also, XPS measurements revealed that no magnesium has diffused into the magnetite film. For the design of spintronic devices this suppression of magnesium diffusion into the magnetite film is essential since the magnesium contamination is weakening the magnetic properties of the magnetite film.

When changing deposition rate and substrate temperature a strong influence on the  $\text{Fe}_3\text{O}_4$  film structure was observed (Chap. 7). It was shown that the ordering of the tetrahedral sites of the inverse spinel lattice is strongly correlated with the deposition conditions while the ordering of the octahedral sites remains almost unaffected. For a high deposition rate and a substrate temperature of 250°C perfect ordering of the tetrahedral sites was observed. For lower deposition rates as well as lower substrate temperatures the ordering of the tetrahedral sites decreases and consequently the intensity of Bragg peaks originating exclusively from these sites also decreases. Here, we proposed a model that the ions usually occupying tetrahedral sites are relocated to octahedral vacancies.

In the following we studied the effect of PDA under low oxygen atmosphere on the structure of a  $\text{Fe}_3\text{O}_4$  film with an initially weak ordered tetrahedral sublattice (Chap. 8). The ordering of the tetrahedral sites improved with increasing PDA temperature. However, the increase in ordering is accompanied by a significant diffusion of magnesium into the iron oxide film and a decrease in film homogeneity.

The ordering of the tetrahedral sites is of special importance for the design of spintronic devices since the magnetic properties of  $\text{Fe}_3\text{O}_4$  are strongly correlated with its crystal structure. Therefore, additional work on this topic is required. Especially, experiments revealing the magnetic structure of the magnetite films should be performed and correlated with the atomic structure of the films. X-ray magnetic circular dichroism (XMCD) measurements should deliver detailed information on the spin polarization depending on the film structure. *In-situ* x-ray diffraction measurements could deliver a deeper insight into the reordering process driven by PDA under low oxygen conditions.

Studying the effect of PDA under high vacuum conditions on the structure of an ultra thin

maghemite ( $\gamma\text{-Fe}_2\text{O}_3$ ), which represents the highest oxidation state of all iron oxides, we observed a reduction of the iron oxide phase occurring in two steps (Chap. 9). The PDA was studied by *in-situ* x-ray diffraction measurements monitoring the vertical layer distance using a newly developed high vacuum chamber for *in-situ* x-ray scattering experiments (Chap. 10). Increasing the PDA temperature, first, a reduction from  $\gamma\text{-Fe}_2\text{O}_3$  to  $\text{Fe}_3\text{O}_4$  was observed. After further increasing the temperature a reduction from  $\text{Fe}_3\text{O}_4$  to  $\text{FeO}$  was observed. Thus, it is possible to select certain oxidation states of the iron oxide film using PDA.

In the present work only structural changes in vertical direction have been studied. Further studies including in-plane measurements could yield important information on the lateral structure of the film during the reduction process. Especially, it could be determined if the lateral lattice constant is pinned to its original value due to interactions with the substrate or if it changes due to the reduction process as observed for the vertical lattice constant.

## A. Derivation of the rms roughness model for x-ray diffraction

As derived in section 2.3.5 the diffracted intensity from a semi-infinite crystal substrate along a crystal truncation rod is given by

$$A_{\text{substrate}}(\mathbf{q}) = A_0 C F(\mathbf{q}) N_a N_b \frac{\left\langle e^{(i\mathbf{q} \cdot \mathbf{c} + \epsilon) N_c(n_a, n_b)} \right\rangle}{1 - e^{-(i\mathbf{q} \cdot \mathbf{c} + \epsilon)}} . \quad (\text{A.1})$$

In the following the average  $\left\langle e^{(i\mathbf{q} \cdot \mathbf{c} + \epsilon) N_c(n_a, n_b)} \right\rangle$  will be calculate. Assuming a Gaussian distribution of  $N_c(n_a, n_b)$ , the average can now be substituted by a summation over all  $n_c$ , which leads to

$$\left\langle e^{(i\mathbf{q} \cdot \mathbf{c} + \epsilon) N_c(n_a, n_b)} \right\rangle = \frac{1}{\sigma\sqrt{2\pi}} \sum_{n_c} e^{-\frac{(n_c - \overline{N}_c)^2}{2\sigma^2}} e^{(i\mathbf{q} \cdot \mathbf{c} + \epsilon) n_c} \quad (\text{A.2})$$

where  $\overline{N}_c$  is the average surface height. This summation can now be converted into a Integration. We obtain

$$\frac{1}{\sigma\sqrt{2\pi}} \sum_{n_c} e^{-\frac{(n_c - \overline{N}_c)^2}{2\sigma^2}} e^{(i\mathbf{q} \cdot \mathbf{c} + \epsilon) n_c} \quad (\text{A.3})$$

$$= \frac{1}{\sigma\sqrt{2\pi}} \int dn_c e^{-\frac{(n_c - \overline{N}_c)^2}{2\sigma^2}} e^{(i\mathbf{q} \cdot \mathbf{c} + \epsilon) n_c} \sum_m \delta(n_c - m) . \quad (\text{A.4})$$

Neglecting the contribution from  $\epsilon$  this integration is the Fourier transformed  $\mathcal{F}$  of  $e^{-\frac{(n_c - \overline{N}_c)^2}{2\sigma^2}} \sum_m \delta(n_c - m)$ . We can write

$$\left\langle e^{(i\mathbf{q} \cdot \mathbf{c} + \epsilon) N_c(n_a, n_b)} \right\rangle = \frac{1}{\sigma\sqrt{2\pi}} \int dn_c e^{-\frac{(n_c - \overline{N}_c)^2}{2\sigma^2}} e^{i\mathbf{q} \cdot \mathbf{c} n_c} \sum_m \delta(n_c - m) \quad (\text{A.5})$$

$$= \mathcal{F} \left\{ \frac{1}{\sigma\sqrt{2\pi}} e^{-\frac{(n_c - \overline{N}_c)^2}{2\sigma^2}} \sum_m \delta(n_c - m) \right\} \quad (\text{A.6})$$

$$= \mathcal{F} \left\{ \frac{1}{\sigma\sqrt{2\pi}} e^{-\frac{(n_c - \overline{N}_c)^2}{2\sigma^2}} \right\} \otimes \mathcal{F} \left\{ \sum_m \delta(n_c - m) \right\} \quad (\text{A.7})$$

$$= \left( e^{-\frac{\sigma^2(\mathbf{q} \cdot \mathbf{c})^2}{2}} e^{i\mathbf{q} \cdot \mathbf{c} \overline{N_c}} \right) \otimes \sum_{\nu} \delta(\mathbf{q} \cdot \mathbf{c} - 2\pi\nu) \quad (\text{A.8})$$

$$\stackrel{\overline{N_c}=0}{=} e^{-\frac{\sigma^2(\mathbf{q} \cdot \mathbf{c})^2}{2}} \otimes \sum_{\nu} \delta(\mathbf{q} \cdot \mathbf{c} - 2\pi\nu) . \quad (\text{A.9})$$

Thus, the average  $\left\langle e^{(i\mathbf{q} \cdot \mathbf{c} + \epsilon) N_c(n_a, n_b)} \right\rangle$  is given by the convolution of a Gaussian and a periodic repetition of  $\delta$ -functions with peaks where the Bragg condition is fulfilled as illustrated in Fig. A.1.

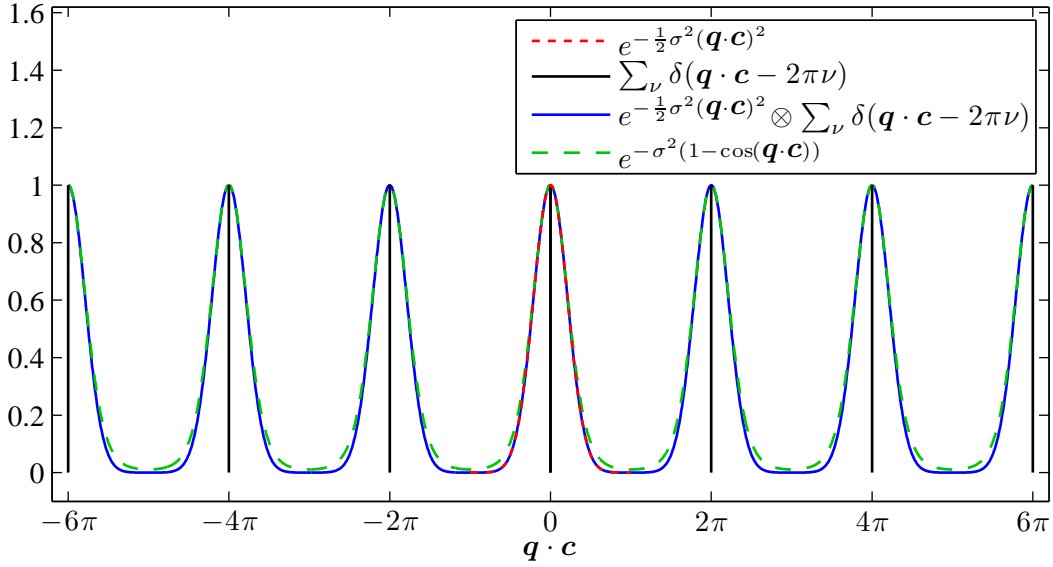


**Fig. A.1:** Gaussian peak shape, periodically iterated delta peaks, their convolution, and its approximation using a cos function for  $\sigma = 1.5$ .

To avoid the summation over the periodically repeated  $\delta$ -function the average is approximated using a periodic cos function. Thus, the averaging results in

$$\left\langle e^{(i\mathbf{q} \cdot \mathbf{c} + \epsilon) N_c(n_a, n_b)} \right\rangle = e^{-\sigma^2(1 - \cos(\mathbf{q} \cdot \mathbf{c}))} e^{(i\mathbf{q} \cdot \mathbf{c} + \epsilon) \overline{N_c}} . \quad (\text{A.10})$$

Therefore, the diffracted amplitude of a semi-infinite crystal assuming  $\overline{N_c} = 0$  is given by

$$A_{\text{substrate}}(\mathbf{q}) = A_0 C F(\mathbf{q}) N_a N_b \frac{\left\langle e^{(i\mathbf{q} \cdot \mathbf{c} + \epsilon) N_c(n_a, n_b)} \right\rangle}{1 - e^{-(i\mathbf{q} \cdot \mathbf{c} + \epsilon)}} \quad (\text{A.11})$$

$$= A_0 C F(\mathbf{q}) N_a N_b \frac{e^{-\sigma^2(1 - \cos \mathbf{q} \cdot \mathbf{c})}}{1 - e^{-(i\mathbf{q} \cdot \mathbf{c} + \epsilon)}} . \quad (\text{A.12})$$

## B. List of publications

### Peer-reviewed publications

- T. Weisemoeller, C. Deiter, F. Bertram, S. Gevers, A. Giussani, P. Zaumseil, T. Schroeder, and J. Wollschläger  
"Epitaxy of single crystalline PrO<sub>2</sub> films on Si(111)"  
*Applied Physics Letters* **93**, 032905 (2008)  
[doi:10.1063/1.2958227](https://doi.org/10.1063/1.2958227)
- G. Jnawali, H. Hattab, C. A. Bobisch, A. Bernhart, E. Zubkov, C. Deiter, T. Weisemoeller, F. Bertram, J. Wollschläger, R. Möller, and M. Horn-von Hoegen  
"Epitaxial Growth of Bi(111) on Si(001)"  
*e-Journal of Surface Science and Nanotechnology* **7**, 441 (2009)  
[doi:10.1380/ejsnt.2009.441](https://doi.org/10.1380/ejsnt.2009.441)
- S. Gevers, T. Weisemoeller, B. Zimmermann, F. Bertram, C. Deiter, and J. Wollschläger  
"Structural phase transition of ultra thin PrO<sub>2</sub> films on Si(111)"  
*Journal of Physics: Condensed Matter* **21**, 175408 (2009)  
[doi:10.1088/0953-8984/21/17/175408](https://doi.org/10.1088/0953-8984/21/17/175408)
- T. Weisemoeller, F. Bertram, S. Gevers, A. Greuling, C. Deiter, H. Tobergte, M. Neumann, A. Giussani, T. Schroeder, and J. Wollschläger  
"Post deposition annealing induced transition from hexagonal Pr<sub>2</sub>O<sub>3</sub> to cubic PrO<sub>2</sub> films on Si(111)"  
*Journal of Applied Physics* **105**, 124108 (2009)  
[doi:10.1063/1.3152796](https://doi.org/10.1063/1.3152796)
- T. Weisemoeller, F. Bertram, S. Gevers, C. Deiter, A. Greuling, and J. Wollschläger  
"Effect of amorphous interface layers on crystalline thin film X-ray diffraction"  
*Physical Review B* **79**, 245422 (2009)  
[doi:10.1103/PhysRevB.79.245422](https://doi.org/10.1103/PhysRevB.79.245422)
- E. Wintersberger, N. Hrauda, D. Krieger, M. Keplinger, G. Springholz, J. Stangl, G. Bauer, J. Oswald, T. Belytschko, C. Deiter, F. Bertram, and O. H. Seeck  
"Analysis of periodic dislocation networks using x-ray diffraction and extended finite element modeling"  
*Applied Physics Letters* **96**, 131905 (2010)  
[doi:10.1063/1.3379298](https://doi.org/10.1063/1.3379298)
- T. Kuschel, T. Becker, D. Bruns, M. Suendorf, F. Bertram, P. Fumagalli, and J. Wollschläger  
"Uniaxial magnetic anisotropy for thin Co films on glass studied by magneto-optic Kerr effect"  
*Journal of Applied Physics* **109**, 093907 (2011)  
[doi:10.1063/1.3576135](https://doi.org/10.1063/1.3576135)

- F. Bertram, C. Deiter, K. Pflaum, M. Suendorf, C. Otte, and J. Wollschläger  
"In-situ x-ray diffraction studies on post-deposition vacuum-annealing of ultra-thin iron oxide films"  
*Journal of Applied Physics* **110**, 102208 (2011)  
[doi:10.1063/1.3661655](https://doi.org/10.1063/1.3661655)
- J. I. Flege, B. Kaemena, S. Gevers, F. Bertram, T. Wilkens, D. Bruns, J. Bätjer, T. Schmidt, and J. Wollschläger, and J. Falta  
"Silicate-free growth of high-quality ultrathin cerium oxide films on Si(111)"  
*Physical Review B* **84**, 235418 (2011)  
[doi:10.1103/PhysRevB.84.235418](https://doi.org/10.1103/PhysRevB.84.235418)
- O. H. Seeck, C. Deiter, K. Pflaum, F. Bertram, A. Beerlink, H. Franz, J. Horbach, H. Schulte-Schrepping, B. M. Murphy, M. Greve, and O. Magnussen  
"The High Resolution Diffraction beamline P08 at Petra III"  
*Journal of Synchrotron Radiation* **19**, 30 (2012)  
[doi:10.1107/S0909049511047236](https://doi.org/10.1107/S0909049511047236)
- F. Bertram, C. Deiter, K. Pflaum, and O. H. Seeck  
"A compact high vacuum heating chamber for *in-situ* X-ray scattering studies"  
*Review of Scientific Instruments* **83**, 083904 (2012)  
[doi:10.1063/1.4746290](https://doi.org/10.1063/1.4746290)
- F. Bertram, C. Deiter, O. Hoefert, M. Suendorf, T. Schemme, F. Timmer, B. Zimmermann, and J. Wollschläger  
"X-ray diffraction study on size effects in epitaxial magnetite thin films on MgO(001)"  
*Journal of Physics D: Applied Physics* **45**, 395302 (2012)  
[doi:10.1088/0022-3727/45/39/395302](https://doi.org/10.1088/0022-3727/45/39/395302)
- F. Bertram, C. Deiter, T. Schemme, S. Jentsch, and J. Wollschläger  
"Reordering between tetrahedral and octahedral sites in ultrathin magnetite films grown on MgO(001)"  
*Journal of Applied Physics* **113**, 184103 (2013)  
[doi:10.1063/1.4803894](https://doi.org/10.1063/1.4803894)

## Non reviewed publications

- F. Bertram, O. Hoefert, M. Suendorf, B. Zimmermann, C. Deiter, S. Gevers, T. Weismöller, and J. Wollschläger  
"GIXRD and XRD studies on epitaxial magnetite ultra thin films on MgO(001)"  
*HASYLAB Annual Report* (2008)
- T. Kuschel, F. Timmer, O. Hoefert, B. Zimmermann, C. Deiter, M. Suendorf, S. Gevers, F. Bertram, and J. Wollschläger  
"XRR and XRD studies on ultra thin Fe-films on MgO(001)"  
*HASYLAB Annual Report* (2008)
- B. Zimmermann, F. Bertram, O. Hoefert, C. Deiter, M. Suendorf, and J. Wollschläger  
"Ultrathin magnetite films on MgO(001) studied by XRR and XRD"  
*HASYLAB Annual Report* (2008)

- 
- S. Gevers, F. Bertram, T. Weisemoeller, C. Deiter, and J. Wollschläger  
 "GIXRD and XRD studies of phase transformations of thin PrO<sub>2</sub> films on Si(111)"  
*HASYLAB Annual Report* (2008)
  - M. Suendorf, T. Kuschel, S. Gevers, D. Bruns, A. Knobeler, H. Wilkens, F. Bertram, and J. Wollschläger  
 "XRR and XRD studies on thin Fe-films grown on MgO(001)"  
*HASYLAB Annual Report* (2009)
  - E. Wintersberger, N. Hrauda, D. Krieger, M. Keplinger, G. Springholz, J. Stangl, G. Bauer, J. Oswald, T. Belytschko, C. Deiter, F. Bertram, and O.H. Seeck  
 "Investigation of periodic dislocation-networks in PbSe epilayers on PbTe by x-ray diffraction"  
*HASYLAB Annual Report* (2009)
  - B. Menkens, J.I. Flege, S. Gevers, F. Bertram, C. Deiter, J. Wollschläger, and J. Falta  
 "Epitaxial growth of ultra-thin ceria films on Cl-passivated Si(111)"  
*HASYLAB Annual Report* (2009)
  - J. Wollschläger, F. Bertram, C. Deiter, O. Hoefert, M. Suendorf, and B. Zimmermann  
 "Combined XRD and XPS studies on size effects in epitaxial magnetite ultrathin films on MgO(001)"  
*HASYLAB Annual Report* (2009)
  - C. Otte, M. Suendorf, T. Kuschel, S. Gevers, D. Bruns, H. Wilkens, F. Bertram, and J. Wollschläger  
 "XRR and XRD studies on thin Fe-films on MgO(001)"  
*HASYLAB Annual Report* (2010)
  - J.I. Flege, B. Kaemena, T. Wilkens, S. Gevers, F. Bertram, C. Deiter, J. Wollschläger, and J. Falta  
 "Interfacant-mediated epitaxial growth of cerium oxide films on Si(111)"  
*HASYLAB Annual Report* (2010)
  - F. Bertram, C. Deiter, K. Pflaum, M. Suendorf, C. Otte, and J. Wollschläger  
 "In-situ XRD-studies on post-deposition vacuum-annealing of ultra-thin iron oxide films"  
*HASYLAB Annual Report* (2010)
  - F. Bertram, C. Deiter, S. Jentsch, T. Schemme, and J. Wollschläger  
 "Disorder on tetrahedral sites of ultra thin magnetite films grown on MgO(001)"  
*HASYLAB Annual Report* (2011)
  - F. Bertram  
 "A compact high vacuum heating chamber for X-ray scattering"  
 Photon Science 2011, DESY (2011)



## Literature

- [1] S. A. Wolf, D. D. Awschalom, R. A. Buhrman, J. M. Daughton, S. von Molnar, M. L. Roukes, A. Y. Chtchelkanova and D. M. Treger. “Spintronics: A Spin-Based Electronics Vision for the Future”. *Science*, 294, 1488, 2001. doi:[10.1126/science.1065389](https://doi.org/10.1126/science.1065389).
- [2] I. Zutic, J. Fabian and S. Das Sarma. “Spintronics: Fundamentals and applications”. *Rev. Mod. Phys.*, 76(2), 323, 2004. doi:[10.1103/RevModPhys.76.323](https://doi.org/10.1103/RevModPhys.76.323).
- [3] M. Julliere. “tunneling between ferromagnetic films”. *Phys. Lett.*, 54A, 225, 1975. doi:[10.1016/0375-9601\(75\)90174-7](https://doi.org/10.1016/0375-9601(75)90174-7).
- [4] E. Y. Tsymbal, O. N. Meyasov and P. R. LeClair. “Spin-dependent tunnelling in magnetic tunnel junctions”. *J. Phys.: Condens. Matter*, 15, R109, 2003. doi:[10.1088/0953-8984/15/4/201](https://doi.org/10.1088/0953-8984/15/4/201).
- [5] M. Bibes and A. Barthelemy. “Oxide Spintronics”. *IEEE Trans. Electron. Devices*, 54, 1003, 2007. doi:[10.1109/TED.2007.894366](https://doi.org/10.1109/TED.2007.894366).
- [6] S. Ikeda, J. Hayakawa, Y. M. Lee, F. Matsukura, Y. Ohno, T. Hanyu and H. Ohno. “Magnetic Tunneling Junctions for Spintronic Memories and Beyond”. *IEEE Trans. Electron. Devices*, 54, 991, 2007. doi:[10.1109/TED.2007.894617](https://doi.org/10.1109/TED.2007.894617).
- [7] D. Mahajan, P. Gütlich and U. Stumm. “The role of nano-sized iron particles in slurry phase Fischer-Tropsch synthesis”. *Catal. Commun.*, 4, 101, 2003. doi:[10.1016/S1566-7367\(03\)00002-5](https://doi.org/10.1016/S1566-7367(03)00002-5).
- [8] C. H. F. Peden, G. S. Herman, I. Z. Ismagilov, B. D. Kay, M. A. Henderson, Y. J. Kim and S. A. Chambers. “Model catalyst studies with single crystals and epitaxial thin oxide films”. *Catal. Today*, 51, 513, 1999. doi:[10.1016/S0920-5861\(99\)00037-1](https://doi.org/10.1016/S0920-5861(99)00037-1).
- [9] S. Wagloehner, D. Reichert, D. Leon-Sorzano, P. Balle, B. Geiger and S. Kureti. “Kinetic modeling of the oxidation of CO on Fe<sub>2</sub>O<sub>3</sub> catalyst in excess of O<sub>2</sub>”. *J. Catal.*, 260, 305, 2008. doi:[10.1016/j.jcat.2008.09.018](https://doi.org/10.1016/j.jcat.2008.09.018).
- [10] A. K. Kandalam, B. Chatterjee, S. N. Khanna, B. K. Rao, P. Jena and B. V. Reddy. “Oxidation of CO on Fe<sub>2</sub>O<sub>3</sub> model surfaces”. *Surf. Sci.*, 601, 4873, 2007. doi:[10.1016/j.susc.2007.08.015](https://doi.org/10.1016/j.susc.2007.08.015).
- [11] A. A. Herzing, C. J. Kiely, A. F. Carley, P. Landon and G. J. Hutchings. “Identification of active gold nanoclusters on iron oxide supports for CO oxidation”. *Science*, 321, 1331, 2008. doi:[10.1126/science.1159639](https://doi.org/10.1126/science.1159639).
- [12] R. Arras, L. Calmels and B. Warot-Fonrose. “Interface states in the full-oxide Fe<sub>3</sub>O<sub>4</sub>-MgO-Fe<sub>3</sub>O<sub>4</sub> magnetic tunnel junction”. *IEEE Trans. Magn.*, 46, 1730, 2010. doi:[10.1109/TMAG.2010.2042577](https://doi.org/10.1109/TMAG.2010.2042577).
- [13] P. F. Fewster. “X-ray analysis of thin films and multilayers”. *Rep. Prog. Phys.*, 59, 1339, 1996. doi:[10.1088/0034-4885/59/11/001](https://doi.org/10.1088/0034-4885/59/11/001).

- [14] M. Birkholz. *Thin Film Analysis by X-Ray Scattering*. WILEY-VCH Verlag GmbH & Co. KGaA, Weinheim, 2006.
- [15] J. Als-Nielsen and D. McMorrow. *Elements of Modern X-Ray Physics*. John Wiley & Sons Inc., 2000. doi:[10.1002/9781119998365](https://doi.org/10.1002/9781119998365).
- [16] T. Möller and J. Falta (Editors). *Forschung mit Synchrotronstrahlung: Eine Einführung in die Grundlagen und Anwendungen*. Vieweg+Teubner Verlag, 2010.
- [17] N. W. Ashcroft and D. N. Mermin. *Festkörperphysik*. Oldenbourg Wissenschaftsverlag, 2001.
- [18] C. Kittel. *Einführung in die Festkörperphysik*. Oldenbourg Wissenschaftsverlag, 2006.
- [19] K. Oura, V. Lifshits, A. Saranin and M. Katayama. *Surface Science*. Springer, 2003.
- [20] B. Warren. *X-ray Diffraction*. Dover publications Inc., 1990.
- [21] W. Friedrich, P. Knipping and M. Laue. “Interferenz-Erscheinungen bei Röntgenstrahlen”. *Die Naturwissenschaften*, 16, 361, 1952. doi:[10.1007/BF00646957](https://doi.org/10.1007/BF00646957).
- [22] W. H. Bragg and W. L. Bragg. “The reflection of X-rays by crystals”. *Proc. R. Soc. Lond. A*, 88, 428, 1913. doi:[10.1098/rspa.1913.0040](https://doi.org/10.1098/rspa.1913.0040).
- [23] R. Feidenhans'l. “Surface structure determination by x-ray diffraction”. *Surface Science Reports*, 10, 105, 1989. doi:[10.1016/0167-5729\(89\)90002-2](https://doi.org/10.1016/0167-5729(89)90002-2).
- [24] I. K. Robinson and D. J. Tweet. “Surface x-ray diffraction”. *Rep. Prog. Phys.*, 55, 599, 1992. doi:[10.1088/0034-4885/55/5/002](https://doi.org/10.1088/0034-4885/55/5/002).
- [25] C. Deiter. *Röntgenstrukturanalyse von Halbleiter-Isolator-Schichtsystemen*. Ph.D. thesis, Universität Bremen, 2005.
- [26] *International tables for X-ray crystallography*. Birmingham, Kynoch Press for the International Union of Crystallography, 3 edition, 1976.
- [27] M. Tolan. *X-Ray Scattering from Soft-Matter Thin Films - Materials Science and Basic Research*. Springer-Verlag, Berlin, Heidelberg, 1999.
- [28] L. G. Parratt. “Surface Studies of Solids by Total Reflection of X-Rays”. *Phys. Rev.*, 95, 359, 1954. doi:[10.1103/PhysRev.95.359](https://doi.org/10.1103/PhysRev.95.359).
- [29] L. Névoit and P. Croce. “Caractérisation des surfaces par réflexion rasante de rayons X. Application à l'étude du polissage de quelques verres silicates”. *Rev. Phys. Appl.*, 15, 761, 1980. doi:[10.1051/rphysap:01980001503076100](https://doi.org/10.1051/rphysap:01980001503076100).
- [30] J. D. Levine, S. H. McFarlane and P. Mark. “Si (111)  $7 \times 7$  surface structure: Calculations of LEED intensity and comparison with experiment”. *Phys. Rev. B*, 16, 5415, 1977. doi:[10.1103/PhysRevB.16.5415](https://doi.org/10.1103/PhysRevB.16.5415).
- [31] H. Lüth. *Solid Surfaces, Interfaces and Thin Films*. Springer, 4. edition, 2001.
- [32] G. Ketteler, W. Weiss, W. Ranke and R. Schlögl. “Bulk and surface phases of iron oxides in an oxygen and water atmosphere at low pressure”. *Phys. Chem. Chem. Phys.*, 3, 1114, 2001. doi:[10.1039/b009288f](https://doi.org/10.1039/b009288f).
- [33] R. M. Hazen and R. Jeanloz. “Wüstite ( $\text{Fe}_{1-x}\text{O}$ ): a review of its defect structure and physical properties”. *Rev. Geophys.*, 22, 37, 1984. doi:[10.1029/RG022i001p00037](https://doi.org/10.1029/RG022i001p00037).
- [34] R. J. Hill, J. R. Craig and G. V. Gibbs. “Systematics of the Spinel Structure Type”. *Phys. Chem. Minerals*, 4, 317, 1979. doi:[10.1007/BF00307535](https://doi.org/10.1007/BF00307535).

- [35] F. Walz. “The Verwey transition - a topical review”. *J. Phys.: Condens. Matter*, 14, R285, 2002. doi:[10.1088/0953-8984/14/12/203](https://doi.org/10.1088/0953-8984/14/12/203).
- [36] B. Zimmermann. *Epitaktisches Wachstum und Charakterisierung ultradünner Eisenoxidschichten auf Magnesiumoxid(001)*. Ph.D. thesis, Universität Osnabrück, 2010.
- [37] J. F. Anderson, M. Kuhn, U. Diebold, K. Shaw, P. Stoyanov and D. Lind. “Surface structure and morphology of Mg-segregated epitaxial  $\text{Fe}_3\text{O}_4(001)$  thin films on  $\text{MgO}(001)$ ”. *Phys. Rev. B*, 56, 9902, 1997. doi:[10.1103/PhysRevB.56.9902](https://doi.org/10.1103/PhysRevB.56.9902).
- [38] J. Korecki, B. Handke, N. Spiridis, T. Slezak, F. Flis-Kabulska and J. Haber. “Size effects in epitaxial films of magnetite”. *Thin Solid Films*, 412, 14, 2002. doi:[10.1016/S0040-6090\(02\)00306-1](https://doi.org/10.1016/S0040-6090(02)00306-1).
- [39] R. Pentcheva, W. Moritz, J. Rundgren, S. Frank, D. Schrupp and M. Scheffler. “A combined DFT/LEED-approach for complex oxide surface structure determination:  $\text{Fe}_3\text{O}_4(001)$ ”. *Surf. Sci.*, 602(7), 1299, 2008. doi:[10.1016/j.susc.2008.01.006](https://doi.org/10.1016/j.susc.2008.01.006).
- [40] N. Spiridis, J. Barbasz, Z. Łodziana and J. Korecki. “ $\text{Fe}_3\text{O}_4(001)$  films on  $\text{Fe}(001)$ : Termination and reconstruction of iron-rich surfaces”. *Phys. Rev. B*, 74, 155423, 2006. doi:[10.1103/PhysRevB.74.155423](https://doi.org/10.1103/PhysRevB.74.155423).
- [41] T. Yamashita and P. Hayes. “Analysis of XPS spectra of  $\text{Fe}^{2+}$  and  $\text{Fe}^{3+}$  ions in oxide materials”. *Appl. Surf. Sci.*, 254, 2441, 2008. doi:[10.1016/j.apsusc.2007.09.063](https://doi.org/10.1016/j.apsusc.2007.09.063).
- [42] T. Fujii, F. de Groot, G. Sawatzky, V. F.C., T. Hibma and K. Okada. “In situ XPS analysis of various iron oxide films grown by  $\text{NO}_2$ -assisted molecular-beam epitaxy”. *Phys. Rev. B*, 59, 3195, 1999. doi:[10.1103/PhysRevB.59.3195](https://doi.org/10.1103/PhysRevB.59.3195).
- [43] Y. Gao and S. A. Chambers. “Heteroepitaxial growth of  $\alpha\text{-Fe}_2\text{O}_3$ ,  $\gamma\text{-Fe}_2\text{O}_3$  and  $\text{Fe}_3\text{O}_4$  thin films by oxygen-plasma-assisted molecular beam epitaxy”. *J. Cryst. Growth*, 174(1-4), 446, 1997. doi:[10.1016/S0022-0248\(96\)01141-4](https://doi.org/10.1016/S0022-0248(96)01141-4).
- [44] S. A. Chambers and S. A. Joyce. “Surface termination, composition and reconstruction of  $\text{Fe}_3\text{O}_4(001)$  and  $\gamma\text{-Fe}_2\text{O}_3(001)$ ”. *Surf. Sci.*, 420, 111, 1999. doi:[10.1016/S0039-6028\(98\)00657-8](https://doi.org/10.1016/S0039-6028(98)00657-8).
- [45] W. Eerenstein, T. T. M. Palstra, T. Hibma and S. Celotto. “Origin of the increased resistivity in epitaxial  $\text{Fe}_3\text{O}_4$  films”. *Phys. Rev. B*, 66, 201101, 2002. doi:[10.1103/PhysRevB.66.201101](https://doi.org/10.1103/PhysRevB.66.201101).
- [46] Y. Gao, Y. J. Kim and S. A. Chambers. “Preparation and characterization of epitaxial iron oxide films”. *J. Mater. Res.*, 13, 2003, 1998. doi:[10.1557/JMR.1998.0281](https://doi.org/10.1557/JMR.1998.0281).
- [47] B. Handke, J. Habber, T. Slezak, M. Kubik and J. Korecki. “Magnesium interdiffusion and surface oxidation in magnetite epitaxial films grown on  $\text{MgO}(100)$ ”. *Vacuum*, 63, 331, 2001. doi:[10.1016/S0042-207X\(01\)00209-3](https://doi.org/10.1016/S0042-207X(01)00209-3).
- [48] F. C. Voogt, T. Fujii, P. J. M. Smulders, L. Niesen, M. A. James and T. Hibma. “ $\text{NO}_2$ -assisted molecular-beam epitaxy of  $\text{Fe}_3\text{O}_4$ ,  $\text{Fe}_{3-\delta}\text{O}_4$ , and  $\gamma\text{-Fe}_2\text{O}_3$  thin films on  $\text{MgO}(100)$ ”. *Phys. Rev. B*, 60, 11193, 1999. doi:[10.1103/PhysRevB.60.11193](https://doi.org/10.1103/PhysRevB.60.11193).
- [49] K. A. Shaw, E. Lochner and D. M. Lind. “Interdiffusion study of magnesium in magnetite thin films grown on magnesium oxide (001) substrates”. *J. Appl. Phys.*, 87, 1727, 2000. doi:[10.1063/1.372084](https://doi.org/10.1063/1.372084).
- [50] C. Ruby, B. Humbert and J. Fusy. “Surface and interface properties of epitaxial iron oxide thin films deposited on  $\text{MgO}(001)$  studied by

- XPS and Raman spectroscopy”. *Surf. Interface Anal.*, 29, 377, 2000. doi:[10.1002/1096-9918\(200006\)29:6<377::AID-SIA879>3.0.CO;2-F](https://doi.org/10.1002/1096-9918(200006)29:6<377::AID-SIA879>3.0.CO;2-F).
- [51] N. Spiridis, B. Handke, T. Slezak, J. Barbasz, M. Zajac, J. Haber and J. Korecki. “Surface structure of epitaxial magnetite  $\text{Fe}_3\text{O}_4(001)$  films: In-situ STM and CEMS studies”. *J. Phys. Chem. B*, 108, 14356, 2004. doi:[10.1021/jp049935i](https://doi.org/10.1021/jp049935i).
- [52] T. Hibma, V. F.C., L. Niesen, P. A. A. van der Heijden, W. J. M. de Jong, J. J. T. M. Donkers and P. J. van der Zaag. “Anti-phase domains and magnetism in epitaxial magnetite layers”. *J. Appl. Phys.*, 85, 5291, 199. doi:[10.1063/1.369857](https://doi.org/10.1063/1.369857).
- [53] W. Eerenstein, T. T. M. Palstra, T. Hibma and S. Celotto. “Diffusive motion of antiphase domain boundaries in  $\text{Fe}_3\text{O}_4$  films”. *Phys. Rev. B*, 68, 014428, 2003. doi:[10.1103/PhysRevB.68.014428](https://doi.org/10.1103/PhysRevB.68.014428).
- [54] S. Celotto, W. Eerenstein and T. Hibma. “Characterization of anti-phase boundaries in epitaxial magnetite films”. *Eur. Phys. J. B*, 36, 271, 2003. doi:[10.1140/epjb/e2003-00344-7](https://doi.org/10.1140/epjb/e2003-00344-7).
- [55] HASYLAB, [http://hasylab.desy.de/facilities/doris\\_iii/beamlines/w1\\_roewi/index\\_eng.html](http://hasylab.desy.de/facilities/doris_iii/beamlines/w1_roewi/index_eng.html).
- [56] O. Seeck, C. Deiter, K. Pflaum, F. Bertram, A. Beerlink, J. Franz, H. Horbach, H. Schulte-Schrepping, B. Murphy, M. Greve and O. Magnussen. “The high-resolution diffraction beamline P08 at PETRA III”. *J. Synchrotron Rad.*, 19, 30, 2012. doi:[10.1107/S0909049511047236](https://doi.org/10.1107/S0909049511047236).
- [57] K. Wille. *Physik der Teilchenbeschleuniger und Synchrotronstrahlungsquellen*. B. G. Teubner Stuttgart, 2 edition, 1996.
- [58] L. Bittner, U. Hahn, G. Krämer and V. Saile. “Ein Toroidspiegel zur Fokussierung der Röntgenstrahlung vom Wiggler”. *HASYLAB Annual Report*, page 286, 1985.
- [59] Y. Sakayangi. “Theoretical approach to x-ray imaging by toroidal mirrors”. *OPTICA ACTA*, 23, 217, 1976.
- [60] J. Voss, C. Kunz, A. Moewes and I. Storjohann. “Grazing-incidence optics for soft-x-ray microscopy”. *Rev. Sci. Inst.*, 63, 569, 1992. doi:[10.1063/1.1142707](https://doi.org/10.1063/1.1142707).
- [61] S. Snigirev, V. Kohn, I. Snigireva, A. Souvorov and B. Lengeler. “Focusing high-energy x rays by compound refractive lenses”. *Applied Optics*, 37, 653, 1998. doi:[10.1364/AO.37.000653](https://doi.org/10.1364/AO.37.000653).
- [62] S. Krüger, K. Giewekemeyer, S. Kalbfleisch, M. Bartels, H. Neubauer and T. Saldit. “Sub-15 nm beam confinement by two crossed x-ray waveguides”. *Opt. Express*, 18, 13492, 2010. doi:[10.1364/OE.18.013492](https://doi.org/10.1364/OE.18.013492).
- [63] T. Arnold, C. Nicklin, J. Rawle, J. Sutter, T. Bates, B. Nutter, G. McIntyre and M. Burt. “Implementation of a beam deflection system for studies of liquid interfaces on beamline I07 at Diamond”. *J. Synchrotron Rad.*, 19(3), 408, 2012. doi:[10.1107/S0909049512009272](https://doi.org/10.1107/S0909049512009272).
- [64] M. Lohmeier and E. Vlieg. “Angle calculations for a six-circle surface X-ray diffractometer”. *J. Appl. Cryst.*, 26, 706, 1993. doi:[10.1107/S0021889893004868](https://doi.org/10.1107/S0021889893004868).
- [65] H. You. “Angle calculations for a ‘4S+2D’ six-circle diffractometer”. *J. Appl. Cryst.*, 32, 614, 1999. doi:[10.1107/S0021889899001223](https://doi.org/10.1107/S0021889899001223).

- [66] B. Schmitt, C. Brönnimann, E. Eikenberry, F. Gozzo, C. Hörmann, R. Horisberger and B. Patterson. “Mythen detector system”. *Nucl. instrum. meth. A*, 501, 267, 2003. doi:[10.1016/S0168-9002\(02\)02045-4](https://doi.org/10.1016/S0168-9002(02)02045-4).
- [67] T. Kracht. *ONLINE*, <http://hasyweb.desy.de/services/computing/online/online.html>.
- [68] E. Vlieg. “Integrated Intensities Using a Six-Circle Surface X-ray Diffractometer”. *J. Appl. Cryst.*, 30, 232, 1997. doi:[10.1107/S0021889897002537](https://doi.org/10.1107/S0021889897002537).
- [69] A. Greuling. *Röntgenstrukturanalyse von Isolatorschichten*. Master’s thesis, Universität Osnabrück, 2007.
- [70] S. Hahne. *Strukturanalyse von Praseodymoxidschichten mit Röntgenbeugung*. Bachelor’s thesis, Universität Osnabrück, 2008.
- [71] F. Bertram. *Röntgenstrukturanalyse von Oxidschichten*. Master’s thesis, Universität Osnabrück, 2009.
- [72] M. Wormington, C. Panaccione, K. Matney and D. Bowen. “Characterization of structures from X-ray scattering data using genetic algorithms”. *Phil. Trans. R. Soc. A*, 357, 2827, 1999. doi:[10.1098/rsta.1999.0469](https://doi.org/10.1098/rsta.1999.0469).
- [73] D. T. Margulies, F. T. Parker, F. E. Spada, R. S. Goldman, J. Li, R. Sinclair and A. E. Berkowitz. “Anomalous moment and anisotropy behavior in  $\text{Fe}_3\text{O}_4$  films”. *Phys. Rev. B*, 53, 9175, 1996. doi:[10.1103/PhysRevB.53.9175](https://doi.org/10.1103/PhysRevB.53.9175).
- [74] K. Balakrishnan, S. K. Arora and I. V. Shvets. “Strain relaxation studies of the  $\text{Fe}_3\text{O}_4/\text{MgO}$  (100) heteroepitaxial system grown by magnetron sputtering”. *J. Phys.: Condens. Matter*, 16, 5387, 2004. doi:[10.1088/0953-8984/16/30/001](https://doi.org/10.1088/0953-8984/16/30/001).
- [75] G. E. Sterbinsky, J. Cheng, P. T. Chiu, B. W. Wessels and D. J. Keavney. “Investigation of heteroepitaxial growth of magnetite thin films”. *J. Vac. Sci. Technol. B*, 25, 1389, 2007. doi:[10.1116/1.2757185](https://doi.org/10.1116/1.2757185).
- [76] L. Horng, G. Chern, M. C. Chen, P. C. Kang and D. S. Lee. “Magnetic anisotropic properties in  $\text{Fe}_3\text{O}_4$  and  $\text{CoFe}_2\text{O}_4$  ferrite epitaxy thin films”. *J. Magn. Magn. Mater.*, 270, 389, 2004. doi:[10.1016/j.jmmm.2003.09.005](https://doi.org/10.1016/j.jmmm.2003.09.005).
- [77] S. Thevuthasan, D. E. McCready, W. Jiang, S. I. Yi, S. Maheswaran, K. D. Keefer and S. Chambers. “Ion beam analysis of interface reactions in magnetite and maghemite thin films”. *Nucl. Instr. Meth. Phys. B*, 161-163, 510, 2000. doi:[10.1016/S0168-583X\(99\)00701-6](https://doi.org/10.1016/S0168-583X(99)00701-6).
- [78] N.-T. H. Kim-Ngan, A. G. Balogh, J. D. Meyer, J. Brötz, S. Hummelt, M. Zajac, T. Slezak and J. Korecki. “Structure, composition and crystallinity of epitaxial magnetite thin films”. *Surf. Sci.*, 602, 2358, 2008. doi:[10.1016/j.susc.2008.04.036](https://doi.org/10.1016/j.susc.2008.04.036).
- [79] N.-T. H. Kim-Ngan, A. G. Balogh, J. D. Meyer, J. . Brötz, M. Zajac, T. Slezak and J. Korecki. “Thermal and irradiation induced interdiffusion in magnetite thin films grown on magnesium oxide (001) substrates”. *Surf. Sci.*, 603, 1175, 2009. doi:[10.1016/j.susc.2009.02.028](https://doi.org/10.1016/j.susc.2009.02.028).
- [80] D. S. Lee, J. S. Wang, D. K. Modak, Y. S. Liu, C. L. Chang and G. Chern. “The magnetic properties of strained and relaxed  $\text{Fe}_{3-x}\text{Mg}_x\text{O}_4$  ferrite films on  $\text{MgO}$ (001) and  $\text{SrTiO}_3$ (001) by molecular beam epitaxy”. *J. Appl. Phys.*, 101, 09M523, 2007. doi:[10.1063/1.2712826](https://doi.org/10.1063/1.2712826).

- [81] T. Weisemoeller, F. Bertram, S. Gevers, C. Deiter, A. Greuling and J. Wollschläger. “Effect of amorphous interface layers on crystalline thin-film x-ray diffraction”. *Phys. Rev. B*, 79, 245422, 2009. doi:[10.1103/PhysRevB.79.245422](https://doi.org/10.1103/PhysRevB.79.245422).
- [82] T. Weisemoeller. *X-ray analysis of praseodymia*. Ph.D. thesis, Universität Osnabrück, 2009.
- [83] A. G. Every and A. K. McCurdy. *Table 7. Cubic system. Binary compounds*, volume 29a of *Landolt-Börnstein - Group III Condensed Matter Numerical Data and Functional Relationships in Science and Technology*. SpringerMaterials - The Landolt-Börnstein Database, 1992. doi:[10.1007/10046537\\_14](https://doi.org/10.1007/10046537_14).
- [84] J. Karunamuni, R. L. Kurtz and R. L. Stockbauer. “Growth of iron oxide on Cu(001) at elevated temperatures”. *Surf. Sci.*, 442, 223, 1999. doi:[10.1016/S0039-6028\(99\)00921-8](https://doi.org/10.1016/S0039-6028(99)00921-8).
- [85] G. D. Waddill and O. Ozturk. “Epitaxial growth of iron oxide films on Ag(111)”. *Surf. Sci.*, 575, 35, 2005. doi:[10.1016/j.susc.2004.10.050](https://doi.org/10.1016/j.susc.2004.10.050).
- [86] C. Schlueter, M. Lübke, A. M. Gigler and W. Moritz. “Growth of iron oxides on Ag(111) - Reversible Fe<sub>2</sub>O<sub>3</sub>/Fe<sub>3</sub>O<sub>4</sub> transformation”. *Surf. Sci.*, 605, 1986, 2011. doi:[10.1016/j.susc.2011.07.019](https://doi.org/10.1016/j.susc.2011.07.019).
- [87] S. Gota, E. Guiot, M. Henriot and M. Gautier-Soyer. “Atomic-oxygen-assisted MBE growth of  $\alpha$ -Fe<sub>2</sub>O<sub>3</sub> on  $\alpha$ -Al<sub>2</sub>O<sub>3</sub>: Metastable FeO(111)-like phase at subnanometer thicknesses”. *Phys. Rev. B*, 60, 14387, 1999. doi:[10.1103/PhysRevB.60.14387](https://doi.org/10.1103/PhysRevB.60.14387).
- [88] M. Ferhat and K. Yoh. “High quality Fe<sub>3- $\delta$</sub> O<sub>4</sub>/InAs hybrid structure for electrical spin injection”. *Appl. Phys. Lett.*, 90, 112501, 2007. doi:[10.1063/1.2713784](https://doi.org/10.1063/1.2713784).
- [89] S. A. Chambers. “Epitaxial growth and properties of thin film oxides”. *Surf. Sci. Rep.*, 39, 105, 2000. doi:[10.1016/S0167-5729\(00\)00005-4](https://doi.org/10.1016/S0167-5729(00)00005-4).
- [90] W. Weiss and W. Ranke. “Surface chemistry and catalysis on well-defined iron-oxide layers”. *Prog. Surf. Sci.*, 70, 1, 2002. doi:[10.1016/S0079-6816\(01\)00056-9](https://doi.org/10.1016/S0079-6816(01)00056-9).
- [91] F. Greullet, E. Snoeck, C. Tiusan, M. Hehn, D. Lacour, O. Lenoble, C. Magen and L. Calmels. “Large inverse magnetoresistance in fully epitaxial Fe/Fe<sub>3</sub>O<sub>4</sub>/MgO/Co magnetic tunnel junctions”. *Appl. Phys. Lett.*, 92, 053508, 2008. doi:[10.1063/1.2841812](https://doi.org/10.1063/1.2841812).
- [92] X. W. Li, A. Gupta, G. Xiao, W. Qian and V. P. Dravid. “Fabrication and properties of heteroepitaxial magnetite, (Fe<sub>3</sub>O<sub>4</sub>) tunnel junctions”. *Appl. Phys. Lett.*, 73, 22, 1998. doi:[10.1063/1.121710](https://doi.org/10.1063/1.121710).
- [93] F. Bertram, C. Deiter, O. Hoefert, M. Suendorf, T. Schemme, F. Timmer, B. Zimmermann and J. Wollschläger. “X-ray diffraction study on size effects in epitaxial magnetite thin films on MgO(001)”. *J. Phys. D: Appl. Phys.*, 2012.
- [94] C.-H. Lai, P.-H. Huang and Y.-J. Wang. “Room-temperature growth of Fe<sub>3</sub>O<sub>4</sub> films by ion beam deposition”. *J. Appl. Phys.*, 95, 7222, 2004. doi:[10.1063/1.1667420](https://doi.org/10.1063/1.1667420).
- [95] D. M. Lind, S. D. Berry, G. Chern, H. Mathias and L. R. Testardi. “Growth and structural characterization of Fe<sub>3</sub>O<sub>4</sub> and NiO thin films and superlattices grown by oxygen-plasma-assisted molecular-beam epitaxy”. *Phys. Rev. B*, 45, 1838, 1992. doi:[10.1103/PhysRevB.45.1838](https://doi.org/10.1103/PhysRevB.45.1838).
- [96] E. Lochner, K. Shaw, R. DiBari, W. Portwine, P. Stoyonov, S. Berry and D. Lind. “Studies of the stoichiometrical variation of epitaxial Fe<sub>3(1- $\delta$ )</sub>O<sub>4</sub> thin films”. *IEEE Trans. Magn.*, 30(6), 4912, 1994. doi:[10.1109/20.334263](https://doi.org/10.1109/20.334263).

- [97] S. A. Chambers, S. Thevuthasan and S. A. Joyce. "Surface structure of MBE-grown  $\text{Fe}_3\text{O}_4(001)$  by X-ray photoelectron diffraction and scanning tunneling microscopy". *Surf. Sci.*, 450, L273, 2000. doi:[10.1016/S0039-6028\(00\)00230-2](https://doi.org/10.1016/S0039-6028(00)00230-2).
- [98] F. Bertram, C. Deiter, T. Schemme, S. Jentsch and J. Wollschläger. "Disorder on tetrahedral sites of ultrathin magnetite films grown on  $\text{MgO}(001)$ ". *Phys. Rev. B*, submitted, 2012.
- [99] F. Bertram, C. Deiter, K. Pflaum, M. Suendorf, C. Otte and J. Wollschläger. "In-situ x-ray diffraction studies on post-deposition vacuum-annealing of ultra-thin iron oxide films". *J. Appl. Phys.*, 110, 102208, 2011. doi:[10.1063/1.3661655](https://doi.org/10.1063/1.3661655).
- [100] R. Harrison and A. Putnis. "Magnetic properties of the magnetite-spinel solid solution; Curie temperatures, magnetic susceptibilities, and cation ordering". *Am. Mineral.*, 81, 375, 1996.
- [101] Y. Gao, Y. J. Kim, S. Thevuthasan and S. A. Chambers. "Growth, structure, and magnetic properties of  $\gamma\text{-Fe}_2\text{O}_3$  epitaxial films on  $\text{MgO}$ ". *J. Appl. Phys.*, 81, 3253, 1997. doi:[10.1063/1.364355](https://doi.org/10.1063/1.364355).
- [102] F. C. Voogt, P. J. M. Smulders, G. H. Wijnja, L. Niesen, T. Fujii, M. A. James and T. Hibma. " $\text{NO}_2$ -assisted molecular-beam epitaxy of wustitelike and magnetitelike Fe oxynitride films on  $\text{MgO}(100)$ ". *Phys. Rev. B*, 63, 125409, 2001. doi:[10.1103/PhysRevB.63.125409](https://doi.org/10.1103/PhysRevB.63.125409).
- [103] J. Stremper, B. Bohnenbuck, I. Zegkinoglou, N. Aliouane, S. Landsgesell, M. v. Zimmermann and D. N. Argyriou. "Magnetic-field-induced transitions in multiferroic  $\text{TbMnO}_3$  probed by resonant and nonresonant x-ray diffraction". *Phys. Rev. B*, 78, 024429, 2008. doi:[10.1103/PhysRevB.78.024429](https://doi.org/10.1103/PhysRevB.78.024429).
- [104] J. C. Gielen, M. Wolffs, G. Portale, W. Bras, O. Henze, A. F. M. Kilbinger, W. J. Feast, J. C. Maan, A. P. H. J. Schenning and P. C. M. Christianen. "Molecular Organization of Cylindrical Sexithiophene Aggregates Measured by X-ray Scattering and Magnetic Alignment". *Langmuir*, 25(3), 1272, 2009. doi:[10.1021/la8039913](https://doi.org/10.1021/la8039913).
- [105] J. E. Daniels, W. Jo, J. Roedel, D. Rytz and W. Donner. "Structural origins of relaxor behavior in a  $0.96(\text{Bi}_{1/2}\text{Na}_{1/2})\text{TiO}_3\text{-}0.04\text{BaTiO}_3$  single crystal under electric field". *Appl. Phys. Lett.*, 98(25), 252904, 2011. doi:[10.1063/1.3602316](https://doi.org/10.1063/1.3602316).
- [106] P. Chen, R. J. Sichel-Tissot, J. Young Jo, R. T. Smith, S.-H. Baek, W. Saenrang, C.-B. Eom, O. Sakata, E. M. Dufresne and P. G. Evans. "Nonlinearity in the high-electric-field piezoelectricity of epitaxial  $\text{BiFeO}_3$  on  $\text{SrTiO}_3$ ". *Appl. Phys. Lett.*, 100(6), 062906, 2012. doi:[10.1063/1.3683533](https://doi.org/10.1063/1.3683533).
- [107] B. Bohnenbuck, I. Zegkinoglou, J. Stremper, C. S. Nelson, H.-H. Wu, C. Schüßler-Langeheine, M. Reehuis, E. Schierle, P. Leininger, T. Herrmannsdörfer, J. C. Lang, G. Srajer, C. T. Lin and B. Keimer. "Magnetic Structure of  $\text{RuSr}_2\text{GdCu}_2\text{O}_8$  Determined by Resonant X-Ray Diffraction". *Phys. Rev. Lett.*, 102, 037205, 2009. doi:[10.1103/PhysRevLett.102.037205](https://doi.org/10.1103/PhysRevLett.102.037205).
- [108] B. K. Gan, I. C. Madsen and J. G. Hockridge. "In situ X-ray diffraction of the transformation of gibbsite to alpha-alumina through calcination: effect of particle size and heating rate". *J. Appl. Cryst.*, 42, 697, 2009. doi:[10.1107/S0021889809021232](https://doi.org/10.1107/S0021889809021232).

- [109] P. Nolte, A. Stierle, N. Kasper, N. Y. Jin-Phillipp, N. Jeutter and H. Dosch. “Reversible Shape Changes of Pd Nanoparticles on MgO(100)”. *Nano Lett.*, 11(11), 4697, 2011. doi:[10.1021/nl2023564](https://doi.org/10.1021/nl2023564).
- [110] A. Hellman, A. Resta, N. M. Martin, J. Gustafson, A. Trincherro, P.-A. Carlsson, O. Balmes, R. Felici, R. van Rijn, J. W. M. Frenken, J. N. Andersen, E. Lundgren and H. Grönbeck. “The Active Phase of Palladium during Methane Oxidation”. *The Journal of Physical Chemistry Letters*, 3(6), 678, 2012. doi:[10.1021/jz300069s](https://doi.org/10.1021/jz300069s).
- [111] H. L. Meyerheim, D. Sander, R. Popescu, J. Kirschner, P. Steadman and S. Ferrer. “Surface structure and stress in Fe monolayers on W(110)”. *Phys. Rev. B*, 64, 045414, 2001. doi:[10.1103/PhysRevB.64.045414](https://doi.org/10.1103/PhysRevB.64.045414).
- [112] H. Bulou, F. Scheurer, P. Ohresser, A. Barbier, S. Stanescu and C. Quirós. “Structure of self-organized Fe clusters grown on Au(111) analyzed by grazing incidence x-ray diffraction”. *Phys. Rev. B*, 69, 155413, 2004. doi:[10.1103/PhysRevB.69.155413](https://doi.org/10.1103/PhysRevB.69.155413).
- [113] M. Takahashi, Y. Yoneda, H. Inoue, N. Yamamoto and J. Mizuki. “X-Ray Diffractometer for Studies on Molecular-Beam-Epitaxy Growth of III-V Semiconductors”. *Jpn. J. Appl. Phys.*, 41, 6247, 2002. doi:[10.1143/JJAP.41.6247](https://doi.org/10.1143/JJAP.41.6247).
- [114] S. Ferrer and F. Comin. “Surface diffraction beamline at ESRF”. *Rev. Sci. Inst.*, 66, 1674, 1995. doi:[10.1063/1.1145879](https://doi.org/10.1063/1.1145879).
- [115] J. Rubio-Zuazo and G. Castro. “Probing Buried Interfaces by Simultaneous Combination of X-ray Diffraction (SXRD) and Hard X-ray Photoelectron Spectroscopy (HAXPES, up to 15 KeV)”. *Rev. Adv. Mater. Sci.*, 15, 79, 2007.
- [116] D. Walko, O. Sakata, P. Lyman, T.-L. Lee, B. P. Tinkham, J. S. Okasinski, Z. Zhang and M. Bedzyk. “surface and interface studies at APS endstation 5ID-C”. *AIP Conf. Proc.*, 705, 1166, 2004. doi:[10.1063/1.1758007](https://doi.org/10.1063/1.1758007).
- [117] J. Bohr, R. Feidenhans'l, M. Nielsen, M. Toney, R. L. Johnson and I. K. Robinson. “Model-Independent Structure Determination of the InSb(111)2x2 Surface with Use of Synchrotron X-Ray Diffraction”. *Phys. Rev. Lett.*, 54, 1275, 1985. doi:[10.1103/PhysRevLett.54.1275](https://doi.org/10.1103/PhysRevLett.54.1275).
- [118] R. Feidenhans'l, F. Grey, R. L. Johnson, S. G. J. Mochrie, J. Bohr and M. Nielsen. “Oxygen chemisorption on Cu(110): A structural determination by x-ray diffraction”. *Phys. Rev. B*, 41, 5420, 1990. doi:[10.1103/PhysRevB.41.5420](https://doi.org/10.1103/PhysRevB.41.5420).
- [119] I. Joumard, X. Torrelles, T.-L. Lee, O. Bikondoa, J. Rius and J. Zegenhagen. “Nanostucture of a vicinal surface of SrTiO<sub>3</sub>: Order on two length scales”. *Phys. Rev. B*, 74, 205411, 2006. doi:[10.1103/PhysRevB.74.205411](https://doi.org/10.1103/PhysRevB.74.205411).
- [120] D. Martoccia, P. R. Willmott, T. Brugger, M. Björck, S. Günther, C. M. Schlepütz, A. Cervellino, S. A. Pauli, B. D. Patterson, S. Marchini, J. Winterlin, W. Moritz and T. Greber. “Graphene on Ru(0001): A 25 × 25 Supercell”. *Phys. Rev. Lett.*, 101, 126102, 2008. doi:[10.1103/PhysRevLett.101.126102](https://doi.org/10.1103/PhysRevLett.101.126102).
- [121] F. U. Renner, Y. Gründer and J. Zegenhagen. “Portable chamber for the study of UHV prepared electrochemical interfaces by hard x-ray diffraction”. *Rev. Sci. Inst.*, 78, 033903, 2007. doi:[10.1063/1.2714046](https://doi.org/10.1063/1.2714046).
- [122] M.-C. Saint-Lager, A. Bailly, P. Dolle, R. Baudoing-Savois, P. Taunier, S. Garaudee, S. Cuccaro, S. Douillet, O. Geaymond, G. Perroux, O. Tissot, J.-S. Micha, O. Ulrich

- and F. Rietord. “New reactor dedicated to in operando studies of model catalysts by means of surface x-ray diffraction and grazing incidence small angle x-ray scattering”. *Rev. Sci. Inst.*, 78, 083902, 2007. doi:[10.1063/1.2766821](https://doi.org/10.1063/1.2766821).
- [123] R. van Rijn, M. D. Ackermann, O. Balmes, T. Dufrane, A. Geluk, H. Gonzalez, H. Isern, E. de Kyper, L. Petit, V. Sole, D. Wermeille, R. Felici and J. W. M. Frenken. “Ultrahigh vacuum/high-pressure flow reactor for surface x-ray diffraction and grazing incidence small angle x-ray scattering studies close to conditions for industrial catalysis”. *Rev. Sci. Inst.*, 81, 014101, 2010. doi:[10.1063/1.3290420](https://doi.org/10.1063/1.3290420).
- [124] P. Bernard, K. Peters, J. Alvarez and S. Ferrer. “Ultrahigh vacuum/high pressure chamber for surface x-ray diffraction experiments”. *Rev. Sci. Inst.*, 70, 1478, 1999. doi:[10.1063/1.1149609](https://doi.org/10.1063/1.1149609).
- [125] L. Merrill and W. A. Bassett. “Miniature diamond anvil pressure cell for single crystal x-ray diffraction studies”. *Rev. Sci. Inst.*, 45, 290, 1974. doi:[10.1063/1.1686607](https://doi.org/10.1063/1.1686607).
- [126] R. Resel, E. Tamas, B. Sonderegger, P. Hofbauer and J. Keckes. “A heating stage up to 1173K for X-ray diffraction studies in the whole orientation space”. *J. Appl. Cryst.*, 36(1), 80, 2003. doi:[10.1107/S0021889802019568](https://doi.org/10.1107/S0021889802019568).
- [127] *Brush Wellman, Inc.*, <http://www.brushwellman.com>.



# List of Figures

1.1. Schematic drawing of a magnetic tunneling junction consisting of two ferromagnetic electrodes ( $F_1$ and $F_2$ ) separated by a thin insulator (I) and the respective density of states profile for magnetization in both electrodes aligned parallel (a) and antiparallel (b). . . . .	5
2.1. Sketch of a two dimensional crystal. The position of each atom within the crystal $\mathbf{r}_{atom}$ is given by the sum of the position vector of the unit cell $\mathbf{r}_n$ and the position vector of the atom within the unit cell $\mathbf{r}_j$ . . . . .	7
2.2. Schematic drawings of the different growth modes: a) layer-by-layer, b) island, and c) layer-plus-island growth. . . . .	8
2.3. Schematic drawings of the different relaxation processes: a) pseudomorphic growth, and b) misfit dislocations. . . . .	9
2.4. An incidence wave $\mathbf{k}_i$ is reflected at a crystal lattice plane (solid lines). The outgoing waves $\mathbf{k}_f$ have different phase due to the path difference $a$ . If $2a = n\lambda$ is fulfilled the outgoing waves interfere constructively and a Bragg peak can be observed. The scattering vector $\mathbf{q}$ resulting from $\mathbf{k}_i$ and $\mathbf{k}_f$ is oriented perpendicular to the lattice planes. . . . .	12
2.5. Schematic drawing showing the intensity distribution in reciprocal space. a) Three dimensional crystals produce diffraction spots in reciprocal space. The dashed lines are direction markers only. b) Two dimensional layers produce diffraction rods. c) Surfaces of crystals produce diffraction spots connected by modulated diffraction rods in vertical direction. d) Thin films produce diffraction spots and oscillations (fringes) in vertical direction. . . . .	16
2.6. Height profile of a semi-infinite crystal surface. The average step height is at the zero level, while the profile is defined by the function $N_c(n_a, n_b)$ . . . . .	17
2.7. Height profile of a thin film with an average thickness of $\overline{N_c}$ . The roughness of the film top is given by $N_c^+(n_a, n_b)$ , the roughness of the film bottom is given by $N_c^-(n_a, n_b)$ . . . . .	18
2.8. The N-slit function for $N = 6$ . Main maxima occur at multiples of $2\pi$ with $N-2$ smaller side maxima or fringes in between two main maxima. The spacing between two fringes is $\frac{2\pi}{N}$ . The FWHM of the main peaks is also given by $\frac{2\pi}{N}$ . . . . .	19
2.9. Schematical drawing of a layer system consisting of two films and a substrate. . . . .	19
2.10. Reflectivity of a thin film on a substrate. At each interface the incidence beam ( $\mathbf{k}_i$ ) is reflected and transmitted. Also, the reflection and transmission of the beam reflected at buried interfaces is contributing to the total reflected intensity. . . . .	21

---

2.11. Reflectivity curve for a magnetite layer on MgO. Up to the critical angle total external reflection is observed. After that the intensity is decreasing. The observed oscillations originate from an interference between the beams reflected at the film/vacuum and the substrate/film interface. . . . .	22
2.12. Ewald construction for a LEED setup using normal incidence. The Ewald sphere (dashed line) is defined by all possible positions for the wave vector of the diffracted beam. The rods (solid line) are the positions in reciprocal space where the 2D Laue conditions are fulfilled. At the interception points of the rods and Ewald sphere diffraction spots can be observed with LEED. . . . .	23
2.13. A three-grid LEED setup <sup>[31]</sup> with a filament emitting the electrons, Wehnelt cylinder (W), electrostatic lens (A, B, C, D), and the fluorescent screen with the three-grid system for background suppression and electron acceleration. . . . .	24
2.14. Schematical drawing of the photoemission excitation process. Electrons are excited by incoming photons with an energy $\hbar\omega$ and are emitted with a kinetic energy $E_{kin} = \hbar\omega - E_i - \phi$ . . . . .	25
2.15. Typical XPS setup consisting of an x-ray tube and a hemispherical analyzer. Due to the incoming x-ray beam the sample emits photoelectrons. By applying electric fields in the analyzer only electrons of a certain energy can pass the analyzer and can be detected at the detector. . . . .	26
3.1. Phase diagram as a function of temperature and oxygen partial pressure obtained by Kettler et al. from theoretical calculations <sup>[32]</sup> . . . . .	27
3.2. Sketch of the wüstite unit cell. . . . .	28
3.3. Sketch of the magnetite unit cell. . . . .	28
3.4. a) typical LEED image from a magnetite thin film showing the $(\sqrt{2} \times \sqrt{2})R45$ superstructure of the reconstructed surface. b) LEED image (taken from <sup>[36]</sup> ) of a magnetite film grown on MgO which was annealed at 600°C after deposition showing the typical $(3 \times 1)$ superstructure for magnetite films contaminated by magnesium segregation. . . . .	29
3.5. XPS spectra for different iron oxide phases as determined by Yamashita et al. <sup>[41]</sup> . . . . .	30
3.6. Phase diagram for the deposition of iron oxide thin films using plasma assisted MBE obtained from Gao et al. <sup>[46]</sup> . The border between the different phases is indicated by solid lines while the boxes mark the optimal deposition conditions for each phase. The $\text{Fe}_2\text{O}_3$ data includes both $\alpha\text{-Fe}_2\text{O}_3$ as well as $\gamma\text{-Fe}_2\text{O}_3$ depending on the used substrate. . . . .	31
3.7. Illustration of a thin film grown on a substrate showing antiphase boundaries in a) side view and b) top view. . . . .	33
3.8. Sketch of the MgO unit cell with the surface coordinate system used for indexing the reciprocal space in this work. . . . .	33
3.9. Sketch of the MgO surface unit cell. . . . .	34

3.10. Sketch of the $H = 0$ plane of the reciprocal space for the MgO(001)/iron oxide system assuming the bulk lattice parameters. Open symbols indicate Bragg peaks originating exclusively from tetrahedral sites. . . . .	35
3.11. a), d) contribution of the different magnetite sites to the structure factor. The solid line shows the contribution from iron ions at the tetrahedral sites, the dashed line iron ions at the contribution from the octahedral sites and the dash-dotted line the contribution from oxygen ions. b), e) The total structure factor of magnetite. c), f) the diffracted intensity from a magnetite film. The top row shows calculations for the $(00L)$ direction, the bottom row for the $(01L)$ direction. . . . .	36
4.1. Radiation pattern of an electron traveling along a circular path a) with non-relativistic velocity and b) with a velocity close to the speed of light. Taken from <sup>[57]</sup> and revised. . . . .	38
4.2. Schematical drawing of a wiggler/undulator. The wiggler/undulator consists of an alternating magnet structure which forces the electron beam on an oscillating path while traveling through the wiggler. This causes the emission of synchrotron radiation. . . . .	39
4.3. Schematical drawing of a typical double-crystal monochromator. The white beam from the x-ray source is hitting the first DCM crystal. Here, the beam is diffracted at both the first and the second DCM crystal. To achieve a fixed vertical offset the second crystal can typically be shifted perpendicular and parallel to the first crystal. To compensate for small misalignments of both DCM crystals the second crystal typically has two additional rotations. One rotation in the same plane as the main axis ( <i>pitch</i> ) and the other one perpendicular to it ( <i>roll</i> ). . . . .	40
4.4. Calculated reflectivity of a x-ray mirror coated with 100 nm gold for 10 and 30 keV. The critical angles for total reflection are indicated by dashed lines. . . . .	42
4.5. Sketch of the z-axis diffractometer at W1. The rotation $\alpha$ is rotating the whole diffractometer with respect to the incoming beam. The rotations $\delta$ and $\gamma$ are used for the positioning of the detector, while $\omega$ is used for sample positioning. Using the z-axis mode, where the sample is vertically mounted, $\alpha$ is the fixed angle of incidence, $\omega$ the sample azimuth, $\delta$ the inplane detector angle and $\gamma$ the out of plane detector angle. In the four-circle mode, where the sample is horizontally mounted, $\alpha$ and $\gamma$ are fixed to zero, $\omega$ is the variable angle of incidence and $\delta$ the out of plane detector angle. . . . .	43
4.6. Sketch illustrating the four degrees of freedom for the position of the incidence angle and the exiting angle. . . . .	46
4.7. Penetration depth of an x-ray beam of 10.5 keV upon a magnetite surface as a function of the angle of incidence $\alpha_i$ . . . . .	47
4.8. Sketch illustrating the active sample area for the grazing incidence geometry. The active area is defined by the entrance slit size, i.e. the primary beam size, the detector slit size and the angle between sample and detector. . . . .	49

4.9. a) The intensity of an N-Slit function for different $N$ ranging from 6 to 7. For non-integer $N$ the intensity becomes infinity at $L = 1$ . b) The intensity of a stack of two films. The lower layer consists of 6 atomic layers with $\Theta = 1$ while the top layer consists of a single atomic layer with $\Theta$ ranging from 0 to 1. . . . .	54
4.10. Calculated intensity using different roughness values. For reasons of simplicity the calculation is done for a $\text{Fe}_3\text{O}_4$ substrate but the same behavior occurs for thin films. With increasing roughness the intensity between the Bragg peaks is dampened. However, the intensity at the Bragg peaks forbidden by the structure factor (half order positions) remains constant independent of the roughness. . . . .	55
8.1. XPS measurements of the Fe2p (a) and the Fe3p (b) peak regions for the as-deposited sample and the PDA samples. . . . .	64
8.2. Relative iron and magnesium content obtained by peak fitting of the Fe3p peak region. . . . .	65
8.3. XRD in specular geometry for the as-deposited film as well as the PDA samples. . . . .	66
8.4. CTR scans of the $(01L)$ rod for the as-deposited sample and the PDA samples. . . . .	66
8.5. Integrated intensity (a) and FWHM (b) of the $(011)$ peak obtained by fitting a Gaussian function. . . . .	67
A.1. Gaussian peak shape, periodically iterated delta peaks, their convolution, and its approximation using a cos function for $\sigma = 1.5$ . . . . .	76

## List of Tables



# Acknowledgments

Finally, I would like to acknowledge several people who supported me during my time as a PhD student.

First, I would like to thank my supervisor Prof. Wollschläger for his support, fruitful discussions, and meaningful input during all the time. I would also like to thank Prof. Falta for filling the role of the secondary reviewer.

In addition I would like to thank my colleagues at DESY. Especially, I would like to thank Carsten Deiter for fruitful discussions and his help during numerous beamtimes, Oliver Seeck who could always provide very helpful advises, Wolfgang Caliebe for providing many beamtimes (in some cases also off schedule) at his beamline, and Kathrin Pflaum for her technical support.

Furthermore, I would like to thank the current and former members of Prof. Wollschlägers workgroup for the great working atmosphere there, their support during sample preparation, fruitful discussions, and last but not least after work activities. Especially, Daniel Bruns, Sebastian Gevers, Steffen Jentsch, Timo Kuschel, Christian Otte, Tobias Schemme, Martin Suendorf, Frederic Timmer, Henrik Wilkens should be mentioned here.

Finally, I would like to thank my family and friends for their support during the time of my thesis.



# Erklärung

Hiermit erkläre ich an Eides Statt, die vorliegende Abhandlung selbstständig und ohne unerlaubte Hilfe verfasst, die benutzen Hilfsmittel vollständig angegeben und noch keinen Promotionsversuch unternommen zu haben.

Osnabrück, 10.09.2012  
Florian Bertram





